Molecular mechanism of action of tyrocidine antimicrobial peptides using NMR spectroscopy and computational techniques

by

Gadzikano Munyuki

BSc (Hon) Applied Chemistry

Thesis Presented for the Degree of

DOCTOR OF PHILOSOPHY

in the Department of Chemistry

UNIVERSITY OF CAPE TOWN

December 2012

Supervisor: **Prof Graham E Jackson**

Co-Supervisor: **Dr Gerhard Venter**

Abstract

The need to come up with new and novel antibiotics that utilize unique mechanisms, to which bacteria cannot generate resistance, was the main motivation of this study. Tyrocidine peptides are non-selective antibiotics that have such properties. However, very limited information is available about their mechanism of action. The aim of this study was to determine the mechanism of action of tyrocidine peptides, tyrocidine A, tyrocidine B and tyrocidine C.

Chapter 3 explored the structure of tyrocidine peptides using molecular dynamics and NMR spectroscopy. All tyrocidine peptides formed β -structures in membrane mimetic environments. Tyrocidine A and tyrocidine C formed β-structures in water, and tyrocidine B was unstructured.

The results of the study of self-aggregation of tyrocidine C in water are shown in Chapter 4. Tyrocidine C monomers form dimers by coming together in sideways orientation. They could form higher ordered structures through the addition of monomers on either side of the dimer. At high concentrations, the peptide forms small aggregates, which eventually come together to form one large unstructured aggregate. The formation of higher ordered structures in water is expected to take much longer than the time simulated.

There was very little disruption of both mammalian and bacterial membrane structures within the simulated timescales as shown in Chapter 5. However it was noted that tyrocidine peptides could permeate the membrane and possibly form aggregates that can disrupt the membrane structure. Aggregation of the peptides in the water section of the membrane reduced the interactions between the peptides and the membrane, thereby increasing the amount of time needed for the peptides to disrupt the membrane.

Homology modeling based channels of tyrocidine peptides were very similar to that of gramicidin S (Chapter 6). The study of the channels in membrane indicated that they are relatively stable in the hydrophobic region of the membrane and unstable in the water phase of the membrane. These results suggested that tyrocidines could destroy bacterial cell structure through channel formation.

The investigation of tyrocidine C and Ca^{2+} binding expected to avail an alternative non-lysis mechanism of action was difficult to ascertain. Experimental results showed that Ca^{2+} weakly binds tyrocidine C. This was contrary to quantum mechanical calculations, which gave plausible tyrocidine-Ca^{2+} complexes.

The overall conclusion of this study is that, there could be several ways through which tyrocidines destroy the membrane. Events such as self-assembly, membrane binding and channel formation may all play major roles in the mechanism of action of tyrocidines.

Acknowledgements

I would not have made it this far had it not been for the grace of God that He showers over me each and every day. I will continue to love and serve him all the days of my life.

Leverhulm Trust paid for my studies through the UCT chemistry department equity development program scholarship for the past four and half years. They believed in me, and saw it fit to help me pursue my dreams. I will forever be indebted to them.

I thank God for giving me a very supportive family and friends. This journey would have been very difficult without their unconditional love and support. I love them with all my heart. A special thank you goes to my wife and my mother; they are the most supportive ladies I have ever seen.

The University of Cape Town chemistry department has been very supportive to me and I am very thankful to everyone. Gerald Heselink helped me a lot with computer stuff. I really appreciate all the help he offered. Prof Jackson's research group, past and present members have been a very tremendous lot. A special mention goes to Dr Grace Mugumbate who helped me with GROMACS and with whom I had countless discussions during the course of this study. May God reward her immensely.

Professor David van der Spoel and his research group offered tremendous help through very fruitful discussions during the course of this study. He also helped me with a lot of computer time. I really appreciate all the help he extended to me.

My supervisors, Prof Graham Jackson and Dr Gerhard Venter have been very tremendous. I really appreciate their patience. I know there were times when I would ask very "stupid" questions but they were always patient and very willing to help.

Table of Contents

Chapter 1

Literature Review

1.1 Introduction

Antibiotic resistance is one of the biggest problems being experienced in human health and is particularly pressing in developing world.[1] The European Union (EU) suffers around 25 000 deaths from antibiotic resistant bacteria related aliments every year. This costs about €1· 5 billion in health care and lost productivity. In the US, antibiotic resistant bacteria have been shown to cause more deaths than HIV/AIDS, Parkinson's disease emphysema, and homicide combined.[2] Around 94 000 cases of Meticillin resistant *Staphylococcus aureus* (MRSA) infections and close to 18 000 deaths are reported in the US alone every year.[3]

Antibiotic development dates back to the early 1930s with the discovery of penicillin. Tyrocidines, the antibiotics of interest in this study, were discovered in the late 1940s and their use was stopped after they were discovered to be hemolytic. Their use is now limited to topical application.[4, 5] Antibiotic resistance was first discovered in the 1940s but new antibiotic were developed from the ones already in use. By the 1970s, the human life expectancy had increased by 8 years and this was attributed to the discovery of antibiotics. In the late 1990s certain strains of bacteria were becoming resistant to almost all known antibiotics of the time.

The development of new antibiotics has been very slow. Pharmaceutical companies have been very reluctant to work in this field due to the very short useful lifetimes of antibiotics before bacteria can develop resistance.[2, 6] In recent years new antibiotic drugs such as linezolid, daptomycin, tigecycline,[7] telavacin and ceftaroline have been developed. Resistance to these new antibiotics has already been recorded.[8, 9]

1.2 Cyclic antibiotics peptides

Several antimicrobial peptides have been discovered from natural sources as well as by synthetic methods.[10] Antimicrobial peptides are generally classified according to their secondary structure and there are four predominant classes that include β-sheet, α-helical, loop and extended peptides.[11-13] Cyclic peptides are mostly made up of β-sheet secondary structure. There are different ways through which the conformations of cyclic peptides are constrained, and these include disulfide cross-links and backbone cyclization by amide bonds.[14] Cyclization constrains the conformation of the peptides making it easy for them to penetrate membrane cell walls. Their rigid conformation is one of the reasons why cyclic peptides have gained attention as bioactive agents.

1.2.1 Disulphide-constrained cyclic peptides

Disulphide constrained cyclic antimicrobial peptides have at least one disulphide bond between cysteine side chains. This class of peptides includes bectenicins,[15, 16] tachyplesins,[17, 18] polyphemusins,[18] protegrins,[19-21] defensins,[22] and drosomycin.[23] Bactenicin is made up of 12 amino acids and is constrained by one disulphide bridge between two cysteine side chains. The primary sequence of bactenicin is RLCRIVVIRVCR. It is characterized by a type I β-turn secondary structure and has

been found to be active against gram-positive bacteria. Tachyplesin I is a cationic cyclic peptide that is made up of 17 amino acids. Two disulphide bridges constrain the conformation of tachyplesin I. It adopts a type II β-turn in both aqueous solution and membrane environments. Tachyplesin I is partially amphipathic because a polar arginine residue is found on both sides of the chain. The amphipathicity of tachyplesin I has been associated with its antimicrobial activity.[24] Protegrin I consist of 18 amino acids and has the following primary sequence RGGRLCYCRRRFCVCVGRa. Drosomycin is isolated from the haemolymph of drosophila. It is made up of 43 amino acids and is constrained by four disulphide bridges.

1.2.2 Novel D/L cyclic peptides

Cyclic peptides with alternating D and L-α amino acids are synthetically produced. They contain an even number of alternating D and L-α amino acids. These peptides form ring shaped conformations that are flat. Their side chains are always outside the ring and in the same plane with the ring structure. The peptides can aggregate in lipid membrane environments to form hollow, β-sheet like tubular structures with amino acid side chains outside the nanotube (Figure 1.1). The resultant peptide aggregates are known to have antimicrobial activity and they specifically permeabilize bacterial membranes.[25-28]

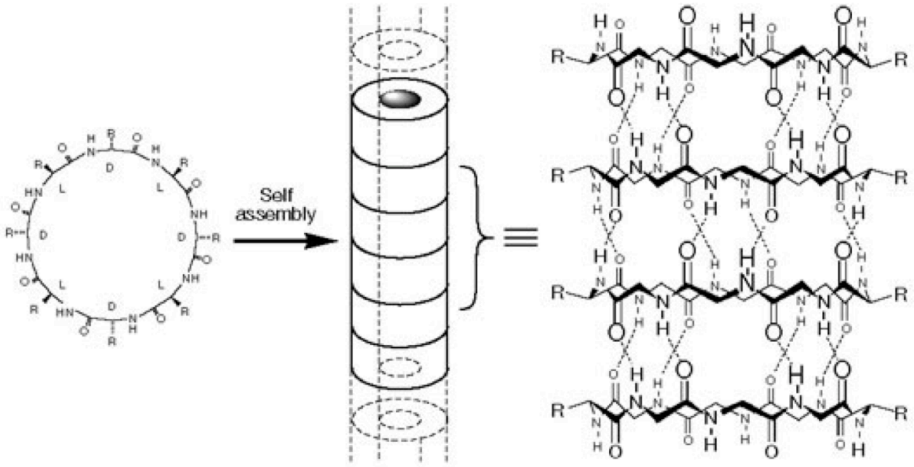

Figure 1.1: Schematic representation of nanotube assembly from cyclic D/L-peptides. For clarity, most of the peptide side-chains have been omitted. The illustration was taken from [29]

1.2.3 Cyclic Lipopeptides

Cyclic lipopeptides (CLPs) are produced by various bacterial species. They are characterized by a lipid tail linked to a short oligopeptide, which is cyclized to form a lactone ring between two amino acids in the peptide chain.[30] CLPs differ in terms of both structure and activity. The variation in the length and composition of the lipid tails and differences in the number, types and configurations of the amino acid moiety results in the structural diversity of CLPs. They have received considerable attention for their antimicrobial, cytotoxic, and surfactant properties.[30]

1.2.4 Tyrothricin based cyclic peptides (gramicidin and tyrocidines)

The discovery of tyrothricin,[31] a mixture of linear and cyclic gramicidins and tyrocidine antimicrobial peptides was credited to Rene Dubos in the late 1930s.[32-34] Tyrothricin was found to be toxic to red blood cells and this was mainly attributed to tyrocidine. Gramicidin was also found to be hemolytic however the toxicity was not as subtle as that

of tyrocidine. The use of these antibiotics is currently limited to topical application only.[4, 5]

1.2.4.1 Gramicidin S

Gramicidin S is one of the cyclic peptides that has been extensively studied.[35-37] It is comprised of the following amino acid sequence (*cyclo*[L-Val-L-Orn-L-Leu-D-Phe-L-Pro]$_2$). Gramicidin S is known to adopt antiparallel β-sheets with two type II β-turns in both aqueous solution and membrane environments. It is stabilized by four intramolecular hydrogen bonds.[38] The structure of gramicidin S is amphipathic with a distinct separation of hydrophilic and hydrophobic amino acids as well as charge, which gives it a polar and non-polar face.[39] It has a total charge of +2 that is attributed to basic ornithine residues. Figure 1.2 shows a molecular model of gramicidin S.

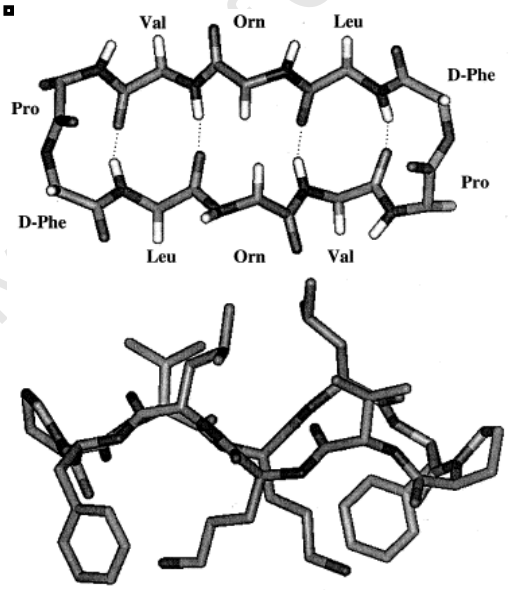

Figure 1.2: Molecular model of gramicidin S. The upper panel shows a top view of the backbone of Gramicidine S indicating the positions of potential interstrand hydrogen bonds. The lower panel shows a side view of Gramicidin S indicating the relative positioning of hydrophobic and basic residues. The illustration was taken from.[39]

1.2.4.2 Tyrocidine

A wide variety of tyrocidines have been isolated from tyrothricin.[31, 40] Tyrocidine A (TyrA), tyrocidine B (TyrB) and tyrocidine C (TyrC) are the most abundant making up to 60 % of tyrothricin. They have the following highly conserved sequence [*cyclo*D-Phe^1-L-Pro^2-L-X^3-D-X^4-L-Asn^5-LGln^6-L-Tyr^7-D-Val^8-L-Orn^9-L-Leu^{10}].[41] The sequences differ at residue positions L-X^3-D-X^4 that are occupied by L-Phe^3-D-Phe^4, L-Trp^3-D-Phe^4, and D-Trp^3-L-Trp^4 in TyrA, TyrB and TyrC respectively. There is also another class of tyrocidines that differs from the previous ones at position 9. Instead of ornithine, lysine occupies this position in this class. The differences on residue 9 can be used to subdivide tyrocidines into TyrA/TyrA1, TyrB/TyrB1 and TyrC/TyrC1 where TyrA, TyrB and TyrC have residue Orn on position 9 and TyrA1, TyrB1 and TyrC1 have residue Lys on the same position. The tyrocidines that contain Lys are the next most abundant after the ones that contain Orn. The rest of the tyrocidines that are found in tyrothricin are far less abundant. Of the most abundant tyrocidines the structure of TyrA, has been studied more than the others in recent years. TyrA is known to be amphipathic containing well separated hydrophilic and hydrophobic faces.[42]

Lately bacteria are becoming more and more resistant even to the last option antibiotics. This has resulted in renewed interest in the tyrocidine antimicrobial peptides and related compounds, as they are believed to utilize mechanisms that cannot be resisted by bacteria.

1.3 Secondary structure elements of peptides

Secondary structure elements can be classified as repeating structural elements or non-repeating structural elements.

1.3.1 Repeating structural elements

Repeating structural elements are characterized by a sequence of residues that contain a repeating pattern of ϕ, ψ dihedral angles and intramolecular hydrogen bonds. These regular structural elements can be divided into helices and β-sheets.

1.3.1.1 Helices

Helices are the most observed secondary structure elements in proteins and peptides. There are three different types of helices namely α-helix, 3_{10}-helix and pi-helix with the α-helix being the most observed among them. The helices are characterized by repeating ϕ, ψ dihedral angles and distinctive intramolecular hydrogen bonds. The hydrogen bonds are characterized by the bond between a C=O on residue i to a hydrogen HN on i+n residues away, forming a repeating pattern O_i-$HN_{i+n.}$ The ideal dihedral angles and the illustrations of helices are shown in Table 1.1 and Figure 1.4 respectively.

Table 1.1: Ideal dihedral angles for α, 3_{10} and pi helices

Type	Phi	Psi	H-bond pattern
α-helix	-58^0	-47^0	O_i-HN_{i+4}
3_{10}-helix	-74^0	-4^0	O_i-HN_{i+3}
pi-helix	-57^0	-70^0	O_i-HN_{i+5}

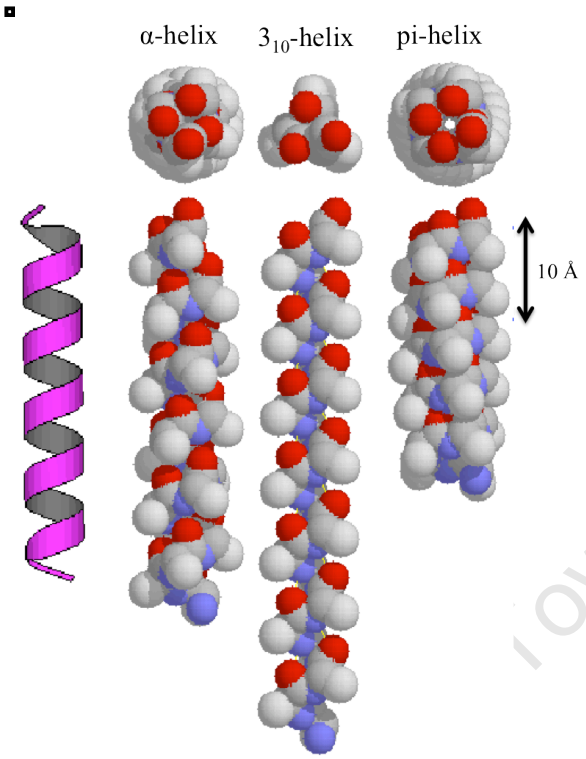

Figure 1.3: A cartoon representing different types of helical structures. *Views are perpendicular to the helical axis with the N-terminal at the bottom (lower) and following a 90 rotation (top). The illustration was adopted from* [43]

1.3.1.2 Sheets

β-sheets are made up of individual β-strands that are connected by inter-chain hydrogen bonds. They can be classified as antiparallel and parallel depending on the direction of interacting β-strands. The backbone dihedral angles ϕ and ψ on individual β-strands in β-sheets are approximately -120^0 and $+120^0$ respectively. The dihedral angles can also be used to differentiate between antiparallel and parallel β-sheets as they exhibit slightly different values. Table 1.2 and Figure 1.5 show the ideal dihedral angle values and the illustrations of parallel and antiparallel β-sheets respectively.

Table 1.2: Ideal dihedral angle values for parallel and antiparallel beta sheets

Type	Phi	Psi
Antiparallel	-139^0	135^0
Parallel	-119^0	113^0

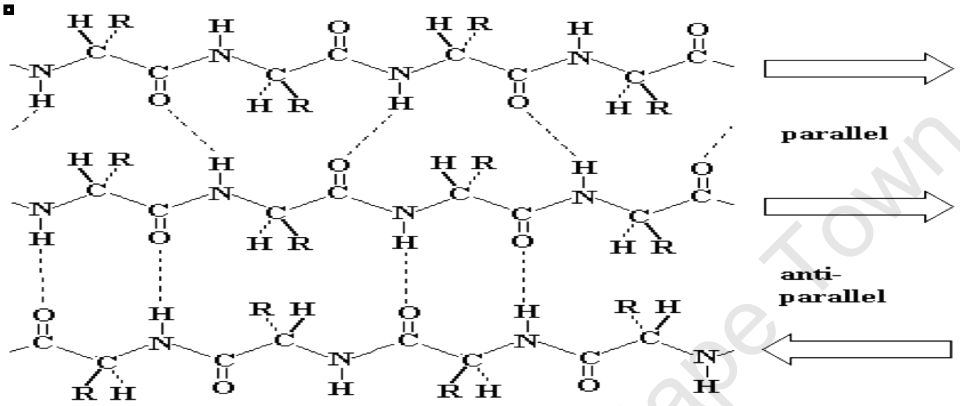

Figure 1.4: Parallel and antiparallel beta sheets. The hydrogen bonds are represented by dotted lines. The illustration was taken from[44]

1.3.2 Non-Repeating structural elements

1.3.2.1 Turns

There are two different types of turns that are exhibited by peptides and proteins secondary structures, called the β- and γ-turns. They are classified as non-repeating secondary structure elements. They are also known as reverse turns since they are involved in the chain reversal phenomena.

A β-turn is characterized by four consecutive residues and is mostly stabilized by a hydrogen bond between the carbonyl oxygen (C=O) of residue i and the amide HN of residue i + 3 (O_i-HN_{i+3}). Also, the distance between the α-carbons of residues i and i +3 is less than or equal to 7 Å in all β-turns. β-turns are also characterized by dihedral angles between residues i + 1 and i + 2, which are very important for parallel and antiparallel β-sheets respectively. Figure 1.6 shows the structures of different types of turns. In contrast to β-turns, γ-turns are made up of three subsequent residues and a hydrogen bond between the carbonyl oxygen (C=O) of residue i and the amide HN of residue i + 2 (O_i-HN_{i+2}). Table 1.3 below shows the characteristic dihedral angles of β-turns

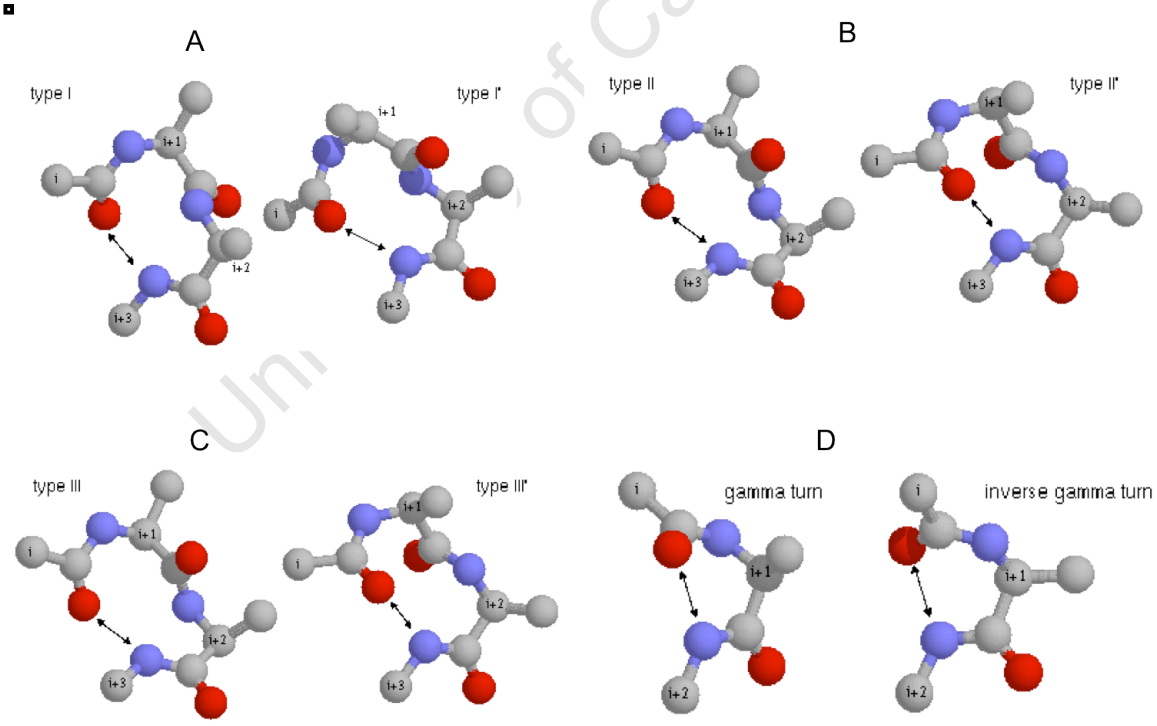

Figure 1.5: Types of turns found in peptides. Illustrations taken from[43]

Table 1.3: Dihedral angle values for different types of turns adapted from[45]

β-turn Type	Φ_{i+1}	Ψ_{i+1}	Φ_{i+2}	Ψ_{i+2}
I	-60^0	-30^0	-90^0	0^0
II	-60^0	120^0	80^0	0^0
III	-60^0	-30^0	-60^0	-30^0
I'	60^0	30^0	90^0	0^0
II'	60^0	-120^0	-80^0	0^0
III'	60^0	30^0	60^0	30^0
Γ	75^0	-64^0	-	-
γ'	-79^0	69^0	-	-

1.4 Specificity of antimicrobial peptides

Most antimicrobial peptides are known to specifically target microbial cell membranes and not mammalian cells. This is attributed to the differences in the lipid composition between the microbial cells and mammalian cells. Mammalian cells have neutral surfaces that are made up of zwitterionic lipids such as phosphatidylcholine (POPC), phosphatidylethanolamine (POPE) and sphingomyelin (SM). Microbial membranes are made up of negatively charged lipids such as phosphatidylglycerol (POPG), cardiolipin (CL) and phosphatidylserine (POPS) giving them a negatively charged surface. Since antimicrobial peptides are mostly positively charged they preferentially bind to the microbial membranes through electrostatic interactions.

The other difference between microbial cells and mammalian cells is the absence of cholesterol in in the membranes of microbial cells, which makes them more easily permeabilized by antimicrobial peptides. Cholesterol is believed to increase the rigidity of the mammalian membrane structure.

1.5 Factors that affect antimicrobial peptide activity

1.5.1 Physico-chemical properties

1.5.1.1 Secondary structure

The secondary structure that antimicrobial peptides adopt on the water-lipid interface has been shown to influence the activity of most peptides. There are four different classes of peptides that have been discovered based on structure namely, β-sheet, α-helical, loop and extended peptides (Figure 1.7).

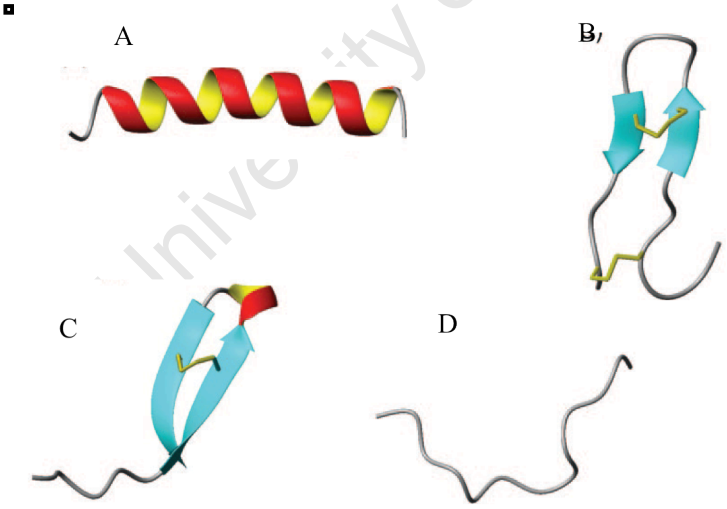

Figure 1.6: Structural classes of antimicrobial peptides. (A) Shows the structure of α-helical magainin-2, (B) Shows the structure of β-sheeted polyphemusin, (C) Shows the structure of looped thanatin and (D) Shows the structure of extended indolicidin. The illustrations were adopted from [47]

α-helical antibiotic peptides

α-helical antibiotic peptides exist mainly as extended peptides or unstructured conformers in solution.[46] The α-helical conformation, which characterizes them, forms upon interaction with the lipid membranes. Most α-helical antibiotic peptides are isolated from the extracellular fluids of insects and frogs.[46]

β -sheet peptides

The β -sheet peptides are made up of very different amino acid sequences, however they are genenerally known to be amphipathic, that is, they have hyrophilic and hydrophobic areas that are well separated.[46] Most β -sheet peptides are cyclic and posses antiparallel β -sheets. Tachyplesins, polyphemusins, bactenecins, protegrins, gramicidin S, polymixyn B and the tyrocidines are examples of cylic peptides that contain β -sheets.[11] A number of β -sheet peptides have been shown to exist as dimers in aqueous solution, one example is human defensin HNP-3.[46]

Loop antibiotic peptides

This class of pepides is characterized by their loop structure imparted by the presence of a single bond (either disulfide, amide or isopeptide).[48] The exact mechanism of action of loop antibiotic peptides is currently unknown. Experiments where membranes were treated with loop peptides did not have any effect on the membrane permeabilities hence their mechanism of action is believed not to involve membranes but other targets.[48]

Extended peptides

This class has some peptides with an unusual amino acid composition, having a sequence, which is rich in one or more specific residues. They lack classical secondary structures, generally due to their high proline/or glycine contents.[48] Tritrpticin and indolicidin are typical examples of extended peptides and are very rich in tryptophan. This amino acid enhances the partionining of peptides into membranes because of its ability to position itself near the membrane/water interface.[11]

1.5.1.2 Charge

The cationic charge of antimicrobial peptides is crucial for electostatic interaction with the negatively charged lipid membranes of bacteria. Antimicrobial peptides carry positive charges that vary from +2 to +9.[46] Studies of cerropins and magainin analogues showed that the activities of these peptides increases with an increase in cationic charge.[49-52] It has also been shown from studies of magainin that increase in the positive charge does not only increase the activity of some antimicrobial peptides but it also causes them to be unspecific. Very high charges in maginin have been shown to cause the peptide to lose specificity making them hemolytic. Large charges also result in unstable channels.[53] Charge can also be used to distinguish between the mechanisms of action that antimicrobial peptides utilise. Anionic antimicrobial peptides require minimum inhibitory concentrations that are much higher than those of cationic antimicrobial peptides indicating that they may utilise another mechanism of action.[54]

1.5.1.3 Amphipathicity

Amphipathicity of a peptide shows the separation in space of the polar and non-polar domains of a peptide. In some instances amphipathicity is portrayed by β-strands arranged in an antiparallel fashion. These β-sheets are common in cyclic peptides that are cyclised either by disulphide bonds or backbone cylization.

It can be measured by calculating the hydrophobic moment, which is the vector sum of hydrophobicities of each amino acid normalised to the helix axis. The mean hydrophobic moment of each residue can also be used to compare the amphipathicity of peptides that differ in lengths.[55] However this method is not very accurate hence another method, hydrophobic potential is more popular. This method considers the charge distribution along the axis of the helix and it also includes gaps between secluded amphipathic stretches. High values of the hydrophobic moments have been observed to make the peptide more cytotoxic by increasing membrane permeabilisation and hemolytic activities.[56, 57] Pathak *et al*[57] believed that amphipathicity could be the predominant property that determines the antibiotic property of a peptide.[56, 57] This led to the design of peptides that had interchanging hydrophobic and hydrophilic domains.[58] Similar studies by Wieprecht *et al* [59] revealed that increasing the hydrophobic moment hiked the activity of antimicrobial peptides on neutral membranes and showed only modest activity on negatively charged membranes. An increase in this parameter in magainin 2 analogues causes an enhanced permeabilizing efficiency on phosphatidycholine–rich bilayers, whereas the negatively charged model membranes are less affected. It suggests that hydrophilic interactions with acyl chains of lipids dominate

the activity on neutral membranes and this parameter influences the antimicrobial specificity in a negative manner.[59] However this understanding was challenged by results obtained from studies of the C-terminal fragment of melittins.[60] The size of the hydrophobic stretch influences the antibacterial activity more than the hemolytic activity.

1.5.1.4 Hydrophobicity

Hydrophobicity is defined as the proportion of hydrophobic residues in a peptide and it determines the environment that the peptide prefers between the aqueous phase and the hydrophobic phase. A more hydrophobic peptide would prefer a hydrophobic phase and the opposite is true for a peptide with low hydrophobicity. Most antimicrobial peptides prefer the hydrophobic lipid environment as they contain more hydrophobic residues than hydrophilic ones. It has also been shown that when hydrophobicity is too high antimicrobial peptides become haemolytic.[56, 61] Using Eisenberg's scale of hydrophobicity,[55] Wieprecht *et al*. studied the relationship between peptide hydrophobicity and membrane permeabilization. They managed to show that hydrophobicity of antimicrobial peptides has no effect on lipid membranes made up of phosphatidylglycerol (PG) only. However a 60 percent increase in the permeabilization effect was recorded for membranes that were made up of phosphatidylcholine (PC) and PG at a ratio of 3:1. Membrane models made up of PC only were affected much more than the other models, and they recorded a 300 percent increase in permeabilization. Studies on histatin and magainin have shown that the effect of antimicrobial peptides on mammalian cells is related to hydrophobicity and not to amphipathicity and charge. This therefore suggests that hydrophobicity plays a secondary role in the interaction between peptides and negatively charged bilayers.[62] It could then be concluded that the activity of

antimicrobial peptides is weakly associated with hydrophobicity. However an increase in this parameter reduces antimicrobial specificity. Hence hydrophobicity affects specificity and not activity.

1.6 Molecular mechanism of antimicrobial peptides

Antimicrobial peptides are known to deform membrane bilayers through various ways such as membrane thinning, pore formation and bilayer disruption, depending on the molecular properties of both the peptide and lipid. Antimicrobial peptides are known to kill bacteria through various mechanisms such as barrel stave, toroidal pore, carpet mechanism and channel aggregates.

In most of the known mechanisms there are common fundamental steps that are involved. Each mechanism is believed to initially involve the electrostatic interaction between antimicrobial peptides and the membrane, where the negatively charged lipo-polysaccharide (LPS) interacts with the positively charged antimicrobial peptides. Upon binding to the surface of the membrane, the peptides fold and are oriented parallel to the surface of the membrane. During the folding process, the hydrophobic residues of the peptides interact with the hydrophobic lipid acyl chains and the hydrophilic residues interact with the lipid headgroups. As more peptides bind to the surface of the membrane, they reach a threshold concentration.[63] At the threshold concentration the peptides reorient inserting themselves into the bilipid layer.[46] Several theories have been suggested as to what causes cell death once the peptides are inserted into the lipid bilayers. These include disruption of the membrane integrity, peptide translocation into the cell, leakage of cell contents and membrane depolarization.

1.6.1 Barrel stave/wormhole mechanism

In the barrel stave mechanism, individual peptides are arranged vertically in the membrane forming "staves" such that the hydrophobic residues are oriented towards the lipid tails and the hydrophilic residues make up the inside part of the channel. The pore is made up of peptides with distinct structure such as β-sheets or α-helices that are long enough to traverse the membrane. This mechanism of action has been proposed for alemethicin,[64-66] pardixin [67] and ceratotoxin.[68]

1.6.2 Toroidal pore mechanism

In the torroidal pore mechanism, the antimicrobial peptides insert into the membrane causing lipid leaflets to curve continuously through the pore so that both the inserted peptides and the lipid head groups line the water core. Among the peptides that utilize this mechanism are magainins,[69] protegrins[70] and melittins.[66]

1.6.3 Carpet mechanism

In the carpet mechanism, antimicrobial peptides orient themselves parallel to the surface of the membrane and accumulate on the membrane surface in a carpet like manner. At the threshold concentrations, the peptides disrupt the membrane integrity in a detergent like manner forming micelles. In a carpet mechanism peptides do not necessarily insert into the hydrophobic core. Cecropins,[71] and dermasptins[72] have been suggested to follow this mechanism.

1.6.4 Self-Assembly/Aggegate mechanism

In this mechanism, peptides insert themselves into the membrane forming unstructured aggregates composed of a mixture of peptides and lipids.[73] The aggregates result in the formation of pores of various sizes and lifetimes. The peptides eventually get into the cell where they attack specific intracellular targets resulting in cell death. It was suggested that indolicidin destroys the membrane structure by forming channel aggregates in the hydrophobic section of the membrane.[74]

1.6.5 Other alternative mechanisms

Alternative mechanisms of action have been reported for antimicrobial peptides. These include receptor-mediated and other mechanisms that target intracellular molecules. In receptor-mediated mechanisms, peptides bind to the receptor causing the formation of pores that result in membrane permeabilization. A typical example of a peptide that utilizes this mechanism is nisin. Intracellular molecules such as DNA, RNA and enzymes are normally the targets of antimicrobial peptides in mechanisms of action that do not involve cell lysis. Bac 5 and Bac 7 are known to inhibit protein and RNA synthesis of *E coli* and *klebsiella pneumonia*. Bufforin II is also known to inhibit cellular functions upon binding to RNA and DNA. Histatins target the mitochondria and are known to cause efflux of ATP. Figure 1.7 summarises the molecular mechanisms of several antimicrobial peptides.

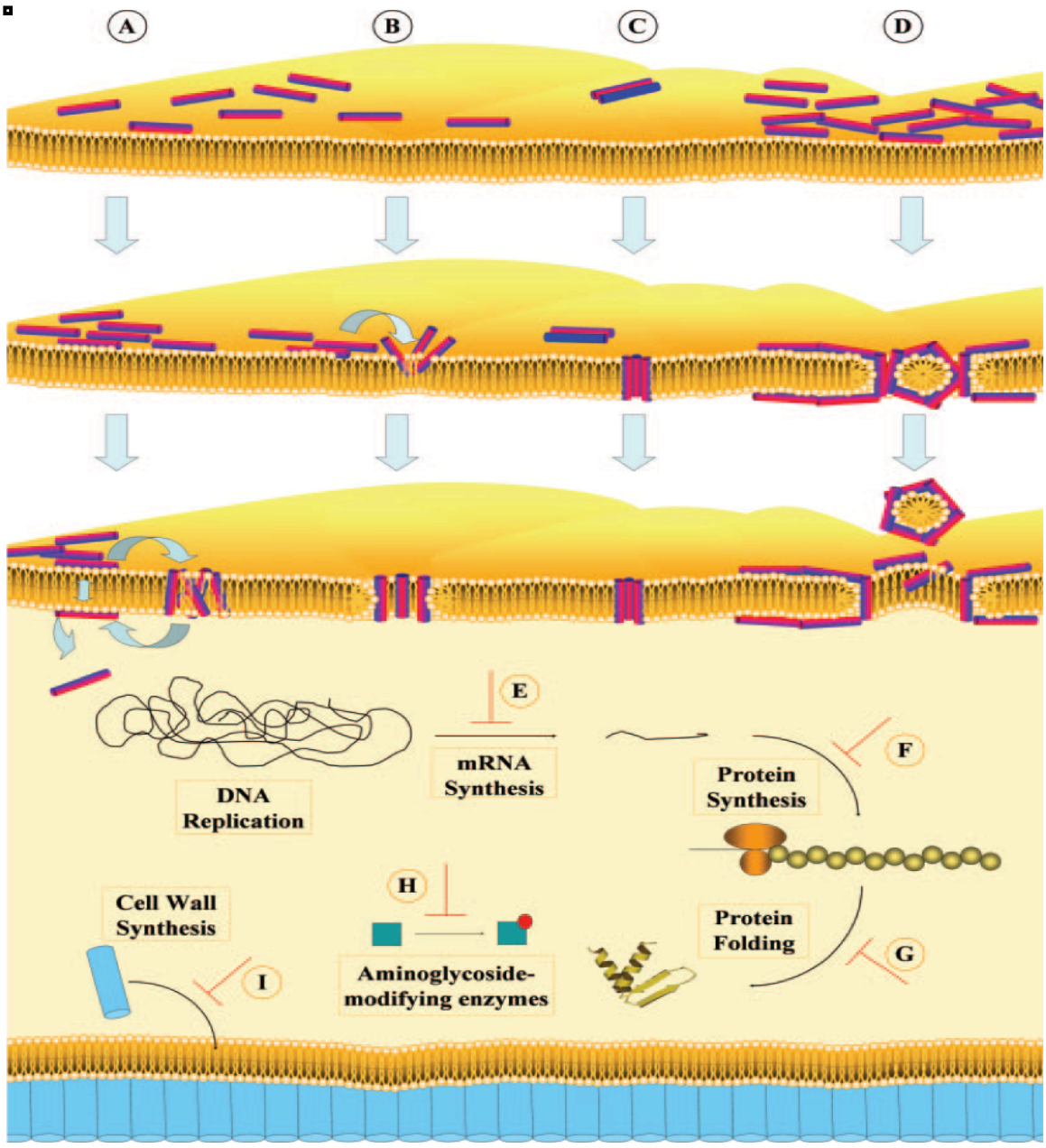

Figure 1.7: The molecular mechanisms of action of antibiotic peptides. The bacterial membrane is represented as a yellow lipid bilayer with the peptides shown as cylinders, where the hydrophilic regions are coloured red and the hydrophobic regions are blue. Cell wall-associated peptidoglycan molecules are depicted as purple cylinders. Models to explain mechanisms of membrane permeabilization are indicated by A to D which correspond to aggregate, torroidal, barrel starve and carpet models respectively) . Models represented by E to I do not permeabilize the membrane by target processes inside the cell. E mRNA synthesis, F protein synthesis, G protein folding, H aminoglycoside-modifying enzymes and I cell wall synthesis. The illustration was taken from[47].

1.7 Aims of the study

The need to come up with new and novel antibiotics that utilize unique mechanisms, to which bacteria cannot generate resistance, was the main motivation of this study. Tyrocidine peptides are non-selective antibiotics that have such properties. However, very limited information is available about their mechanism of action. Knowledge of structure, self-assembly in aqueous and membrane mimetic environments, and physicochemical properties plays a major role towards understanding the molecular mechanism of action of antimicrobial peptides.

The major objectives of this study were:

I. To investigate the structure of tyrocidine using NMR spectroscopy and molecular modeling in aqueous and membrane-mimetic environments.

II. To investigate the self-assembly of tyrocidine in aqueous and membrane-mimetic environments using molecular modeling and NMR spectroscopy.

III. To investigate the possibility of channel formation using homology modeling and molecular dynamics of antimicrobial peptides.

IV. To investigate the effect of metal binding on the structure of tyrocidine C peptide using quantum mechanics and NMR.

1.8 References

1. Winters C, Gelband H. Part1. the global antibiotic resistance partnerships (GARP). South African Medical Journal 2011;101:556-7.
2. The bacterial challenge: Time to react. The Lancet 2009;374:1868.
3. Furlow B. Preventing drug-resistant infections in health care. Radiologic Technology.2009;80:217-37.
4. Rammelkamp CH, Weistein L. Toxic effects of tyrothricin, gramicidin and tyrocidine. The Journal of Infectious Diseases 1942;71:166-73.
5. Van Epps HL. René Dubos: Unearthing antibiotics. The Journal of Experimental Medicine 2006;203:259.
6. Theuretzbacher U. Future antibiotics scenarios: Is the tide starting to turn? International Journal of Antimicrobial Agents 2009;34:15-20.
7. Livermore DM, Warner M, Mushtaq S, Doumith M, Zhang J, Woodford N. What remains against carbapenem-resistant enterobacteriaceae? Evaluation of chloramphenicol, ciprofloxacin, colistin, fosfomycin, minocycline, nitrofurantoin, temocillin and tigecycline. International Journal of Antimicrobial Agents 2011;37:415-9.
8. Livermore DM. Has the era of untreatable infections arrived? Journal of Antimicrobial Chemotherapy 2009;64:i29-36.
9. Ursula T. Resistance drives antibacterial drug development. Current Opinion in Pharmacology 2011;11:433-8.
10. Giuliani A, Pirri G, Nicoletto SF. Antimicrobial peptides: An overview of a promising class of therapeutics. Central European Journal of Biology 2007;2:1-33.

11. Epand RM, Vogel HJ. Diversity of antimicrobial peptides and their mechanisms of action. Biochemica Et Biophysical Acta-Biomembranes 1999;1462:11-28.
12. Hancock REW, Lehrer R. Cationic peptides: A new source of antibiotics. Trends Biotechnology 1998;16:82-8.
13. van't Hof W, Veerman ECI, Helmerhorst EJ, Amerongen AVN. Antimicrobial peptides: Properties and applicability. Journal of Biological Chemistry 2001;382:597-619.
14. Rizo J, Gierasch LM. Constrained peptides: Models of bioactive peptides and protein substrucures. Annual Review of Biochemistry 1992;61:387-418.
15. Romeo D, Skerlavaj B, Bolognesi M, Gennaro R. Structure and bactericidal activity of an antibiotic dodecapeptide purified from bovin neurophilis. Journal of Biological Chemistry 1988;263:9573-5.
16. Schluesener HJ, Radermacher S, Melms A, Jung S. Leukocytic antimicrobial peptides kill autoimmune T cells. Journal of Neuroimmunology 1993;47:199-202.
17. Kawano K, Yoneya Y, Miyata T. Antimicrobial peptide, tachyplesin I, isolated from hemocytes of the horseshoe crab (tachypleus tridents). Journal of Biological Chemistry 1990;265:15635-367.
18. Miyata T, Tokunaga F, Yoneya T, Yishokawa K, Iwanaga S, Niwa M, Takao T, Shimonishi Y. Antimicrobial peptides, isolated from horseshoe crab hemocytes, tachyplesin II, and polyphemusins I and II: Chemical structures and biological activity. Journal of Biochemistry 1989;106:663-8.
19. Kokryakov VN, Hawig SS, Panyutic EA, Shevshenko AA, Aleshina GM, Shamova OV, Korneva HA, Lehrer RI. Protegrins: Leukocyte antimicrobial peptides that

combine features of corticostatic defensins and tachyplesins. FEBS Letters 1993;327:231-6.

20. Storici P, Zanetti M. A novel cDNA sequence encoding a pig leukocyte antimicrobial peptide with a cathelin-like pro-sequence. Biochemical and Biophysical Research Communications 1993;196:1363-8.
21. Zhao C, Lui L, Lehrer RI. Identification of a new member of the protegrin family by cDNA cloning. FEBS Letters 1994;346:285-8.
22. Lehrer RI, Lichtenstein AK, Ganz T. Defensins: Antimicrobial and cytotoxic peptides of mammalian cells. Annual Review of Immunology 1993;11:105-28.
23. Fehlbaum P, Bulet P, Michait L, Lagueux M, Brekaert WF, Hetru C, Hoffmann JA. Insect immunity. septic injury of drosophila induces the synthesis of a potent antifungal peptide with sequence homology to plant antifungal peptides. Journal of Biological Chemistry 1994;265:33159-63.
24. Leaderach A, Andreotti AH, Fulton DB. Solution and micelle-bound structures of tachyplesin I and its active aromatic linear derivatives. Biochemistry 2002;41:12359-68.
25. Bong DT, Clark TD, Granja JR, Ghadiri MR. Self-assembling organic nanotubes. Angewandte Chemie International Edition 2001;40:988-1011.
26. Ghadiri MR, Granja JR, Milligan RA, McRee DE, Khazanovich N. Self-assembling organic nanotubes based on a cyclic peptide architecture. Nature 1993;366:324-7.
27. Khuran E, Nielsen SO, Ensing B, Klein ML. Self-assembling cyclic peptides: Molecular dynamics studies of dimers in polar and nonpolar solvents. The Journal of Physical Chemistry B 2006;110:18965-72.

28. Tarek M, Maigret B, Chipot C. Molecular dynamics investigation of an oriented cyclic peptide nanotube in DMPC bilayers. Biophysical Journal 2003;85:2287-98.
29. Fernandez-Lopez S, Kim H, Choi EC, Delgado M, Granja JR, Khasanov A, Kraehenbuehl K, Long G, Weinberger DA, Wilcoxen KM, et al. Antibacterial agents based on the cyclic D,L-alpha-peptides architecture. Nature 2001;412:452-5.
30. Raaijmakers JM, de Bruijn I, de Kock MJD. Cyclic lipopeptide production by plant-associated pseudomonas spp.: Diversity, activity, biosynthesis, and regulation. Molecular Plant-Microbe Interactions 2006;19:699-710.
31. Hotchkiss RD, Dubos RJ. Bactericidal fractions from an aerobic sporulating bacillus. Journal of Biological Chemistry 1940;136:803-4.
32. Dubos JR. Studies on a bactericidal agent extracted from a soil bacillus. The Journal of Experimental Medicine 1939;70:1-10.
33. Dubos RJ. Studies on a bactericidal agent extracted from a soil bacillus. The Journal of Experimental Medicine 1939;70:11-7.
34. Dubos RJ, Hotchkiss RD. The isolation of bactericidal substances from cultures of bacilus brevis. The Journal of Experimental Medicine 1941;01:155-62.
35. Katsu T, Ninomiya C, Kuroko M, Kabayashi H, Hirota T, Fujita Y. Action mechanism of amphipathic peptides gramicidine S and melittin on erythrocyte membrane Biochimica Et Biophysica Acta (BBA) - Biomembranes 1988;939:57-63.
36. Prenner EJ, Jelokhani-Niaraki M, Kondejewski LH, Hodges RS, McElhaney RN. Membrane interactioncs of gramicidin S and biologically active analogs. Biophysical Journal 2000;78:321A.

37. Tishchenko GN, Andrianov VI, Vainstein BK, Woolfson MM, Dodson E. Channels in the gramicidine S-with-urea transmembrane ion transport . Acta Crystallographica Section D 1997;53:151-9.

38. Josh K, Semrouni D, Ohanessian G, Clavaguera C. Structures and IR spectra of the gramicidins peptide: Pushing the quest for low-energy conformations. The Journal of Physical Chemistry B 2012;116:483-90.

39. Prenner EJ, Lewis RNAH, Jelokhani-Niaraki., Hodges RS, McElhaney RN. Cholestrol attenuates the interaction of the antimicrobila peptide gramicidin S with phospholipid bilayer. Biochimica Et Biophysica Acta (BBA) - Biomembranes 2001 12/15;1510:83-92.

40. Tang XJ, Thibault P, Boyd RK. Characterization of the tyrocidine and gramicidin fractions of the tyrothricin complex from bacillus brevis using liquid chromatography and mass spectroscopy. International Journal of Mass Spectrometry and Ion Processes 1992;122:153-79.

41. Dubos RJ, Hotchkiss RD. The production of bactericidal substances by aerobic sporulating bacilli. Journal of Experimental Medicine 1941;73:629-40.

42. Marques MA, Citron DM, Wang CC. Development of tyrocidine A analogues with improved antibacterial activity. Bioorganic & Medicinal Chemistry 2007;15(21):6667-77.

43. [Internet]; c1996 [cited 5 March 2012] Available from: http://www.cryst.bbk.ac.uk/PPS2/course/section8/ss-960531_5.html.

44. 76-456/731 Biophysical Methods - Protein structure component [Internet]; c1998 [cited 5 March 2012]. Available from: http://www.chembio.uoguelph.ca/educmat/phy456/PHY456.htm.
45. Acharya KR, Stuart DI, Walker NPC, Lewis M, Phillips DC. Refined structure of baboon alpha-lactalbumin at 1.7 angstrom resolution: Comparison with C-type. Journal of Molecular Biology 1989;208:99-127.
46. Yeaman MR, Yount NY. Mechanisms of antimicrobial peptide action and resistance. Pharmacological Reviews 2003;55:27-55.
47. Jenssen H, Hamill P, Hancock REW. Peptide antimicrobial agents. Clinical Microbiology Reviews 2006;19:491-511.
48. Powers JS, Hancock REW. The relationship between peptide structure and antibacterial activity. Peptides 2003;24:1681-91.
49. Fink J, Memifield RB, Boman A, Boman HG. The chemical synthesis of cecropin D and an analog with enhanced antibacterial activity. The Journal of Biological Chemistry 1988;264:6260-7.
50. Iwahori A, Hirota Y, Sampe R, Miyano S, Takahashi N, Sasatsu M, Kondo I, Numao N. On the antibacterial activity of normal and reversed magainin 2 analogs against helicobacter pylori. Biological & Pharmaceutical Bulletin 1997;20:805-8.
51. Matsuzaki K, Sugishita K, Harada M, Fujii N, Miyajima K. Interactions of an antimicrobial peptide, magainin 2, with outer and inner membranes of gram-negative bacteria. Biochimica Et Biophysica Acta (BBA) - Biomembranes 1997;1327:119-30.

52. Matsuzaki K, Yoneyama S, Fujii N, Miyajima K, Yamada K, Kirino Y, Anzai K. Membrane permeabilization mechanisms of a cyclic antimicrobial peptide, tachyplesin I, and its linear analog. Biochemistry 1997;36:9799-806.

53. Dathe M, Nikolenko H, Meyer J, Beyermann M, Bienert M. Optimization of the antimicrobial activity of magainin peptides by modification of charge. FEBS Letters 2001;501:146-50.

54. Brogden KA, Ackermann M, Huttner KM. Small, anionic, and charge-neutralizing propeptide fragments of zymogens are antimicrobial. Antimicrobial Agents and Chemotherapy 1997;41:1615-7.

55. Eisenberg D. Three-dimensional structure of membrane and surface proteins. Annual Review of Biochemistry 1984;53:595-623.

56. Javadpour MM, Juban MM, Lo WC, Bishop SM, Alberty JB, Cowell SM, Becker CL, McLaughlin ML. De novo antimicrobial peptides with low mammalian cell toxicity. Journal of Medicinal Chemistry 1996;39:3107-13.

57. Pathak N, Salas-Auvert R, Ruche G, Janna MH, McCarthy D, Harrison RG. Comparison of the effects of hydrophobicity, amphipathicity and alpha helicity, on the activities of antimicrobial peptides. Proteins 1995;22:182-6.

58. Cornut I, Buttner K, Dasseux JL, Dufourcq J. The amphipathic alpha-helix concept. application to the de novo design of ideally amphipathic leu, lys peptides with hemolytic activity higher than that of melittin. FEBS Letters 1994;349:29-33.

59. Wieprecht T, Dathe M, Krause E, Beyermann M, Maloy WL, MacDonald DL, Bienert M. Modulation of membrane activity of amphipathic, antibacterial peptides by slight modifications of the hydrophobic moment. FEBS Letters 1997;417:135-40.

60. Subbalakshmi C, Nagaraj R, Sitaram N. Biological activities of C-terminal 15-residue synthetic fragment of melittin: Design of an analog with improved antibacterial activity. FEBS Letters 1999;448:62-6.

61. Skerlavaj B, Gennaro R, Bagella L, Merluzzi L, Risso A, Zanetti M. Biological characterization of two novel cathelicidin-derived peptides and identification of structural requirements for their antimicrobial and cell-lytic activities. Journal of Biological Chemistry 1996;271:28375-81.

62. Helmerhorst EJ, Reijnders IM, Van 't Hof W, Veerman ECI, Nieuw Amerongen AV. Acritical evaluation of the lytic activity of cationic antimicrobial peptides against candida albicans cells and human erythrocytes. FEBS Letters 1999;449:105-9.

63. Shai Y. Mechanism of membrane permetion and pore formation by antimicrobial peptides. In: L. K. Tamm, editor. Protein-lipid interactions. Weinheim, Germany: Wiley-VCH; 2005.

64. Béven L, Helluin O, Molle G, Duclohier H, Wróblewski H. Correlation between antibacterial activity and pore sizes of two classes of voltage-dependent channel forming peptides. Biochemica Et Biophysical Acta 1999;1421:53-63.

65. Sansom MS. The biophysics of peptide models of ion channels. Progress in Biophysics and Molecular Biology 1991;55:139-235.

66. Yang L, Harroun TA, Weiss TM, Ding JL, Huang HW. Barrel stave model or toroidal model ? A case study on melittin pores. Biophysical Journal 2001;81:1475-85.

67. Rapaport D, Shai Y. Interaction of fluorescently labeled pardaxin and its analogues with lipid bilayers. Journal of Biological Chemistry 1991;266:23769-75.

68. Saint N, Marri L, Marchini D, Molle G. The antimicrobial peptide ceratotoxin A displays an alamethicin-like behaviour in lipid bilayers. Peptides 2003;24:1779-84.

69. Ludtke JS, He K, Heller WT, Harroun TA, Yang L, Huang HW. Membrane pores induced by magainin. Biochemistry 1996;35:13723-8.

70. Yang L, Weiss TM, Lehrer RI, Huang HW. Crystallization of antimicrobial pores in membranes: Magainin and protegrin. Biophysical Journal 2000;79:2002-9.

71. Gazit E, Bach D, Kerr ID, Sansom MS, Chejanovsky N, and Shai Y. The α-5 segment of bacillus thuringiensis δ-endotoxin: In vitro activity, ion channel formation andmolecular modeling. Biochemical Journal 1994;304:895-902.

72. Strahilevitz J, Mor A, Nicolas P, Shai Y. Spectrum of antimicriobial activity and assembly of dermaseptin-b and its precusor form in phospholipid membranes. Biochemistry 1994;33:10951-60.

73. Hancock REW, Chapple DS. Peptide antibiotics. Antimicrobial Agents and Chemotherapy 1999;43:1317-23.

74. Rozek A, Friedrich CL, Hancock RE. Structure of the bovine antimicrobial peptide indolicidin bound to dodecylphosphocholine and sodium dodecyl sulfate micelles. Biochemistry 2000;39:15765-74.

Chapter 2

Experimental and Computational Methods

2.1 Nuclear Magnetic Resonance

NMR spectroscopy has become one of the most widely used research techniques because of the vast amount of information it provides about the chemical structure, dynamics, reaction state and chemical environments of peptides and proteins.[1, 2] Despite providing a vast amount of information, one other advantage it has is its ability to be utilized under different experimental conditions such as solvents, temperature and pH.[3]

2.1.1 ^{1}H NMR

The typical nucleus in NMR, the most often used and most easy to work with, is the hydrogen nucleus mainly because it gives one of the strongest resonances.[4] The values obtained from NMR, essential for the structure determination, are proton – proton distances. However, in case of biomolecules these data must be obtained from 2D spectra, due to many overlapping signals in the 1D spectrum of proteins. Dipolar coupling results from the intrinsic magnetic field of each nucleus. If two nuclei are close enough they can interact and influence each other. After irradiation of one of the nuclei, polarization is transferred, via dipolar coupling, to the other nucleus. This phenomenon is called the nuclear Overhauser effect (nOe). The nOe interaction is proportional to $1/r^6$, where r is a distance between the two nuclei. For this reason ^{1}H – ^{1}H nOe interactions are only observed for interatomic distances shorter than 5 – 6 Å. nOe can be measured using

1D pulse sequences but is generally measured using 2D techniques. The most common pulse sequences are NOESY (Nuclear Overhuaser enhancement spectroscopy) and ROESY (rotating frame Overhuaser spectroscopy). As nOe build-up is also dependent on the rotational correlation time, the latter is more useful for small molecules.

Correlation spectroscopy (COSY) is also used to relate protons that are scalar coupled to each other. Various embellishments of COSY are used in practice, including quantum filtered COSY, and in particular double quantum filtered COSY (DQF-COSY), to simplify and improve spectral resolution, although at a small loss of sensitivity. Another method called Total correlation spectroscopy (TOCSY) correlates all protons within an individual spin system by means of complete magnetization transfer induced by an applied mixing pulse during a spin lock period.

2.1.2 Chemical shift (δ)

Chemical shift (δ in ppm units) is the basic parameter measured by NMR. The magnitude of the shift depends upon the type of nucleus and the details of the electron motion in the nearby atoms and molecules. Based on this, the chemical shift of individual nuclei reflects the primary and secondary structure of amino acids in a peptide or protein. The study of chemical shifts has produced a large store of information about the chemical bonds and the structure of molecules. Figure 2.1 shows the range of typical chemical shifts for ^{1}H resonances.

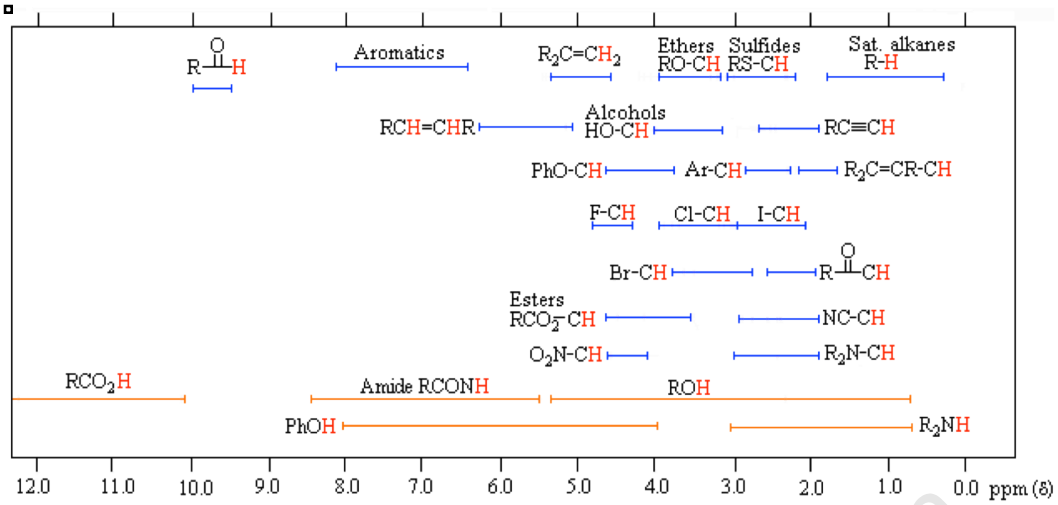

Figure 2.1: The range of typical chemical shifts for ^{1}H resonances. Adopted from [4]

2.1.3 NMR titration

NMR titration spectra are useful for obtaining thermodynamic data. Ligand binding induces secondary chemical shifts in nuclei that are located close to the binding site. The signals of the ligand also appear in the spectrum during the titration. If the exchange between the bound and free form of the ligand is fast on the NMR timescale, average signals of the free and bound molecule appear in the spectrum. From the change of chemical shift the stoichiometry and binding constant can be determined.

2.2 Computational Methods

2.2.1 Molecular Mechanics

Molecular mechanics is one of the primary tools that can be used to model large macromolecules such as proteins and nucleic acids. It disregards the quantum properties of electrons and considers a simplified description of nuclei and electrons as point charges based on the Born-Oppenheimer approximation.[5] The simplified description of the atomic particles enables one to avoid using quantum mechanics, which is extremely slow when modeling large molecules such as proteins. The point charges are joined together by springs regarded as bonds and other potential functions that describe van der Waals and electrostatic interactions. To describe the potential energy functions of a system, bond distances, bond angles and other parameters are first determined empirically based on specific sets of atoms. The experimentally determined parameters and the potential functions used to describe the potential energy function of a system is called a forcefield.

2.2.1.1 Force field

A forcefield is basically defined as a collection of functions and parameters that are used to determine the potential energy of a system. The individual terms that are used in determining the total energy of a system can be subdivided into two classes namely; bonded and non-bonded interactions. The bonded interactions make up the first four terms in a general force field equation. These include; bond stretching, angle bending, proper and improper dihedral angles. The last two terms in the force field equation, the electrostatic and van der Waals interactions are classified as non-bonded interactions.

Bonded Interactions

Bonded interactions are based on a fixed list of atoms. They include bond stretching, bond angle and torsional angle interactions.

Bond stretching can be described by a harmonic potential that takes into consideration the stretching and compression of bonds and treats atoms as if they are joined by springs. The energy of the bond varies with the square of its displacement from the natural bond length. Other functions such as the Morse potential and addition of quartic terms to the harmonic potential can also be used to describe bond stretching. They are however computationally more expensive compared to the harmonic potential.

$$v(l) = \frac{k}{2}(l - l_0)^2 \tag{2.1}$$

Angle bending can also described by a harmonic potential and the energy of each bond in the system is defined by a force constant and reference value.

$$v(\theta) = \frac{k}{2}\left(\theta_i - \theta_{i,0}\right)^2 \tag{2.2}$$

Torsional/dihedral potentials are used to describe the energy contributions of proper and improper dihedral angles. Some molecular mechanics force field do not use torsional potentials, they however depend on non-bonded interactions between 1-4 atoms in a dihedral angle to achieve the desired energy profile. Torsional potentials are frequently determined using a cosine series expansion.

$$v(w) = \sum_{n=0}^{N} \frac{V_n}{2}[1 + \cos(nw - \gamma)] \tag{2.3}$$

The improper torsions are generally shown in the form of equation 2.4 below. This function keeps the improper torsion angle at 0^0 or 180^0.

$$v(w) = k(1 - cos2w) \tag{2.4}$$

Non-bonded interactions

Electrostatic interactions describe the forces experienced by atoms as a result of their charges. They are treated using the classical pair-wise additive Coulombic term.

$$v(r_{ij}) = \frac{q_i q_j}{4\varepsilon_0 r_{ij}} \tag{2.5}$$

Van der Waals interactions are used to describe London forces. They generally describe attractive and repulsive forces between instantaneous dipoles. The Lennard Jones potential is mainly used to treat van der Waals interactions. They are often truncated at a cutoff distance. Different functions can also be utilized to smooth truncated forces and thermal noise around the cutoff radius.

$$v(r) = 4\varepsilon\left[\left(\frac{\sigma}{r}\right)^{12} - \left(\frac{\sigma}{r}\right)^{6}\right] \tag{2.6}$$

The general class1 forcefield can be described by equation 2.7 below

$$V(x) = \sum_{bonds} \frac{k_i}{2}\left(l_i - l_{i,0}\right)^2 + \sum_{angles} \frac{k_i}{2}\left(\theta_i - \theta_{i,0}\right)^2 + \sum_{torsions} \frac{V_n}{2}\left[1 + \cos(n\omega - \gamma)\right] + \sum_{i=j}^{N}\sum_{j=i+1}^{N}\left(4\varepsilon_{ij}\left[\left(\frac{\sigma_{ij}}{r_{ij}}\right)^{12} - \left(\frac{\sigma_{ij}}{r_{ij}}\right)^{6}\right] + \frac{q_i\, q_j}{4\pi\, \varepsilon_0 r_{ij}}\right) \tag{2.7}$$

Constraints and restraints

Constraints are used to fix the length of bonds or angles to particular values during a simulation. Restraints are different from constraints and are used to keep the restrained entities as close as possible to a particular value. Restraints are implemented by adding an additional term to the potential energy function of a system and a penalty is applied to the energy of the system when the bond or angle deviates from the reference value. Distance restraints are normally used to refine structures using NMR data. NOESY data is used to generate the target distance.[6]

The relationships below show how the restraints can be applied. The potential form for distance restraints is quadratic below a specified lower bound and between two specified upper bounds and linear beyond the largest bound.[7]

$$V_{dr}(r_{ij}\ ) = \begin{cases} \frac{1}{2}k_{dr}(r_{ij} - r_0)^2 & for \quad r_{ij} < r_0 \\ 0 & for\ r_0 \le r_{ij} < r_1 \\ \frac{1}{2}k_{dr}(r_{ij} - r_1)^2 & for\ r_1 \le r_{ij} < r_2 \\ \frac{1}{2}k_{dr}(r_2 - r_1)(2r_{ij} - r_2 - r_1) & for\ r_2 \le r_{ij} \end{cases} \tag{2.8}$$

2.2.2 Energy minimization

Energy minimization is performed to remove steric clashes that may cause instabilities of the system during molecular dynamics. This can be achieved by searching for the global minimum of the potential energy function of the macromolecule. The derivative of the potential energy function is zero at the global minimum. However, the dimensionality of the configurational space of any macromolecule and the number of local minima it can have is so high that it is impossible to sample the whole conformational space and guarantee the determination of the global minimum in any practical amount of time. Most energy minimization methods determine the nearest local minimum, which is the minimum that can be reached by systematically moving down the steepest local gradient of the potential energy function. Some of the energy minimization methods used include steepest descents and L-BFGS.

Steepest descents

Steepest descents energy minimization method falls under what are called first order minimization algorithms. It takes a step in the direction parallel to the force without any consideration of the history built up in previous steps. The step size is adjusted such that the search is fast, but the motion is always downhill.

L-BFGS

The L-BFGS algorithm works by successively creating better approximations of the Hessian matrix. It achieves this by using a fixed number of corrections from previous steps.

2.2.3 Simulated annealing

Simulated annealing is a technique that is used to find the global minimum energy of a molecular system. During simulated annealing, a system is heated to high temperature allowing it to occupy high-energy states of its conformational space and traverse energy barriers.[6, 8, 9] The system is then gradually cooled and, as the temperature falls, the system is likely to occupy the lowest energy conformation. It is expected that at absolute zero the system should occupy the lowest energy state, which corresponds to the global minimum energy conformation.[6] However, simulated annealing does not always give low energy conformations from a single calculation and generally the simulation is repeated several times to get the true global minimum energy conformations from an ensemble.[6]

2.2.4 Classical molecular dynamics

Molecular dynamics simulation is used to determine the time evolution of a molecular system. The trajectory of a system is obtained by solving the differential equations based on Newton's laws of motion.[6, 7]

$$F = ma \tag{2.9}$$

$$\frac{d^2x_i}{dt^2} = \frac{F_{x_i}}{m_i} \tag{2.10}$$

The differential equation (2.10) above describes the variation of the motion of particle i of mass m_i with time t in the x coordinate. The particle is being acted upon by a force F_{x_i}. Solving the equation gives the position, velocity and acceleration of the particle at any particular instant during the trajectory.

2.2.4.1 Algorithms

In molecular dynamics, the potential energy function is made up of 3N atomic positions, which makes it very complicated to obtain an analytical solution to the equations of motion. The solutions can more easily be obtained numerically based on a number of integration algorithms that have been developed from the Taylor series expansion. These algorithms include; the Verlet algorithm, the leapfrog algorithm, velocity Verlet algorithm and the Beeman's algorithm.[10-12]

The Verlet algorithm uses positions and accelerations at time t and the positions from the time $t - \delta t$ to calculate new positions at time $t + \delta t$ (eqn 2.11). The Verlet algorithm is not very precise but is probably one of the most widely used time integration algorithms.

$$r(t + \delta t) = 2r(t) - r(t - \delta t) + a(t)\delta t^2 \tag{2.11}$$

The leapfrog algorithm is cheaper and that makes it more popular when modeling large systems. In this integration method, the velocities are determined at time $t + \frac{1}{2}\delta t$ and used to calculate the positions r at time $t + \delta t$ (equations 2.12 and 2.13).

$$r(t + \delta t) = r(t) + v\left(t + \tfrac{1}{2}\delta t\right)\delta t \tag{2.12}$$

$$v\left(t + \frac{1}{2}\delta t\right) = v\left(t - \frac{1}{2}\delta t\right) + a(t)\delta t \tag{2.13}$$

The velocity Verlet algorithm calculates the position r, velocity v and acceleration a at time $(t + \delta t)$ the same way it does at time t with no compromise in precision (equations 2.14 and 2.15).

$$r(t + \delta t) = r(t) + v(t)\delta t + \tfrac{1}{2}a(t)\delta t^2 \tag{2.14}$$

$$v(r + \delta t) = v(t) + \frac{1}{2}[a(t) + a(t + \delta t)]\,\delta t \tag{2.15}$$

Beeman's algorithm is very similar to the Verlet algorithm. It is also very good with energy conservation and calculates velocities accurately. The downside of this algorithm is that it is very expensive because of the complexity of its equations 2.16 and 2.17.

$$r(t + \delta t) = r(t) + v(t)\delta t + \frac{3}{2}a(t)\delta t^2 - \frac{1}{b}a(t - \delta t)\delta t^2 \tag{2.16}$$

$$v(t+\partial t) = v(t) + v(t)\partial t + \frac{1}{3}a(t)\partial t + \frac{5}{6}a(t)\partial t - \frac{1}{6}a(t-\partial t)\partial t \quad (2.17)$$

2.2.5 Replica exchange molecular dynamics (REMD)

Replica exchange molecular dynamics (REMD) [13] is mainly used to study systems that have rugged potential energy surfaces. When such systems are simulated at low temperature they normally get trapped in conformations of local energy minima. The REMD algorithm is a non-Boltzmann sampling method, which allows a system to perform a random walk on the energy surface.[14-16] In REMD, a given number of replicas are simulated at different temperatures. The replicas are exchanged between adjacent temperatures at a predetermined frequency based on the probability given by the equation below

$$p(i,j) = min\left\{1.0, exp\left[\frac{1}{k_B T_i} - \frac{1}{k_B T_j}\right](E_i - E_j)\right\} \quad (2.18)$$

After REMD simulations, the Weighted Histogram Analysis Method (WHAM) [17, 18]is used to extract thermodynamic and folding properties of proteins and peptides from the various simulations. This then allows for the determination of the global minimum conformation of a system.

2.2.6 Center of mass pulling

Center of mass (COM) pulling or Steered molecular dynamics (SMD) is commonly used to study processes such as ligand-protein dissociation and protein-protein interactions.[19-21]

In ligand-protein dissociation SMD simulation, the ligand is initially restrained to its center of mass by a harmonic potential. The COM of the ligand is then moved in a predetermined direction x at a constant speed v by a force F that corresponds to a harmonic spring of stiffness K.[20] The displacement of the ligand from its initial position allows it to explore new contacts along the reaction pathway.[20]

$$F = K(x_0 + vt - x) \tag{2.19}$$

As the ligand dissociates, the pulling force is expected to decrease. However if the force is not large enough it continues to increase with increasing time until it is large enough to dissociate the ligand. The force vs time profile can then be plotted from which qualitative information about the ligand dissociation can be extracted. The non-equilibrium conditions under which SMD simulations are performed mean that it is not possible to extract quantitative information such as thermodynamic properties without large errors.[22] The errors can be reduced when weak pulling forces that cause very small changes to the ligand are applied very slowly. Yang et al.[23, 24] described a method that can be used to extract thermodynamic data from non-equilibrium SMD simulations, however several simulations have to be performed.

2.2.7 Potential of mean force

The potential of mean force (PMF) or free energy can be defined as the potential that gives an average force over all the configurations of a given system.[25]

Different ways of computing PMF have been proposed. One method involves computing the variation of free energy with distance between two particles. Generally the PMF, $w(r)$can be computed from the probability distribution function as shown below[6, 26, 27]

$$P(r) = Ce^{-\beta w(r)} \tag{2.20}$$

$$w(r) = -k_B T ln P(r) + C \tag{2.21}$$

where,

$$P(r) = \frac{\int \delta(r) e^{-\beta V(q)} d\boldsymbol{q}}{\int e^{-\beta V(q)} d\boldsymbol{q}} \tag{2.22}$$

However this method does not always succeed in giving accurate PMF because the whole conformational space will not be sampled properly since MD simulations generally tend to avoid high-energy regions of conformational space. Umbrella sampling methods have been generated to circumvent this problem.

2.2.7.1 Umbrella sampling

Umbrella potential introduces a biasing potential to the potential energy of a system to allow for sampling of unfavorable states [6, 28, 29]

$$V'(r) = V(r) + W(r) \tag{2.23}$$

where $W(r)$ is the biasing potential

The biasing potential allows the system to sample a small area of the conformational space. This gives a non-Boltzmann distribution for each sampled space also known as a window. A series of overlapping windows are generated along the reaction coordinate. Each window is biased by a different biasing potential that centers the system within a particular space. The resulting distributions are then unbiased to do away with the non-Boltzmann factor before being combined to give the PMF. The Weighted Histogram Analysis Method (WHAM) is normally used to compute the total unbiased distribution and PMF.[17] It should be noted that umbrella sampling is a Boltzmann sampling method in the presence of a biasing potential.

2.2.8 Simulation setup in Molecular Dynamics

2.2.8.1 Periodic boundary conditions

Periodic boundary conditions reduce edge effects when modeling systems of finite sizes.[6, 7, 30] This is achieved by placing the system into a space filling box surrounded by copies of itself in three dimensions. This allows a particle leaving from one end of the simulation box to re-enter on the opposite side.[6, 30] It is very important to take into account the size of the box such that the particles of the system do not interact with their periodic images as this can result in artifacts due to unphysical dynamics. Making use of the minimum image convention, which states that a particle in the central box must not see more than one image of every other particle within the box, can do this.[30]

2.2.8.2 Temperature and pressure coupling

Different statistical ensembles are used when performing MD simulations. Each ensemble has certain macroscopic environmental constraints of thermodynamic parameters for the system and these include total energy (E), number of particles (N), pressure (P), temperature (T) and volume (V). An example of an ensemble is the NVE or microcanonical ensemble, which depicts a system that contains a constant number of particles, in a fixed volume and total energy. This particular ensemble does not correspond to the experimental conditions of most simulated systems.

Another ensemble, NPT or canonical ensemble is commonly used in MD simulations. It has a fixed number of particles, pressure and temperature. This ensemble is used to simulate physical systems such as biomembranes and biomolecules. During simulations, temperature can deviate from that required in a particular simulation due to several reasons such as drift during equilibration, external or frictional forces, and integration errors. In order to control the temperature, several coupling schemes have been developed and these include Berendsen, Nose-Hoover and Verlet coupling schemes. The Berendsen temperature coupling does not yield phase space distributions corresponding to any known ensemble and should be used with caution (in particular in conjunction with REMD).

The Berendsen temperature coupling corrects the temperature based on the relationship below

$$\frac{dT}{dt} = \frac{T_0 - T}{\tau} \tag{2.24}$$

where, T_0 is the required temperature

T is the temperature at a particular time

τ is the time constant

In the same way as temperature coupling, systems have to be coupled to a pressure bath. Several coupling schemes have also been developed. These include Berendsen, and Parrinello-Rahman pressure coupling schemes.

The Berendsen pressure coupling works in a similar way to rescale the pressure of the system

$$\frac{dP}{dt} = \frac{P_0 - P}{\tau_p} \tag{2.25}$$

where, T_0 is the required temperature

T is the temperature at a particular time

τ is the time constant

2.2.8.3 Choice of time step

Time step is one of the most important parameters in MD simulations, as using a wrong time step can result in artifacts. A very small time step will limit the phase space that can be covered by the trajectory while a very large time steps may cause instabilities in the integration algorithm due to high energy overlaps between atoms.[6, 7] In general bonds are constrained to their equilibrium values and the rest of the degrees of freedom are allowed to vary under the influence of intramolecular and intermolecular forces. This makes it possible to use longer time steps. Different time steps have been suggested depending on the system being simulated and they can vary from 1×10^{-14} s to 5×10^{-16} s [6].

2.2.8.4 Solvation

Solvation plays a big role during molecular modeling of biomolecules since solvents are a major part of their native environment. There are basically two types of solvation methods that can be applied; namely implicit and explicit solvation methods. The implicit method is also known as the continuum method. It is basically used for the determination of thermodynamic properties such as free energy of solute-solvent interactions in several biological processes that range from protein folding to drug transport. This method is generally cheaper compared to explicit solvation methods. An example of an implicit solvation method is the Generalized Born model. Explicit solvation methods treat solvent molecules explicitly (individually) which increases the size of the system. They give more realistic interactions such as hydrogen bonding between solvent molecules and the biomolecules. Several explicit models are in use and these include SPC, SPC/E, TIP3P and TIP4P.

2.3 References

1. Dyson HJ, Wright PE. Two-dimensional NMR spectroscopy applications for chemists and biochemists. New York: VCH; 1994.

2. Dyson HJ, Wright PE. Defining solution conformations of small linear peptides. Annual Review Biophysics and Biophysical Chemistry 1991;20:519-38.

3. Wuthrich K. NMR of proteins and nucleic acids. New York: John Wiley & Sons; 1986.

4. Gerothanassis IP, Troganis A, Exarchou V, Barbarossou K. Nuclear magnetic resonance (NMR) spectroscopy: Basic principles and phenomena, and their applications to chemistry , biology and medicine. Chemistry Education: Research and Practice in Europe 2002;3:229-52.

5. Born M, Oppenheimer RJ. Zur quantentheorie der molekeln. Annalen Der Physik 1927;389:457-84.

6. Leach AR. Molecular mdelling: Principles and applications. In: Molecular mdelling: Principles and applications. 2nd Edition ed. Person Education Limited; 2001.

7. van der Spoel D, Lindahl E, Hess B, van Buuren AR, Apol E, Meulenhoff PJ, Tielemann DP, Sijbers ALTM, Feenstra KA, Van Drunen R, et al. Gromacs user manual, version 3.3. 2005.

8. Bertsimas D, Tsitsiklis J. Simulated annealing. Statistical Science 1993;8:10-5.

9. Kirkpatrick S, Gelatt CD, Vecchi MP. Optimisation by simulated annealing. Science 1983;220:671-80.

10. Hockney RW. Thr potential calculation and some applications. Methods in Computational Physics 1970;9:136-211.

11. Verlet L. Computer 'experiments' on clasical fluids. I. thermodynamical properties of lennard-jones molecules. Physical Review 1967;159:98-103.

12. Tuckerman M, Berne BJ, Martyna GJ. Reversible multiple time scale molecular dynamics. Journal of Chemical Physics 1992;97:1990-2001.

13. Sugita Y, Kitao A, Okamoto Y. Multidimensional replica-exchange method for free-energy calculations. Journal of Chemical Physics 2000;113:6042-51.

14. Swedesen RH, Wang JS. Replica monte carlo simulation of spin glasses. Physical Review Letters 1986;57:2607.

15. Hukushima K, Nemoto K. Exchange monte carlo method and applicationto spin glass simulations. Journal of the Physical Society of Japan 1996;65:1604-8.

16. Tesi MC, Rensburg EJJ, Orlandini E, Whittington SG. Monte Carlo study of the interacting self-avoiding walk model in three dimensions. Journal of Statistical Physics 1996;82:155-82.

17. Kumar S, Rosenberg JM, Bouzida D, Swendsen RH, Kollman PA. THE weighted histogram analysis method for free-energy calculations on biomolecules. I. the method. Journal of Computational Chemistry 1992;13:1011-21.

18. Chodera JD, Swope WC, Pitera JW, Seok C, Dill AK. Use of the weighted histogram analysis method for the analysis of simulated and parallel temperaing simulation. Journal of Chemical Theory and Computation 2007;3:26-41.

19. Leech J, Prins JF, Hermans J. SMD: Visual steering of molecular dynamics for protein design. Computational Science & Engineering, IEEE 1996;3:38-45.

20. Izrailev S, Stepaniants S, Isralewitz B, Kosztin D, Lu H, Molnar F, Wriggers W, Schulten K. Steered molecular dynamics. Springer-Verlag: Berlin, 1998;4.

21. Isralewitz B, Gao M, Schulten K. Steered molecular dynamics and mechanical functions of proteins. Current Opinion in Structural Biology 2001;11:224-30.

22. Lemkul JA, Bevan DR. Assessing the stability of Alzheimer's amyloid protofibrils using molecular dynamics. The Journal of Physical Chemistry B 2010;114:1652-60.

23. Yang LJ, Zou J, Xie HZ, Li L, Wei YQ, Yang SY. Steered molecular dynamics simulations reveal the likelier dissociation pathway of imatinib from its targeting kinases c-kit and abl. PLoS One 2009;4:e8470.

24. Jarzynski C. Nonequilibrium equality for free energy differences. Physical Review Letters 1997;78:2690-3.

25. McQuarries DA. Statistical mechanics. Sausalito, California: University Science Books; 2000.

26. Brooks CL, Karplus M, Pettitt BM. Proteins: A theoretical perspective of dynamics, structure, and thermodynamics. New York: Wiley-Interscience; 1988.

27. McCammon JA, Harvey SC. Dynamics of proteins and nucleic acids. Cambridge, U.K.: Cambridge University Press; 1987.

28. William DC, Moebs. A monte carlo simulation of chemical reactions. Mathematical Biosciences 1974;22:113-20.

29. Torrie GM, Valleau JP. Nonphysical sampling distributions in monte carlo free-energy estimation: Umbrella sampling. Journal of Computational Physics 1977;23:187-99.

30. van Gunsteren WF, Berendsen HJC. Computer simulations of molecular dynamics: Methodology, applications, and perspectives in chemistry Angewandte Chemie International Edition in English 1990;29:992-1023.

Chapter 3

Structure and characterization of the physicochemical properties of tyrocidine peptides based on NMR spectroscopy and molecular dynamics

3.1 Introduction

The activity of antimicrobial peptides is determined by their three-dimensional structures and physicochemical properties.[1-5] Studies involving Gramicidin S, a cyclic decapeptide similar to the tyrocidine peptides have shown that physicochemical properties such as size, amphipathicity, hydrophobicity, conformation and charge distribution play crucial roles in regulating its activity.[6-9] Some of these physicochemical properties such as charge distribution and amphipathicity are determined by the three-dimensional structure of the peptide. Self-aggregation, another important property that influences the mechanism of action of antimicrobial peptides [4, 5, 10-13] depends on a number of factors such as hydrophobicity, amphipathicity, conformation and the general topology of the peptide.[9, 13-15] Various studies have also pointed out that linear antimicrobial peptides are unstructured in water.[16, 17] They are, however, known to adopt certain three dimensional

structures upon interaction with the membrane.[18, 19] Depending on the mechanism of action, peptides may aggregate into higher-order structures inside the membrane leading to the destruction of the cell.[19-21] In order to understand the mechanism of action of cyclic antibiotic peptides it is, therefore, crucial to study their structures before, upon and after interaction with biological membranes. This chapter focuses on elucidating the structures of major tyrocidine peptides in water and decane membrane mimetic environment. The physicochemical properties of the resultant structures are also discussed in relation to their influence on the mechanism of action of the peptides.

3.2 Methods

3.2.1 NMR Experiments

3.2.1.1 Sample preparation

The tyrocidine samples were a generous gift from Prof Marina Rauthenbach, University of Stellenbosch. 1-2 mg of the peptide was dissolved in 0.5 ml of 10:1 (v/v) H_2O:D_2O solution the pH was adjusted to 4 by adding DCl. Trimethylsilylpropionate (TSP) was used as internal chemical shift reference.

^{1}H NMR Experiments

^{1}H NMR experiments were performed on a Bruker Avance 400 MHz (Department of Chemistry, University of Cape Town) and an Avance II 500 MHz (Department of Chemistry, University of Debrecen). The two dimensional NMR spectra of the peptide in water were collected in the phase sensitive mode, TOCSY (mixing time, 60 ms),[22] NOESY (mixing time, 100ms)[23] and ROESY (mixing time, 150ms)[24] using the WATERGATE sequence to suppress the water resonance.[25] Spectral assignments were

based on the method of Wüthrich.[26] Inter-proton distances, from the 2D nOe cross-peak intensities, were estimated by the isolated spin pair approximation (ISPA):[27]

$$\boldsymbol{r}_{ij} = \boldsymbol{r}_{ref}\,(\boldsymbol{a}_{ref}/\boldsymbol{a}_{ij})^{1/6} \qquad (3.1)$$

Where $\boldsymbol{r}_{ij}$ is the inter-proton distances to be estimated and $\boldsymbol{a}_{ij}$ is the corresponding 2D nOe cross-peak intensity.

3.2.2 Simulated Annealing Conformational Search

The starting configuration of the peptide was generated using homology modeling. The structure of gramicidin S was used as the template. An initial conformational search was performed using molecular dynamics in vacuum at 600K for 100 ns using the GROMACS molecular dynamics package.[28] NMR derived distance restraints shown in appendix 1 were applied with a force constant of 1000 kJ mol-1 nm-2 during the simulated annealing conformational search. The OPLS force field was used in the calculations.[29] A time step of 2 fs was used. The non-bonded interactions were treated with a switch function operating at 12 Å. Structures were saved every 1000 ps. All the saved structures were subjected to simulated annealing for 1 ns. The structure that had the lowest energy after annealing was subjected to molecular dynamics in water.

3.2.3 Molecular Dynamics in water

The structure with minimum energy from simulated annealing was subjected to molecular dynamics for 100 ns. In all cases, NMR derived distance restraints were continuously applied with a force constant of 1000 $kJ.mol^{-1}.nm^{-2}$. The peptide starting conformation was placed in a cubic box with dimensions 33 × 36 × 41 Å and a volume

of about 49 nm^{-3}. The box was then solvated with water. The Simple Point Charge (SPC) based model was used to represent the water atoms.[30] No counterions were added to balance the charge of the system. The system was subjected to steepest descent energy minimization using a force tolerance of 100 $kJ.mol^{-1}.nm^{-1}$ to remove high energy contacts. An initial step size of 0.01 was used. The water molecules were then equilibrated by a short molecular dynamics simulation at 300 K (1 ns duration, 2 fs integration timestep) with the heavy atoms of the peptide position restrained. The density of water approximately replicated the experimental value of 1000 $g.l^{-1}$. Molecular dynamics was further run for 1 ns to equilibrate the system energies.

One hundred nanosecond molecular dynamics simulations were conducted for the peptide with structures collected every 100 ps. The integration time step was 2 fs and the neighbourhood list was updated every 10 fs. Lennard-Jones and Coulombic non bonded interaction terms were treated with a cut-off scheme operating at 15 Å. Protein and solvent were coupled independently to an external temperature bath using a time constant of 0.1 ps according to the Berendsen method.[31] The LINCS algorithm was used to constrain all covalent bonds.[32]

3.2.4 Molecular Dynamics in Decane

Molecular dynamics simulations of the peptides in a decane solvent box were conducted using the GROMACS molecular dynamics package,[28] and the OPLS forcefield.[29] This study sought to determine the structure of tyrocidine peptides in hydrophobic membrane environment. Decane was chosen because its properties are comparable to those of the hydrophobic middle section of lipid bilayers.[33] Using decane aided in reducing the size of

the system at the same time retaining the properties of the membrane environment under study. The methyl and methylene groups of the decane solvent molecules were treated as unified atoms.[34] The decane solvent box was constructed in a stepwise fashion. A one decane molecule solvent box was initially generated. This was then expanded by a factor of 10 and filled with decane molecules. The solvent box was subjected to NPT molecular dynamics, to make a liquid out of it. The simulation was conducted at 300K for 10 ns duration with a timestep of 2 fs. All bonds were constrained using the LINCS algorithm.[32] The density of decane approximately replicated the experimental value of 700g/l. The peptide was then solvated in the resultant box of size 5.5 × 5.5 × 5.5 nm. The system was subsequently subjected to l-bfgs energy minimisation[35] to remove high energy contacts. This was followed by a short molecular dynamics simulation at 300K for 1 ns using a 2 fs time step. The peptide position was restrained to allow the decane molecules to soak the peptide. Unrestrained molecular dynamics simulations of 1 ns were conducted at 300K to allow the system to equilibrate. The integration time step was 2 fs and the neighbourhood list was updated every 10 fs. Non bonded interactions (Lennard-Jones and Coulombic terms) were treated with a cut-off function operating at 15 Å. Protein and solvent were coupled separately to an external temperature bath using a time constant of 0.1 ps according to the Berendsen method.[31] The molecular dynamics simulation for the system was extended for a further 100 ns. The same parameters described in the equilibration calculations were used. Structures were collected every 100 ps.

3.3 Analysis

The DSSP program[36] was used to calculate the secondary structure elements of the peptides. However, the DSSP program does not recognize the cyclization bond between the terminal residues in cyclic peptides, hence the two residues were neglected during secondary structure calculation and are always reported as coils. The peptides were considered to have formed a β-structure if they had a β-sheet, β-bridge or both structural elements. They were considered to be non-structured if they only had bends, turns and coils.

Cluster analysis[37] was performed to determine the similarities of structures obtained from molecular dynamics. Least square rotational and translational fit on the backbone atoms was done on each structure that was saved in the trajectory. Structures were regarded as similar if their atom-positional root-mean-square difference (RMSD) were ≤ 0.10 nm. Backbone atoms (N, Cα, C) were used in determining the RMSD. The structure with the largest number of neighbors and all its neighbors were regarded as a cluster and eliminated from the pool of clusters. The process was repeated until all the structures were put in their respective clusters.

3.4 Results and Discussion

3.4.1 Tyrocidine C

3.4.1.1 NMR

The ^{1}H chemical shifts are shown in Table 3.1. The ^{1}H chemical shifts measurements are novel and are a major contribution of this work. The correlations between chemical shifts of Hα protons, and the secondary structure of peptides and proteins identified in earlier studies[38-40] were utilized to extract the structural information of tyrocidine C. Helical alpha protons and amide protons have chemical shifts that are consistently less than their respective random coil values by about 0.3 ppm. β-sheets show chemical shift values that are consistently greater than their random coil values by about 0.3 ppm.[38, 39, 41] The involvement of amide protons in hydrogen bonding affects their chemical shifts, thereby limiting their use as a qualitative indicator for the presence of helix or β-structures.[42] The ^{1}H chemical shifts can also be affected by aromatic ring currents[43] and sequence effects.[44]

Figure 3.1 shows a comparison of the Hα and H^{N} chemical shifts to their random coil values for tyrocidine C in water.[38, 39, 42, 45] The backbone H^{N} chemical shifts of all residues were greater than their random coil values by more than 0.3 except for Trp^{3} and Val^{8}, which were less by 0.2 and 0.1 ppm respectively. Residue Asn^{5} showed the largest deviation of 0.9 ppm. The Hα proton chemical shifts were also larger than their random coil values by between 0.1 - 1.4 ppm as shown in Figure 3.1. The Hα chemical shifts of residues Phe^{1}, Pro^{2} and Trp^{3} were different from their random coil values by less than 0.3 ppm. The majority of the chemical shifts suggest the presence of β-sheets. The opposite

shift of H^N values for Trp^3 and Val^8 can be attributed to the ring current effects of neighboring aromatic residues. It could also be due to their involvement in hydrogen bonding.

Table 3.1: ^{1}H assignments and chemical shifts (ppm) of TyrC in 50% (*v/v*) $D_2O/CNCD_3$ at 4.8 ppm and a temperature of 305K

Residue	H^N	Hα	Hββ'	Hγγ'	Hδδ'	Other	Aromatics
Phe[1]	9.089	4.803	4.674; 3.336				7.560[&](2,6);7.647 (4); 7.671[&](3,5)
Pro[2]	--	4.545	0.705; 1.380	1.758	2.450; 3.401		
Trp[3]	7.857	4.850	2.350; 2.796			10.224 (1-NH)	7.42;7.51(5,6); 7.60(2);7.75(7); 7.89 (4)
Trp[4]	8.555	6.135	3.494; 3.624			10.105 (1-NH)	7.29;7.47(5,6); 7.405(2);7.70 (7); 8.00 (4)
Asn[5]	9.676	5.290	3.401; 3.671			8.045; 7.190 $CONH_2$	
Gln[6]	8.913	4.803	4.386	2.145		7.520; 7.040 $CONH_2$	
Tyr[7]	8.860	4.950	3.377; 3.547				7.14(3,5);7.44(2,6)
Val[8]	8.310	4.920	2.550	1.433; 1.442			
Orn[9]	8.772	5.724	2.321*; 2.239*	2.104*	3.272		
Leu[10]	8.602	4.896	1.720[#]; 1.840[#]	1.670[#]	1.345; 1.368		

*, [#], [&] assignments mutually interchangeable

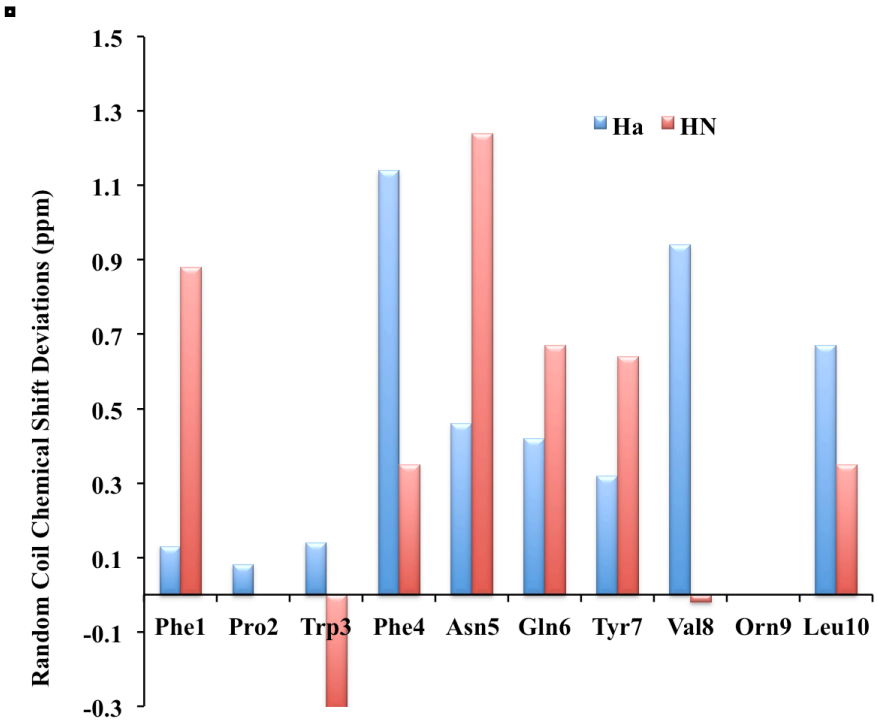

Figure 3.1: Backbone H^N and Hα chemical shift deviations from random coil values for TyrC in water. Random coil chemical shifts were obtained from[53]

The $^3J_{HNH\alpha}$ coupling constants that are useful for structure prediction are the ones less than 5 and greater than 8.[46] This is because between 5 and 8 the ^3J coupling constants are unable to distinguish the preferred dihedral angle, and can predict up to four dihedral angles.[26] A $^3J_{HNH\alpha}$ coupling constant less than 5 Hz is indicative of an α -helical conformation, whereas a $^3J_{HNH\alpha}$ greater than 8 shows the presence of a β-sheet structure.[47] Table 3.1 shows that all the experimental $^3J_{HNH\alpha}$ coupling constants were greater than 8 except for Asn[5] which was 7.9. Thus, the NMR coupling constants indicate the presence of β-strands.[40, 48] Molecular dynamics (MD) was also used to calculate the theoretical $^3J_{HNH\alpha}$ constants in water. They were comparable to those obtained from NMR. ^3J coupling constants of Phe[1], Gln[6] and Orn[9] from MD were less than 8 Hz, and the coupling constants of these three residues could not be determined experimentally as the

line widths of the peaks were comparable to the coupling constant. Table 3.2 shows that phi angles calculated from the MD simulation were in good agreement with the values determined from NMR.

Table 3.2: $^{1}H–^{1}H$ coupling constants (Hz), the experimental φ angle derived from the Karplus equation [46] and the corresponding calculated φ angles from MD.

Residue	NMR $^{3}J_{HNH\alpha}$ coupling constant	NMR φ dihedral angle (°)	MD $^{3}J_{HNH\alpha}$ coupling constant	MD φ dihedral angle (°)
Phe[1]	-	-	5.4	80 ± 15
Pro[2]	-	-	-	-
Trp[3]	8.6	-142	8.7	-126 ± 23
Trp[4]	9.5	-151	8.4	-144 ± 9
Asn[5]	7.9	-146	8.5	-144 ± 9
Gln[6]	-	-	6.0	74 ± 8
Tyr[7]	9.7	-120	8.6	-142 ± 16
Val[8]	9.0	-140	8.9	-104 ± 16
Orn[9]	-	-	7.7	-88 ± 10
Leu[10]	9.0	-140	9.5	-129 ± 10

3.4.1.2 Simulated Annealing Conformational Search

The conformational search of the peptide was performed at 600 K using molecular dynamics. This process generated 100 structures and each structure was subsequently subjected to simulated annealing for 1 ns. The structure with lowest energy after simulated annealing was subjected to molecular dynamics in decane and water.

3.4.1.3 Molecular Dynamics in water and decane

Cluster analysis, based on the backbone atoms of the peptide, gave only one cluster for both the water and decane simulations. There was very little variation of the secondary

structure of TyrC in water and decane as shown in Figure 3.2. The secondary structure plots show that TyrC favors the formation of β-structures in both water and decane.

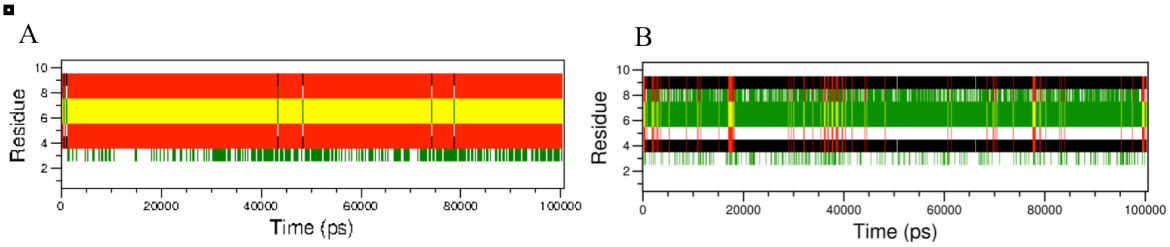

Figure 3.2: Secondary structure plots of TyrC in water A and decane B. The colours associated with the secondary structural elements are red (β-sheets), yellow (turn), green (bend), black (β-bridge) and white (coil).

The Ramachandran plots of individual residues, shown in Figure 3.3 indicated the lack of flexibility of TyrC during the simulations. The rigidity of the backbone conformation can be attributed to the fact that TyrC is cyclized, and the rotation of amide bonds is restricted. However, it was noted that the side chains were more flexible. The Ramachandran plot of TyrC shows that six of its ten residues were in the β-region. These residues are Trp[3], Trp[4], Asn[5], Val[8], Orn[9], and Leu[10]. Phe[1] was located in the unwanted or type II region of the Ramachandran plot for the entire duration of the simulation. The three remaining residues Pro[2], Gln[6] and Tyr[7] were located between the β-region and the α-region. The Ramachandran plot of TyrC in decane was remarkably similar to the one found in water except that one residue, Gln[6] was located in a different region. In decane, Gln[6] was located in the type II or unwanted region. Glycine or residues that constitute turn regions in peptides are often found in this region.[67] D-amino acid segments found in both type II' and type I' turns can also be found in this region.[68]

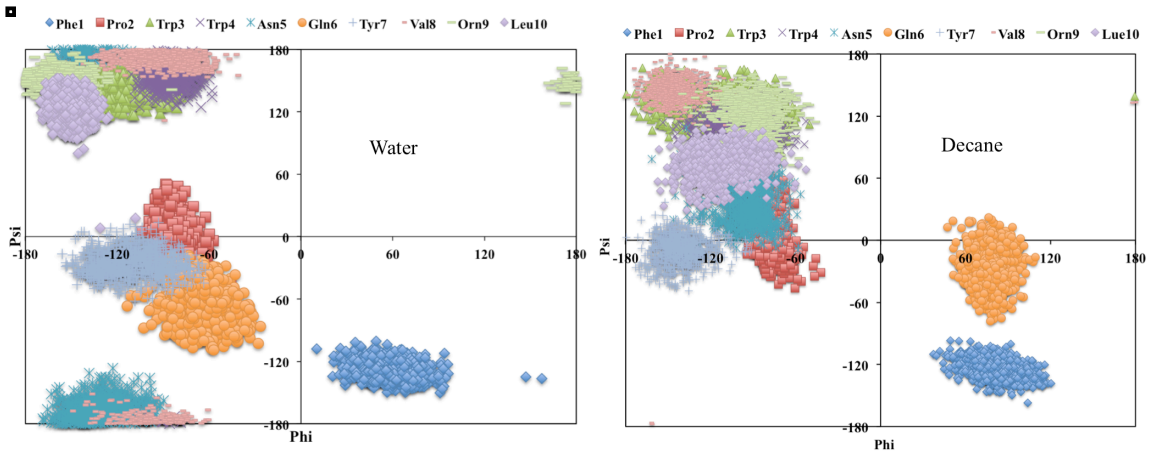

Figure 3.3: Ramachandran plots of the backbone dihedral angles, φ and ψ of the simulations of TyrC in water and decane.

Figures 3.4A and 3.4B show the root conformer (the structure with minimum energy in the predominant cluster) of TyrC. Tyrocidine C is weakly amphipathic. This is because hydrophobic and hydrophilic residues in structures obtained from both water and decane simulations are not completely separated. However, TyrC showed consistent and important intra-molecular hydrogen bonding networks during the simulations. There were fewer intra-molecular hydrogen bonds formed in water than in decane. In general, about half the number of intramolecular hydrogen bonds were made in water compared to decane. The most frequent hydrogen bonds were between Trp^{3}-O-NH-Leu^{10}, Asn^{5}-O-HN-Val^{8} and Val^{8}-O-HN-Asn^{5} in water. The frequency of these hydrogen bonds was 97.1%, 91.9 % and 98.7 % respectively. Four intra-molecular hydrogen bonds were consistently identified for more than half of the simulation time in decane. These were between Trp^{3}-O-NH-Leu10, Asn^{5}-OD1- NE1HE1-Trp^{3}, Asn^{5}-O-NH-Tyr^{7} and Val^{8}-O-NH-Asn^{5} and occurred for 90.5 %, 60.2 %, 62.2 % and 92.5 % of the calculation time respectively. These findings suggest that, in water, hydrophilic groups of the peptide are exposed to bulk water to form hydrogen bonds with water molecules, and in decane the

hydrophilic groups of the peptide tend to combine with each other. In both systems, the resultant conformations showed anti-parallel β-sheet elements between residues Trp^3-Asn^5 and Val^8-Leu^{10} as shown in Figures 3.4C and 3.4D.

The residues Leu^{10}, Phe^1 and Pro^2 fulfilled the requirements of a Type II' β-turn (φ_{i+1} =82°, ψ_{i+1} = -125°, φ_{i+2} = -71, ψ_{i+2} = -10°) in water. [49, 50] The average dihedral angles of Gln^6 (φ = 73°, ψ = -72°) pointed to the presence of a γ-turn for the Asn^5- Tyr^7 sequence. This was stabilized by a hydrogen bond between Asn^5 and Tyr^7 (O_i – HN_{i+2}) identified for a significant part of the simulation.[49, 50] In decane, tyrocidine C formed a type II' turn and a γ-turn. The type II' turn was between residues Leu^{10}, Phe^1 and Pro^2 and the γ-turn was comprised of Asn^5, Gln^6 and Tyr^7. This was confirmed by the angles φ_{i+1} =82°, ψ_{i+1} = -125°, φ_{i+2} = -71, ψ_{i+2} = -10° between Phe^1 and Pro^2 respectively as well as φ_{i+1} =78°, ψ_{i+1} = -25° for Gln^6.

A low, pairwise, RMSD of 0.90 was obtained upon superimposition of the backbone atoms of the decane and water root conformers (Figure 3.5). The backbones of the conformers exhibited highly similar conformations.

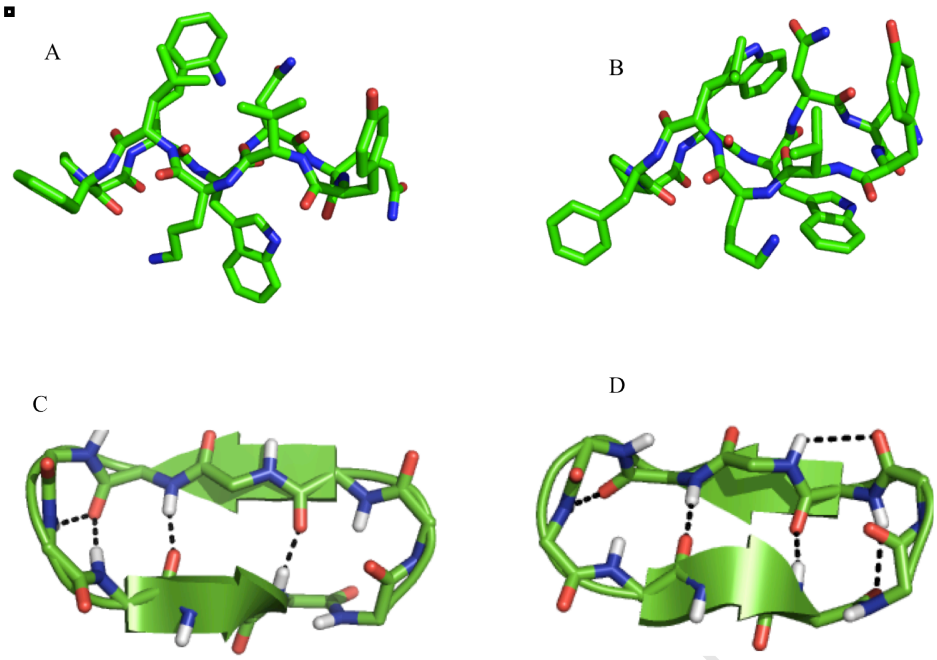

Figure 3.4: Root conformations of TyrC. A is the root conformation in water and B is the root conformation in decane. Only heavy atoms are shown. C and D show the secondary structure elements of TyrC in water and decane respectively. The most frequent hydrogen bonds are shown as dotted lines.

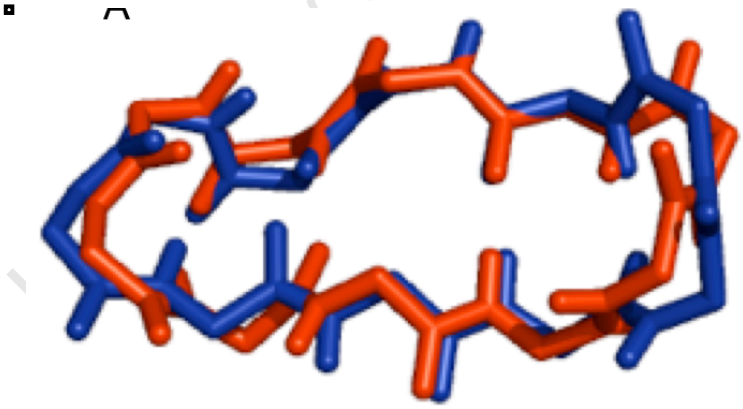

Figure 3.5: Superimposed backbone structures of root conformers of TyrC. The structure in decane is coloured in blue, and the structure in water is coloured in red**.**

3.4.2 Tyrocidine A

3.4.2.1 NMR

Table 3.3 below shows the ^{1}H chemical shifts of TyrA in water.

Table 3.3. 1H assignments and chemical shifts (ppm) of TyrA in 50% (*v/v*) $D_2O/CNCD_3$ at 4.8 ppm and a temperature of 305K

Residue	H^N	Hα	Hββ'	Hγγ'	Hδδ'	Other	Aromatics
Phe[1]	9.316	5.054	3.670; 3.630				
Pro[2]	--	4.877	1.073; 1.756	2.086	2.850; 3.960		
Phe[3]	8.137	5.116	3.080; 3.126				
Phe[4]	9.056	6.349	3.673; 3.820				
Asn[5]	9.800	5.479	3.696; 3.924			8.300; 7.434 $CONH_2$	
Gln[6]	9.280	4.656	2.370*; 2.410*	2.581*		7.754; 7.248 $CONH_2$	
Tyr[7]	9.064	5.211	3.516; 3.790				7.430 (3,5); 7.722 (2,6)
Val[8]	8.517	5.084	2.794	1.685			
Orn[9]	8.772	5.724	2.390[#]; 2.445[#]	2.617[#]	3.550		
Leu[10]	8.865	5.211	2.020[&];	2.390[&]	1.655		

*, [#], [&] assignments mutually interchangeable

Figure 3.6 shows a comparison of the Hα and H^N chemical shifts with their random coil values for TyrA in water.[38, 39, 42, 45] All of the backbone amide proton chemical shifts were greater than their random coil values by more than 0.3 except for the amide proton chemical shifts of Phe[3] and Val[8]. The random coil chemical shift deviations of Phe[3] and Val[8] were -0.1 ppm and 0.2 ppm respectively. Phe[4] showed the largest deviation of 1.4

ppm. All the Hα proton chemical shifts were close to 0.3 or greater as shown in Figure 3.6. Phe[4] had the largest deviation of 1.7, and Gln[6] had the smallest deviation, which was close to 0.3. The majority of the chemical shifts suggest the presence of β-sheets. The random coil chemical shift deviation of H^N value for Phe[3] can be attributed to the ring current effects of neighboring aromatic phenylalanine residues. It could also be due to its involvement in hydrogen bonding.

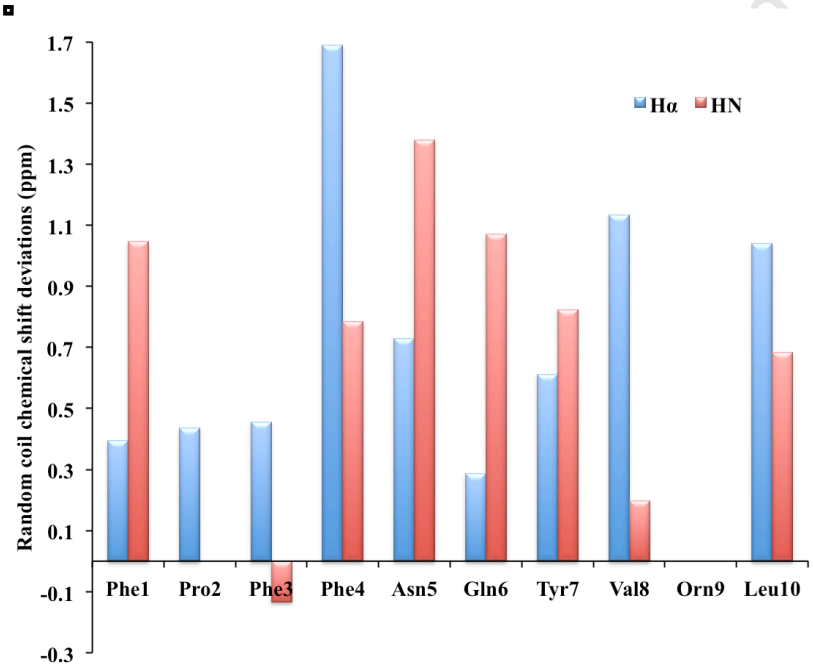

Figure 3.6: Backbone H^N and Hα chemical shift deviations from random coil values for TyrA in water. Random coil chemical shifts were obtained from [53].

The MD simulation results were used to calculate the $^3J_{HNH\alpha}$ coupling constants of TyrA in water, and compared to those determined from NMR (Table 3.4). The $^3J_{HNH\alpha}$ coupling constants from both MD and NMR varied between 4.0 Hz, and 9.9 Hz. Six residues had ^3J coupling constants that were greater than 8 Hz from NMR compared to 5 from MD calculations. NMR showed that the coupling constants of Phe[1], Asn[5] and Gln[6] were

below 8 Hz, whereas, Phe[1], Phe[3], Phe[4] and Gln[6] had coupling constants less than 8 for the MD simulation. The $^{3}J_{HNH\alpha}$ coupling constants pointed to the presence of β-sheets for TyrA in water. The $^{3}J_{HNH\alpha}$ constants from NMR and MD were also used to calculate the phi torsion angles, and were found to be in reasonable agreement.

Table 3.4. $^{1}H–^{1}H$ coupling constants (Hz), the experimental φ angle derived from the Karplus equation [46] and the corresponding calculated φ angles from MD.

Residue	NMR $^{3}J_{HNH\alpha}$ coupling constant	NMR φ dihedral angle (°)	MD $^{3}J_{HNH\alpha}$ coupling constant	MD φ dihedral angle (°)
Phe[1]	4.0	-106	5.7	-108 ± 9
Pro[2]	--	-	-	
Phe[3]	8.8	-141	7.6	-144 ± 18
Phe[4]	9.8	--	7.2	156 ± 40
Asn[5]	7.5	-154	9.2	-150 ± 60
Gln[6]	4.0	-106	4.9	-27 ± 12
Tyr[7]	9.9	--	9.2	-33 ± 17
Val[8]	9.0	-140	8.8	-147 ± 17
Orn[9]	9.5	-130	9.1	144 ± 9
Leu[10]	9.2	-135	8.9	68 ± 18

3.4.2.2 Simulated Annealing Conformational Search

The simulated annealing conformational search generated an ensemble of 100 structures. The structure that had the lowest energy after annealing was subjected to molecular dynamics in decane and water molecular dynamics simulations.

3.4.2.3 Molecular Dynamics in Water and Decane

The structures that were obtained during molecular dynamics simulations in both water and decane were clustered, and each gave a single cluster. The rigidity of the structures of TyrA in water and decane can be seen in the variation of the secondary structure elements shown in Figure 3.7. TyrA favors the formation of a β-structure in both water and decane as indicated by the secondary structure elements. This was also confirmed by the Ramachandran plot where a significant number of the residues were seen to be resident in the β-region.

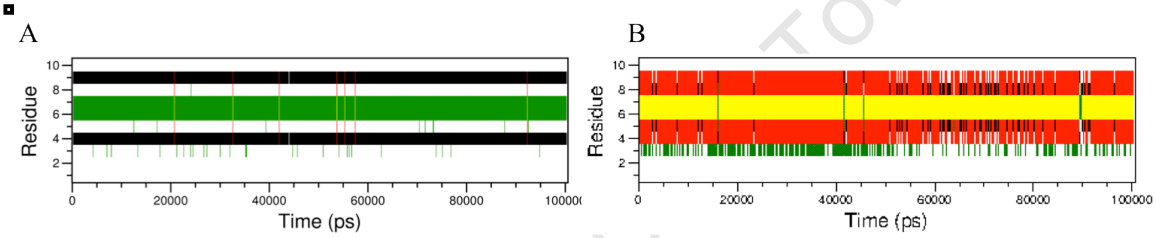

Figure 3.7: Secondary structure plots of TyrA in water A and decane B. The colours associated with the secondary structural elements are red (β-sheets), yellow (turn), green (bend), black (β-bridge) and white (coil).

The Ramachandran plot for TyrA in water, shown in Figure 3.8, indicated that its residues were resident in three different regions, β-region, α-region and the type II region or unwanted region. Six residues Phe^{3}, Phe^{4}, Asn^{5}, Val^{8}, Orn^{9} and Leu^{10} were resident in the β-region. Three residues Pro^{2}, Gln^{6} and Tyr^{7} were located in the α-region whereas only one residue Phe^{1} was found in the disallowed region of the Ramachandran plot. The Ramachandran plot of TyrA in decane shown in Figure 3.8 is similar to the one obtained in the water simulation. The only difference is that Gln^{6} occupies the unwanted region instead of the α-region. The residues that were not found in the β-region region of the Ramachandran plots were those that occupied the turn regions of the peptide. This was

consistent in both environments. Glycine or residues that constitute turn regions in peptides are often found in this region.[67] D-amino acid segments found in both type II' and type I' turns can also be found in this region.[68]

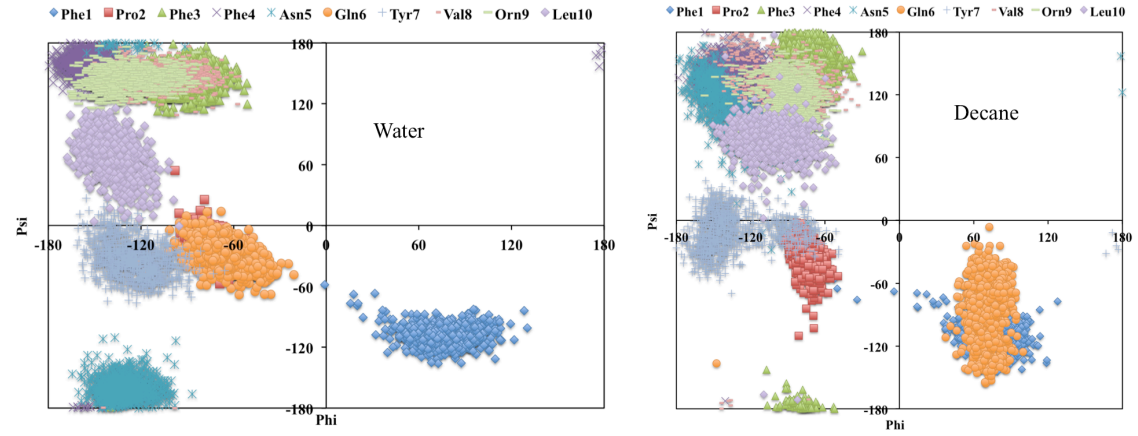

Figure 3.8: Ramachandran plots of the backbone dihedral angles, φ and ψ of the simulations of TyrA in water and decane.

Figure 3.9 shows the root conformers of TyrA in water and decane respectively. The root conformers in both water and decane, Figure 3.9A and Figure 3.9B indicate that hydrophilic and hydrophobic residues were found on both sides of the peptide. The lack of separation between hydrophilic and hydrophobic residues meant that TyrA is weakly amphipathic. The structure obtained in decane formed more intramolecular hydrogen bonds compared to the one in water indicated by Figures 3.9C and 3.9D. The root conformer of TyrA showed 2 backbone-backbone hydrogen bonds in water, and 3 backbone-backbone hydrogen bonds in decane. This was in contrast to what had been reported before[51, 52] where TyrA showed four backbone-backbone hydrogen bonds. The bonds between Phe^{3}-O-NH-Leu^{10} and Asn^{5}-NH-O-Val^{8} were found in both structures but the additional bond between Asn^{5}-O-NH-Val^{8} occurred only in TyrA in decane. The structures obtained both water and decane showed β-sheet conformation between residues

Trp[3]-Asn[5] and Val[8]-Leu[10].

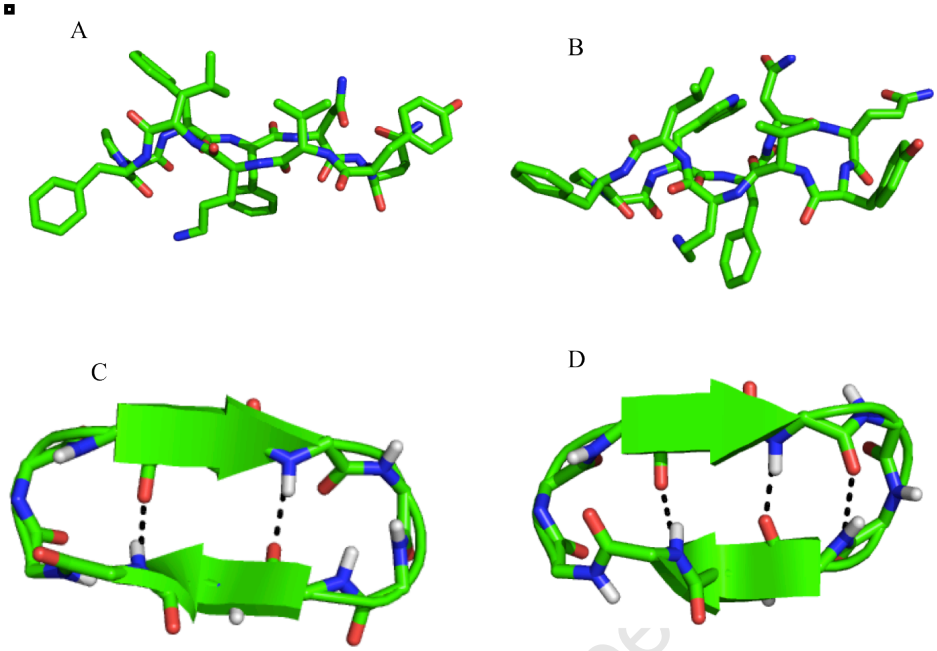

Figure 3.9: Root conformations of TyrA. A is the root conformation in water and B is the root conformation in decane. Only heavy atoms are shown. C and D show the secondary structure elements of TyrA in water and decane respectively. The hydrogen bonds on the root conformations are shown as dotted lines.

TyrA exhibited a type I turn and a type II' turn in water. The type II' turn was made up of residues Leu[10], Phe[1] and Pro[2] as indicated by the torsion angles (φ_{i+1} =74°, ψ_{i+1} = -108°, φ_{i+2} = -77, ψ_{i+2} = -20°) where i+1 and i+2 are Phe[1] and Pro[2] residues respectively. Residues Asn[5], Gln[6] and Tyr[7] fulfilled the criteria of a type I turn for tyrocidine A in water. The torsional angles between the Gln[6] and Tyr[7] were (φ_{i+1} =-65°, ψ_{i+1} = -27°, φ_{i+2} = -124, ψ_{i+2} = -33°). In decane, TyrA exhibited two type II' turns. The dihedral angles of Phe[1] and Pro[2] (φ_{i+1} =73°, ψ_{i+1} = -110°, φ_{i+2} = -73, ψ_{i+2} = -39°) as well as the angles of Gln[6] and Tyr[7] (φ_{i+1} =71°, ψ_{i+1} = -81°, φ_{i+2} = -131, ψ_{i+2} = -10°) fulfilled the criteria for type II' turns.

The backbone structures of the root conformers from the simulation in decane and water were superimposed to determine the similarity of the two structures in the two environments. This showed that the structures were remarkably similar.

3.4.3 Tyrocidine B

3.4.3.1 NMR

Table 3.5 shows the ^{1}H chemical shifts of TyrB determined in 50% (*v/v*) $D_2O/CNCD_3$ at 4.8 ppm and a temperature of 298 K.

Table 3.5: 1H assignments and chemical shifts (ppm) of TyrB in 50% (*v/v*) $D_2O/CNCD_3$ at 4.8 ppm and a temperature of 298 K

Residue	H^N	Hα	Hββ'	Hγγ'	Hδδ'	Other	Aromatics
Phe[1]	8.572	4.235	2.868				7.11 (2,6); 7.08-7.20 (3,4,5)
Pro[2]	--	4.075	0.187; 0.890	1.250; 1.300	1.970; 2.980		
Trp[3]	7.414	4.450	2.417; 2.572			9.730 (1-NH)	6.95;7.03(5,6);7.01(2); 7.27 (7); 7.54 (4)
Phe[4]	8.295	5.625	2.764; 3.023				7.18 (2,6); 7.08-7.20 (3,4,5)
Asn[5]	9.080	4.723	2.942; 3.178			7.578; 6.705 $CONH_2$	
Gln[6]	8.517	4.191	3.910; 1.809	1.648; 1.803		7.036; 6.532 $CONH_2$	
Tyr[7]	8.331	4.464	2.890; 3.067				6.68 (3,5); 6.97 (2,6)
Val[8]	7.783	4.353	2.035	0.939			
Orn[9]	8.219	5.218	1.663[&]; 1.700[&]	1.863[&]	2.800		
Leu[10]	8.189	4.464	1.301	1.508	0.939		

[&] assignments mutually interchangeable

The Hα and H^N chemical shifts for TyrB in water were compared with their random coil values[38, 39, 42, 45] as shown in Figure 3.10A. The observed chemical shifts must be greater than their random coil values by 0.3 for a structure to adopt a β-strand. For a peptide to adopt a helical structure, the observed chemical shifts must be less than their random coil values by at least 0.3. The general observation was that for both Hα and H^N, there was no systematic trend followed by the differences between the observed and the random coil chemical shifts. The differences were randomly distributed downfield and upfield. The observed Hα chemical shifts were greater than their random coil values in Phe^1, Phe^4, Val^8 and Leu^{10} and the rest were less than their random coil values. Only Phe^1 and Phe^4 had values greater than 0.3. Of the observed Hα chemical shifts that were lower than their random coil values, only Pro^2 and Trp^3 had values that were less than -0.3. For the observed H^N chemical shifts, only Trp^3 and Leu^{10} experienced up-field shifts, and the rest experienced downfield shifts with respect to their random coil values. Of the amide proton chemical shifts that experienced downfield shifts, only Phe^1, Asn^5 and Val^8 had differences greater than 0.3. These results point out that TyrB is unstructured in water.

The chemical shift index (CSI) method[40] was employed to check if it would give the same conclusion as the random coil chemical shift deviation method. In the CSI method, the Hα chemical shift values are compared to their random chemical shift values. The residue is assigned a value of 1 if the Hα is greater than 1. A value of 0 is assigned to a residue when the observed chemical shift is within the random coil range, and -1 is assigned to the residue if the observed chemical shift is less than the random coil range.[40] The indices are then used to determine the secondary structure of the peptide. A group of

at least four -1's uninterrupted by a 1 indicates a helical structure and a group of at least three 1's uninterrupted by a -1 represent a β-sheet. The other regions that do not fall in either the β-sheet or the helical structure are defined as coils.[40, 53] From the CSI plot shown in Figure 3.10B, tyrocidine B can be said to be unstructured in water.

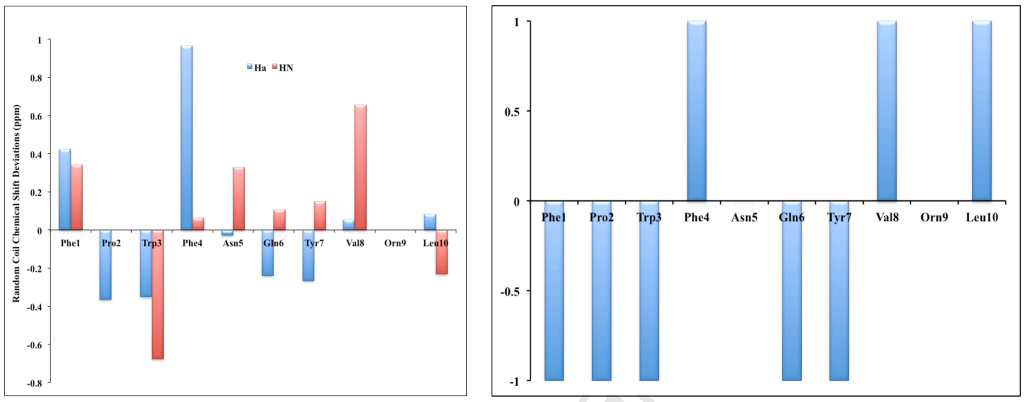

Figure 3.10: Backbone H^N and Hα chemical shift deviations from random coil values for TyrB in water and CSI plot. Random coil chemical shifts were obtained from[53]

The experimental and theoretical $^3J_{HNH\alpha}$ coupling constants and their corresponding phi torsion angles were determined and compared to each other as shown in Table 3.6. Six of the experimental $^3J_{HNH\alpha}$ coupling constants were greater than 8, and these were for Trp^3, Phe^4, Tyr^7, Val^8, Orn^9 and Leu^{10}. Phe^1 and Gln^6 had $^3J_{HNH\alpha}$ coupling constants in the α-helix region. Asn^5 had a coupling constant value of 7.6. Molecular dynamics gave only three $^3J_{HNH\alpha}$ constants that were greater than 8. These were coupling constants of Trp^3, Val^8 and Leu^{10}. Phe^1 and Phe^4 had values below 5, and the rest had $^3J_{HNH\alpha}$ coupling constants between 5 and 8. The experimental and MD $^3J_{HNH\alpha}$ coupling constants of TyrB in water were different. The values from experiment pointed to the presence of β-sheets.

$^{3}J_{HNH\alpha}$ coupling constants obtained from MD were mainly found in the region where they are unable to distinguish the preferred dihedral angle.

Table 3.6. $^{1}H–^{1}H$ coupling constants (Hz), the experimental φ angle derived from the Karplus equation [46] and the corresponding calculated φ angles from MD.

Residue	NMR $^{3}J_{HNH\alpha}$ coupling constant	NMR φ dihedral angle (°)	MD $^{3}J_{HNH\alpha}$ coupling constant	MD φ dihedral angle (°)
Phe[1]	3.7	-109	4.0	-126 ± 17
Pro[2]	--	--		-22 ± 26
Trp[3]	8.6	-142	8.7	140 ± 60
Phe[4]	10.0	--	3.8	-42 ± 54
Asn[5]	7.6	-93	6.2	-52 ± 54
Gln[6]	3.7	-109	7.3	-1 ± 115
Tyr[7]	9.6	-127	5.5	-22 ± 21
Val[8]	8.9	140	8.6	34 ± 137
Orn[9]	9.8br	-	7.9	115 ± 35
Leu[10]	9.0	-140	8.6	28 ± 44

3.4.3.2 Simulated Annealing Conformational Search

The simulated annealing conformational search generated an ensemble of 100 similar structures. Cluster analysis using the backbone atoms and an RMSD cut-off of 0.15 nm yielded one cluster. The root conformer of the cluster was used as the starting structure for molecular dynamics simulations in both water and decane.

3.4.3.3 Molecular Dynamics in Water and Decane

Cluster analysis, based on the backbone atoms of the peptide, gave twenty-five clusters for the simulation in water. The predominant cluster contained 34% of all the structures. The rest of the clusters contained remarkably few structures, and some clusters containing as few as 1 % of all the structures saved during molecular dynamics. The large

number of clusters found in water for TyrB confirmed the NMR results, indicating that the molecule is unstructured in water. This was also confirmed by the manner in which the secondary structure of TyrB varied in water. It lacked well-defined and persistent secondary structure elements (Figure 3.11). However, cluster analysis of the simulation of TyrB in decane retained one cluster. The secondary structure analysis plot indicated that TyrB forms a β-structure in decane.

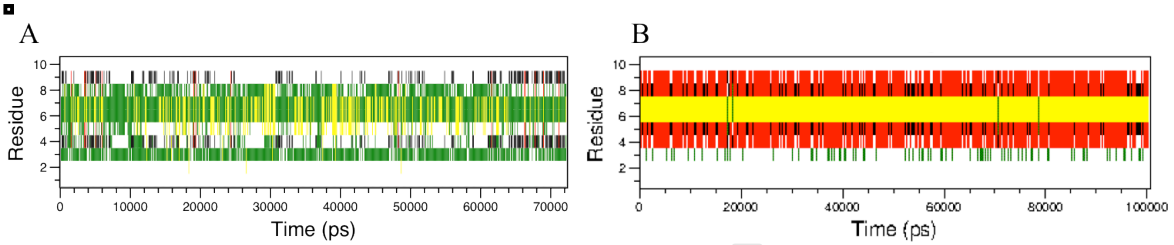

Figure 3.11. Secondary structure plots of TyrB in water A and decane B. The colours associated with the secondary structural elements are red (β-sheets), yellow (turn), green (bend), black (β-bridge) and white (coil).

A Ramachandran plot of individual residues indicated that TyrB was extremely flexible in water. A number of residues resided in more than one region of the plot during the course of the simulation. Tpr^{3}, Gln^{6}, Val^{7}, Orn^{9} and Leu^{10} were found in the β-region. Leu^{10} also spent a considerable amount of time in the right-handed, α-helix region. Gln^{6} was found in all the four regions of the ramachandran plot. Pro^{2} and Asn^{5} spent more than 80% of their time in the right handed α-helix region. Of the five residues, Phe^{1}, Phe^{4}, Asn^{5},Gln^{6} and Tyr^{7} that were found in the disallowed region, only Phe^{1} and Tyr^{7} resided there for more than 90% of the time. Glycine or residues that constitute turn regions in peptides are often found in this region.[67] D-amino acid segments found in both type II' and type I' turns can also be found in this region.[68] This is likely to point to the fact that Phe^{1} and Tyr^{7} are turn residues in TyrB. Only Phe^{4} resided in the left handed α-helix

region for more than 50% of the time. A number of residues were found in different regions of the Ramachandran plot hence the peptide was unstructured in water.

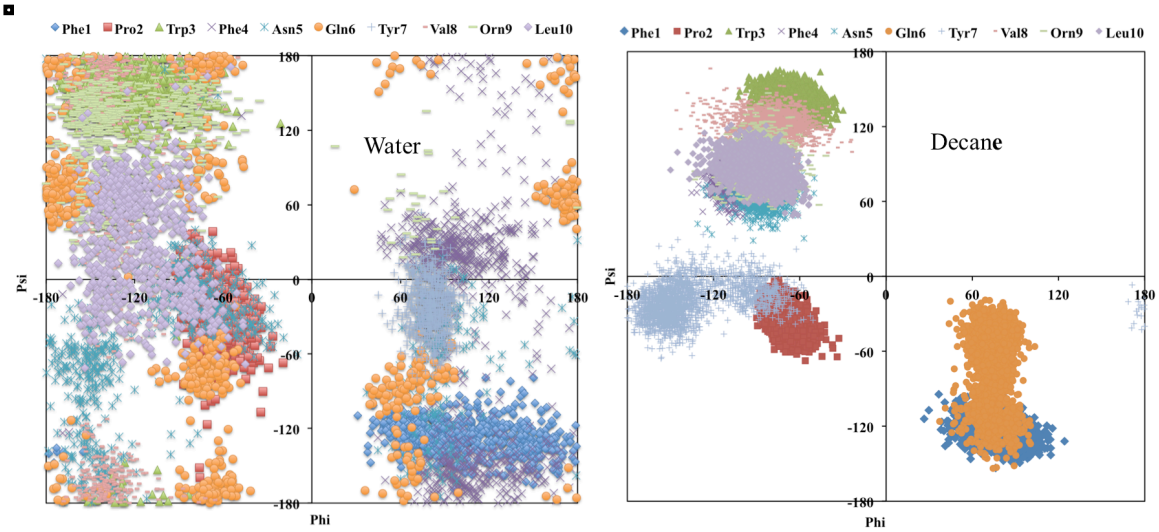

Figure 3.12: Ramachandran plots of the backbone dihedral angles, φ and ψ of the simulations of TyrB in water and decane.

Figure 3.13A and Figure 3.13B show the root conformers of TyrB in water and decane respectively. There was no distinctive separation of hydrophilic and hydrophobic residues in both structures found in water and decane. This means that TyrB is only weakly amphipathic. The root conformer of TyrB in water was unstructured as shown in Figure 3.13C. However, it contained three significant backbone-backbone hydrogen bonds. These were between Asn^5-NH-O-Val^8, Asn^5-O-NH-Val^8 and Asn^5-O-NH-Tyr^7. The structure obtained in decane contained the four backbone-backbone hydrogen bonds reported before.[51, 52] These were between Trp^3-NH-O-Leu^{10}, Trp^3-O-NH-Leu^{10}, Asn^5-NH-O-Val^8 and Asn^5-O-NH-Val^8. There was also a hydrogen bond in the turn region between Asn^5-O-NH-Tyr^7 residues. The structure obtained in decane depicted a β-sheet conformation between residues Trp^3-Asn^5 and Val^8-Leu^{10}.

The structure of TyrB in water had a γ-turn made up of residues Asn[5], Gln[6] and Tyr[7]. This was confirmed by the dihedral angles of Gln[6] (φ_{i+1} =65°, ψ_{i+1} = -77°). There was also a stabilising hydrogen bond between Asn[5] and Tyr[7] (O_i – HN_{i+2}). In decane, TyrB, exhibited a type II' turn between residues Leu[10], Phe[1] and Pro[2] as well as a γ-turn between Asn[5], Gln[6] and Val[8]. The γ-turn was also stabilized by the hydrogen bond between Asn[5] and Tyr[7]. The dihedral angles of Phe[1] and Pro[2] were (φ_{i+1} =78°, ψ_{i+1} = -123°, φ_{i+2} = -70, ψ_{i+2} = -34°) and those of a Gln[6], which confirmed the presence of a γ-turn, were φ_{i+1} =74° and ψ_{i+1} = -69°.

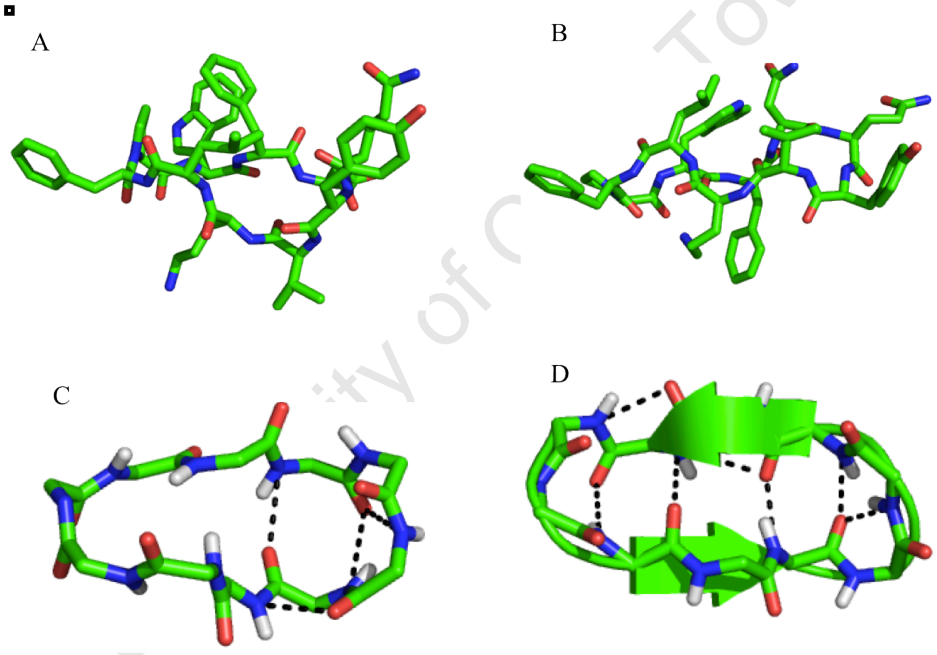

Figure 3.13: Root conformations of TyrB. A is the root conformation in water and B is the root conformation in decane. Only heavy atoms are shown. C and D show the secondary structure elements of TyrB in water and decane respectively. The hydrogen bonds on the root conformations are shown as dotted lines.

The results indicated that the structures of TyrA and TyrC in aqueous and membrane mimetic environments as well as the structure of TyrB in membrane mimetic environment were very similar. This was confirming previous experimental results that

showed that tyrocidine peptides could form β-structures.[65] In the present work, TyrB was unstructured in water, and these results were contrary to what was reported before, where it was shown to adopt a β-structure.[64,65] The structures obtained before formed a β-structures most probably because of the method that was used. The previous structure was obtained from homology modeling based on the gramicidin S template, which is a β-structure. Recent experimental studies on tyrocidine peptides indicated that their secondary structures are likely to be stabilized by self-assembly.[65] It is therefore a possibility that TyrB could form a β-structure upon aggregation. The primary sequences of tyrocidine peptides only differ in residues that occupy position 3 and 4. TyrA is made up of Phe^3/Phe^4, TyrB has Trp^3/Phe^4, whereas TyrC is made up of Trp^3/Trp^4 residues on the respective positions. It is not understood if the variation in the residues at these positions has any role in the differences in structure of tyrocidine peptides in water. Studies on lysine rich cyclic decapeptides revealed that the peptides were unstructured in the aqueous environment and adopted β-structures in a membrane environment.[66] This has also been observed for a number of linear peptides.[62,63] It could therefore mean that TyrB is unstructured in the aqueous phase but changes into an 'active' confirmation upon interaction with the membrane.

3.5 Characterization of the physico-chemical properties of tyrocidine peptides

The main physico-chemical properties that influence antimicrobial properties, hydrophobicity, lipophilicity, charge and amphipathicity were determined for all three tyrocidine peptides and are given in Table 3.7. The calculated physico-chemical properties were similar in all three tyrocidine peptides.

All the three tyrocidine peptides have a net charge of +1. Previous studies have shown that charge ranging from +2 to +5 result in antimicrobial peptide specificity toward microorganisms and that unusually large charge increases the hemolytic nature of peptides.[49, 54-56] It has also been shown that charge plays a pivotal role in the self-promoted uptake of the peptide across the outer membrane barrier.[57] The +1 net charge is not expected to influence their ability to bind to lipid bilayers, as it is relatively small.

The structures obtained for tyrocidine show limited amphipathic properties. Residues Trp^3/Phe^3, Asn^5, Gln^6, Tyr^7, Val^8, and Leu^{10} were on one face, and residues Trp^4/Phe^4 and Orn^9 made up the other face in all the structures except for TyrB in water. The lack of complete separation between hydrophobic and hydrophilic residues reduces the level of amphipathicity of tyrocidine peptides. The amphipathicity of tyrocidine peptides were determined using the ratio Q/L, where Q is the charge, and L is the lipophilicity of the peptide.[58] Lipophilicity was defined via the residue side-chain lipophilicity parameter, pFP,[59] as a summation over all residues of the peptide.[58]

Table 3.7: Physico-chemical properties of tyrocidine A, tyrocidine B and tyrocidine C

Property	Tyrocidine A	Tyrocidine B	Tyrocidine C
Hydrophobicity	70 %	70 %	70 %
Lipophilicity (L)	9.55	10.01	10.47
Charge (Q)	+1.0	+1.0	+1.0
Amphipathicity (Q/L)	0.105	0.100	0.096

Hydrophobicity, defined as the percentage of hydrophobic residues within a peptide,[60] is 70% for all the three tyrocidine peptides. It is an instrumental property for antimicrobial peptide and membrane interactions. It governs the extent to which a peptide can

permeabilize a lipid bilayer.[61] Most antimicrobial peptides are moderately hydrophobic and have a hydrophobicity of about 50%.[61] This allows them to regulate their antimicrobial activities. Peptides that are highly hydrophobic lose specificity and are hemolytic.[61] The relatively high level of hydrophobicity of the tyrocidine peptides could be the reason they are not specific, and are toxic to mammalian cells.

3.6 Conclusion

There was an exceptionally strong agreement between the NMR and MD results for calculations done in water. TyrA and TyrC were structured in water, and there was also a substantial agreement between the calculated and experimental ^{3}J coupling constants. The unstructured TyrB had a poor agreement between the calculated and experimental ^{3}J values. However, both results pointed out that TyrB was unstructured in water. The structures of the tyrocidine peptides in decane were highly similar, they all formed β-structures. There was also a high similarity between the structures of TyrA and TyrC in both water and decane. The structure of TyrB was different in the two environments.

Tyrocidine structures obtained in both water and decane did not exhibit a complete separation of hydrophobic and hydrophilic residues, which shows that they are inherently not amphipathic.

3.7 References

1. Epand RM, Vogel HJ. Diversity of antimicrobial peptides and their mechanisms of action. Biochemica Et Biophysical Acta-Biomembranes 1999;1462:11-28.
2. van't Hof W, Veerman ECI, Helmerhorst EJ, Amerongen AVN. Antimicrobial peptides: Properties and applicability. Journal of Biological Chemistry 2001;382:597-619.
3. Jelokhani-Niaraki M, Prenner EJ, Kay CM, McElhaney RN, Hodges RS. Conformation and interaction of the cyclic cationic antimicrobial peptides in lipid bilayers. The Journal of Peptide Research 2002;60:23-36.
4. Yount NY, Yeaman MR. Immunocontinuum; perspectives in antimicrobial peptide mechanisms of action and resistance. Protein & Peptide Letters 2005;12:49-67.
5. Shai Y. From innate immunity to de-novo designed antimicrobial peptides. Current Pharmaceutica Design 2002;9:715-25.
6. Prenner EJ, Lewis RNAH, McElhaney RN. The interaction of the antimicrobial peptide gramicidin S with lipid bilayer model and biological membranes. Biochimica Et Biophysica Acta (BBA) - Biomembranes 1999;1462:201-21.
7. Jelokhani-Niaraki M, Kondejewski LH, Farmer SW, Hancock REW, Kay CM, Hodges RS. Diastereoisomeric analogues of gramicidine S: Structure, biological activity and interaction with lipid bilayers. Journal of Biochemistry 2000;349:747-55.
8. Prenner EJ, Lewis RN, Neuman SM, Gruner SM, Kondejewski LH, Hodges RS, McElhaney RN. Nonlamellar phases induced by the interaction of gramicidin S with lipid bilayers. A possible relationship to membrane-disrupting activity. Biochemistry 1997;36:7906-7916.

9. Jelokhani-Niaraki M, Prenner EJ, Kondejewski LH, Kay CM, McElhaney RN, Hodges RS. Conformation and other biophysical properties of cyclic antimicrobial peptides in aqueous solutions. Journal of Peptide Research 2001;58:293-306.

10. Yount NY, Bayer AS, Xiong YQ, Yeaman MR. Advances in antimicrobial peptide immunobiology Journal of Peptide Science 2006;84:435-58.

11. Hwang PM, Vogel HJ. Structure-function relationships of antimicrobial peptides. Cell Biology 1998;76:235-46.

12. Bechinger B, Lohner K. Detergent-like actions of linear amphipathic cationic antimicrobial peptides Biochemica Et Biophysical Acta 2006;1758:1529-39.

13. Scolani A, Dalla Serra M, Amodeo P, Mannina L, Vitale RM, Segre AL, Cruciani O, Menestrina G. Structure, conformation and biological activity of a novel lipodepsipeptide from *pseudomonas corrugata*: Cormycin A. Biochemical Journal 2004;384:25-36.

14. Guerrero E, Saugar JM, Matsuzaki K, Rivas L. Role of positional hydrophobicity in the leishmanicidal activity of magainin2. Antimicrobial Agents and Chemotherapy 2004;48:2980-6.

15. Frecer V, Ho B, Ding JL. *De novo* design of potent antimicrobial peptides. Antimicrobial Agents and Chemotherapy 2004;48:3349-57.

16. Bello J, Bello HR, Granados E. Conformation and aggregation of melittin: Dependence on pH and concentration. Biochemistry 1982;21:461-5.

17. Falla TJ, Karunaratne DN, Hancock REW. Mode of action of the antimicrobial peptide indolicidin. Journal of Biological Chemistry 1996;271:19298-303.

18. Cirac A , Moiset G, Mika J , Koçer A, Salvador P, Poolman B, Marrink S , Sengupta D. The molecular basis for antimicrobial activity of pore-forming Cyclic Peptides. Biophysical Journal 2011;100:2422-31.

19. Hancock REW, Chapple DS. Peptide antibiotics. Antimicrobial Agents and Chemotherapy 1999;43:1317-23.

20. Matsuzaki K, Sugishita K, Harada M, Fujii N, Miyajima K. Interactions of an antimicrobial peptide, magainin 2, with outer and inner membranes of gram-negative bacteria. Biochimica Et Biophysica Acta (BBA) - Biomembranes 1997;1327:119-30.

21. Ehrenstein G, Lecar H. Elecrically gated ionic channels in lipid bilayers. Quarterly Reviews of Biophysics 1977;10:1-34.

22. Braunschweiler L, Ernst RR. Coherence transfer by isotropic mixing: Application to proton correlation spectroscopy. Journal of Magnetic Resonance 1983;53:521-8.

23. Jeener J, Meier BH, Bachmann R, Ernst RR. Investigation of exchange processes by two-dimensional NMR spectroscopy. Journal of Chemical Physics 1979;71:4546-53.

24. Bax A, Davis DG. Practical aspects of two-dimensional transverse NOE spectroscopy. Journal of Magnetic Resonance 1985;63:207-13.

25. Sklenar V, Piotto M, Leppik R, Saudek V. Gradient-tailored water suppression for $^{1}H—^{15}N$ HSQC experiments optimized to retain full sensitivity. Journal of Magnetic Resonance 1993;102:241-5.

26. Wuthrich K. NMR of proteins and nucleic acids. New York: John Wiley & Sons; 1986.

27. Thomas PD, Basus VJ, James TL. Protein solution structure determination from two-dimensional nuclear overhauser effect experiments: Effect of approximations on the

accuracy of derived structures. Proceedings of the National Academy of Sciences 1991;88:1237-41.

28. Berendsen HJC, Van der Spoel D, Van Drunen R. GROMACS: A message-passing parallel molecular dynamics implementation. Computational Physics Communication 1995;91:43-56.

29. Jorgensen WL, Severence DL. Aromatic-aromatic interactions: Free energy profiles for the benzene dimer in water, chloroform, and liquid benzene. Journal of the American Chemical Society 1990;112:4768-74.

30. Berendsen HJC, Postma J, van Gunsteren WF, Hermans J. Interaction models for water in relation to protein hydration. Dordrecht: D. Reidel 1981.

31. Berendsen H, Postma J, DiNola A, Haak J. Molecular dynamics with coupling to an external water bath. The Journal of Chemical Physics 1984;81:3684-90.

32. Hess B, Bekker H, Berendsen HJC, Fraaije, J. G. E. M. LINCS: A linear constraint solver for molecular simulations. Journal of Computational Chemistry 1997;18:1463-72.

33. Tieleman DP, Marrink S , Berendsen HJC. A computer perspective of membranes: Molecular dynamics studies of lipid bilayer systems. Biochemica Et Biophysical Acta 1997;1331:235-70.

34. van Buuren AR, Marrink SJ, Berendsen HJC. A molecular dynamics study of the decane/water interface. Journal of Physical Chemistry 1993;90:9206-12.

35. Leiu DC, Nocedal J. On the limited memory BFGS method for large scale optimization. MATHEMATICAL PROGRAMMING 1989;45:503-28.

36. Kabsch W, Sander C. Dictionary of protein secondary structure: Pattern recognition of hydrogen bonded and geometric features. Biopolymers 1983;22:2577-637.

37. van der Spoel D, Lindahl E, Hess B, van Buuren AR, Apol E, Meulenhoff PJ, Tielemann DP, Sijbers ALTM, Feenstra KA, Van Drunen R, et al. Gromacs user manual, version 3.3. 2005.

38. Szilagyi L. Chemical shifts in proteins come of age. Progress in Nuclear Magnetic Resonance Specroscopy 1995;27:325-443.

39. Szilagyi L, Jardetzky O. Alpha-proton chemical shifts and secondary structure in proteins. Journal of Magnetic Resonance 1989;83:441-9.

40. Wishart DS, Sykes BD, Richards FM. The chemical shift index: A fast and simple method for the assignment of protein secondary structure through NMR spectroscopy. Biochemistry 1992;31:1647-51.

41. Shen Y, Bax A. Protein backbone chemical shifts predicted from searching a database for torsion angle and sequence homology. Journal of Biomolecular NMR 2007;38:289-300.

42. Pardi A, Wagner G, Wuthrich K. Protein conformation and proton nuclear- magnetic resonance chemical shifts. European Journal of Biochemistry 1983;137:445-54.

43. Neal S, Nip A, Zhang H, Wishart D. Rapid and accurate calculation of protein 1H 13C and 15N chemical shifts. Journal of Biomolecular NMR 2003;26:215-40.

44. Wang Y, Jardetzky O. Investigation of the neighboring residue effects on protein chemical shifts. Journal of American Chemical Society 2003;26:215-40.

45. Williamson MP. Secondary-structure dependent chemical shifts in proteins. Biopolymers 1990;29:1423-31.

46. Dyson HJ, Wright PE. Two-dimensional NMR spectroscopy applications for chemists and biochemists. New York: VCH; 1994. .

47. Pardi A, Billeter M, Wuthrich K. Calibration of the angular dependence of the amide proton-C_a proton coupling constants $^3J_{NHa}$ in globular protein. use of $^3J_{NHa}$ for identification of helical secondary structure. Journal of Molecular Biology 1984;180:741-51.

48. Teng Q. Structural biology: Practical NMR applications. New York: Springer + Bussiness Media; 2010.

49. Wilmot CM, Thornton JM. Analysis and predictition of the different types of b-turns in proteins. Journal of Molecular Biology 1988;203:221-32.

50. Hutchinson EJ, Thornton JM. PROMOTIF - A program to identify and analyze structural motifs in proteins. Protein Science 1996;5:212-20.

51. Gibbons WA, Beyer CF, Dadok J, Sprecher RF, Wyssbrod HR. Studies of individual amino acid residues of the decapeptide tyrocidine A by proton double-resonance difference spectroscopy in the correlation mode. Biochemistry 1975;14:420-9.

52. Kuo MC, Gibbons WA. Nuclear overhauser effect and cross-relaxation rate determinations of dihedral and transannular interproton distances in the decapeptide tyrocidine A, Biophysical Journal 1980;32:807-36.

53. Wishart DS, Case DA. Use of chemical shifts in macromolecular structure determination. Methods in Enzymology 2001;338:2-34.

54. Dathe M, Nikolenko H, Meyer J, Beyermann M, Bienert M. Optimization of the antimicrobial activity of magainin peptides by modification of charge. FEBS Letters 2001;501:146-50.

55. Bessalle R, Haas H, Goria A, Shalit I, Fridkin. M. Augmentation of the antibacterial activity of magainin by positive-charge chain extension. Antimicrobial Agents and Chemotherapy 1992;36:313-7.

56. Dathe M, Wieprecht T, Nikolenko H, Handel L, Maloy WL, MacDonald DL, Beyermann M, Bienert M. Hydrophobicity, hydrophobic moment and angle subtended by charged residues modulate antibacterial and haemolytic activity of amphipathic helical peptides. FEBS Letters 1997;403:208-12.

57. Hancock REW, Monisha SG. The role of antimicrobial peptides in animal defenses. PNAS 2000;16:8856-61.

58. Frecer V. QSAR analysis of antimicrobial and haemolytic effects of cyclic cationic antimicrobial peptides derived from protegrin-1. Bioorginic & Medicinal Chemistry 2006;14:6065-74.

59. Fauchere JL, Pliska V. Hydrophobic parameters pi of amino acide chains from the partitioning of N-acetyl-amino-acid amides. European Journal of Medicinal Chemistry 1983;18:369-75.

60. Yeaman MR, Yount NY. Mechanisms of antimicrobial peptide action and resistance. Pharmacological Reviews 2003;55:27-55.

61. Wieprecht T, Dathe M, Krause E, Beyermann M, Maloy WL, MacDonald DL, Bienert M. Modulation of membrane activity of amphipathic, antibacterial peptides by slight modifications of the hydrophobic moment. FEBS Letters 1997;417:135-40.

62. Bello J, Bello HR, Granados E. Conformation and aggregation of melittin: Dependence on pH and concentration. Biochemistry 1982;21:461-5.

63. Falla TJ, Karunaratne DN, Hancock REW. Mode of action of the antimicrobial peptide indolicidin. Journal of Biological Chemistry 1996;271:19298-303.

64. Marques MA, Citron DM, Wang CC. Development of tyrocidine A analogues with improved antibacterial activity. Bioorganic & Medicinal Chemistry 2007;15:6667-77.

65. Spathelf BM. Qualitative structure-activity relationships of the major tyrocidines, cyclic decapeptides from bacillus aneurinolyticus. PhD Thesis; Stellenbosch University; 2010.

66. Cirac AD. Mechanism of action of cyclic antimicrobial peptides. PhD Thesis; Universitat de Girona; 2010.

67. Pal D, Chakrabarti P. (2002) On residues in the disallowed region of the ramachandran map, Biopolymers 2002; 63:195-206.

68. Mahalakshmi R., and Balaram, P. The use of D-amino acids in peptide design, in *D-Amino Acids: A New Frontier in Amino Acid and Protein Research - Practical Methods and Protocols* (Konno, R., Bruckner, H., D'Aniello, A., Fisher, G., and Fujii, N., Eds.) 2007; 1st Ed., pp 415-430 Gazelle Distribution.

Chapter 4

Mechanism of self-assembly/aggregation of tyrocidine in aqueous solution

4.1 Introduction

Small, linear and cyclic peptides are known to aggregate in different ways in different environments and this influences their activities as antimicrobial peptides. Tyrocidine peptides have also been shown to aggregate in solution.[1-5] A peptide similar to tyrocidine, gramicidin S, is known to aggregate when it interacts with the membrane. The resultant aggregate of gramicidin S forms a channel structure that destroys the cell potential,[6, 7] resulting in cell death. Smaller cyclic D and L-α-peptides have been extensively studied. They form planar conformations and aggregate by stacking on top of each other resulting in a hollow channel where all the side chains in the peptides lie on the outside of the channel.[8-11] A beta-sheet forming cyclic peptide, protegrin also aggregates by sideways overlap as it disrupts the membrane lipid.[12]

Studies have shown that self-association and multimerization are crucial for peptide activity.[13] It is therefore important to understand the role of self-association in the mechanism of action of tyrocidines. It is not known if tyrocidine peptides self-associate on the extracellular side of the membrane or inside the membrane. There is also a need to

understand if there are any structural changes of tyrocidine as it self-associates or as it moves into the membrane, as these conformational changes may influence its mode of action.

This study seeks to elucidate the aggregation process of TyrC in water. To understand this, the dimerization process was studied first. Classical molecular dynamics, steered molecular dynamics and umbrella sampling simulations were performed to determine the most favorable dimerization state, driving forces of dimerization and the possible dimerization pathways. The ability of tyrocidine to form oligomers was then studied using systems containing four, six and twelve peptides and the simulation data was compared to DOSY experimental data.

4.2 Methods

All simulations and analysis were performed using the GROMACS software package.[14] The OPLS force field was used.[15] The peptides were solvated using the Simple Point Charge (SPC) water model.[16]

Simulations were performed using periodic boundary conditions. The solvated peptides were energy minimized using a steepest descent algorithm. The initial velocities used for equilibrating the system were taken from a Maxwell distribution. The temperature was kept constant using weak coupling to a temperature bath[17] and with a coupling constant of 0.1 ps. Protein and solvent were coupled independently to a temperature bath. All covalent bonds were constrained using the LINCS algorithm,[18] which allows the use of a 2 fs time step.

4.2.1 Dimerization simulation

Four 100 ns MD simulations of TyrC were performed in water at 300 K in order to investigate dimerization of the peptide. To determine if the resultant conformations were independent of the starting conformations different starting configurations were used. The first configuration was generated such that the peptides were more than 1.2 nm apart making sure that their backbone atoms were in the same plane. Rotating one peptide by 90 degrees with respect to the previous conformation systematically derived three additional conformations. The rotation was performed along the y-axis. The peptide was rotated by 90, 180, and 270 degrees. The rotation of the peptides along the y-axis was performed using the program InsightII software program (Accelrys Inc.).

4.2.2 Effect of temperature on dimerization

Molecular dynamics at high temperature allows systems to sample a larger conformational space[19] and can therefore be used to generate new conformations. The simulations of the four starting configurations generated above were repeated at 400 K in order to investigate the effect of temperature on the dimerization process of TyrC. A temperature of 400 K was used because it was high enough to allow the system to sample a relatively large conformational space compared to what was sampled at 300 K. At the same time the pressure was increased in order to prevent the water from boiling, The parameters used are described under the methods section.

4.2.3 Steered molecular dynamics

In order to generate the potential of mean force (PMF) for each system, COM pulling and umbrella sampling simulations were carried out. The representative structures of the first five most populous clusters obtained from the MD simulation at 400 K were used as the

starting structures for the COM pulling simulations. For each simulation, the starting structure was placed on one end of a box of dimensions 6.6 nm × 4.4 nm × 9.0 nm making sure that the minimum image convention requirement was satisfied. The COM pulling simulations were done using GROMACS and the OPLSA forcefield.[14, 15] The LINCS algorithm was used to constrain all bonds.[18] The simulation box was solvated in SPC water.[16] After solvation the system was energy minimized using the steepest descents algorithm. Equilibration was subsequently performed and the peptides were position restrained during this process. All the simulations were carried out at 300 K using a 2 fs integration time step.

One of the peptides in the dimer was pulled along the z-direction, which was determined as the reaction coordinate while the other one was kept fixed during the pulling process. The peptide was pulled with a force of 1000 $kJmol^{-1}nm^{-2}$ at two different rates, 0.01 nm/ps^{-1} for a simulation of 500 ps and 0.001 nm/ps^{-1} for a simulation time of 2.5 ns.

4.2.4 Potential of mean force

Umbrella sampling windows were generated from the pulling simulation trajectories. A force constant of 5000 $kJmol^{-1}nm^{-2}$ during umbrella sampling. A distance of 0.01 nm in the slower pulling simulations separated the windows from each other. This gave a total of about thirty umbrella sampling windows from each of the five pulling simulations. The faster pulling simulation generated thirty umbrella simulation sampling windows that were separated from each other by 0.1 nm. Each umbrella simulation was run for 10 ns. During the umbrella sampling a biasing potential was used. WHAM was also used to

generate the Potential of Mean Force (PMF) profiles.[20] The umbrella sampling simulations from the different pulling rates were combined and a total of 60 umbrella sampling windows were used in this process. The error associated with the PMFs was calculated using the bootstrapping method.[20]

4.2.5 Aggregation simulations

Twelve copies of the monomer from MD of tyrocidine C in water were placed in a box of 637 nm^3 (8.9 nm × 9.8 nm × 7.3 nm). The peptides were solvated such that the final concentration was approximately 20 mM. Two other systems were also simulated at lower concentration (Approximately 10 mM). In these cases the simulation boxes consisted of six and four peptides surrounded by water molecules. In order to ascertain the multimerization as well as the size of aggregates of TyrC in solution, Diffusion-ordered 2D NMR spectroscopy (DOSY) were performed in collaboration with Professor Katalin Köver (University of Debrecen, Hungary).

4.3 Results/Discussion

4.3.1 Dimerization

The peptides were regarded as bound together when the center of mass separation distance between them was less than 1.2 nm as this was the cut-off value used for the non-bonded interactions. The angle between the planes of the two peptides was also calculated to determine the orientation of the peptides in the dimer. Figure 4.1 shows that, at 300 K, once the peptides aggregate, they take a very long time to separate. This indicates the stability of the dimers that are being formed. The distance between the centers of mass of the two peptides decreases rapidly to < 1.0 nm in under 25 ns in all the

simulated systems. Once they aggregate pair 2 and pair 3 (Figure 4.1a) do not separate. In pair 1 the peptides dimerize in the first 15 ns and stay attached for the next 30 ns after which they start to randomly attach and separate for the rest of the simulation. Pair 4 quickly dimerizes (< 10 ns) and the peptides remain bound to each other for 5 ns. After 10 ns the COM separation increases rapidly from 0.9 nm to 1.7 nm before decreasing again to 1 nm just after 20 ns. Besides a small increase in COM between 60 – 70 ns, the COM remained at < 1 nm for the rest of the simulation.

At 400 K, it was observed that the peptides kept coming together and separating, at times moving quite far apart. This occurred in all the four simulations. This gave the peptides the ability to interact again, possibly with a different orientation when they came together again, allowing them to sample a larger conformational space.

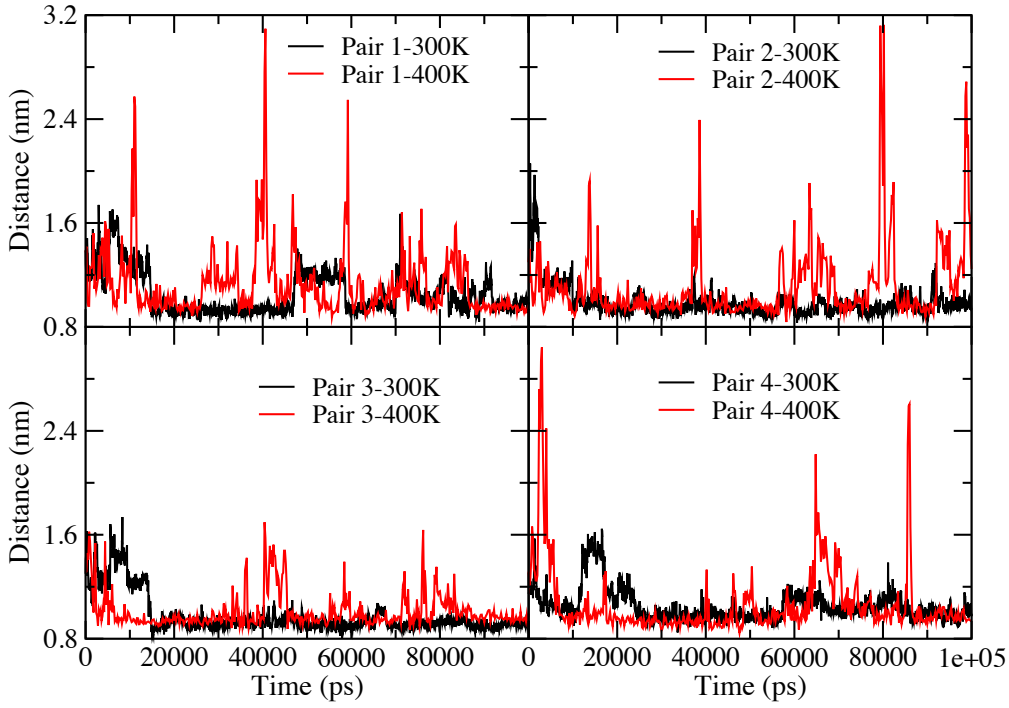

Figure 4.1: Center of mass separation distance between peptides as a function of time.

In order to determine the variation of the orientation of the peptides in the systems, the angle between the planes of the two peptides in the systems were monitored. Three atoms on the backbone ring Trp^4CA, Val^8CA and Orn^9CA were used to define the plane of each peptide. The angle that was generated by the normal to the two respective planes was then measured. The variation in this angle is shown in Figure 4.2. There were fewer and gradual changes in the orientation of the planes of the two peptides at 300 K compared to the ones observed at 400 K. This suggests that, peptides stayed in the same orientation for longer periods of time at 300 K compared to 400 K. It can be seen from Figure 4.2 that Pair 1 (300K) had five transitions between 0ns - 10 ns, 10 ns - 25 ns, 25 ns - 50 ns, 50 ns - 80 ns and 80 ns – 100 ns. The biggest angle transition recorded during the simulation occurred between 47 ns and 80 ns, and resulted in a rotation of 150^0 in 33 ns. In Pair 2 the angle between the peptides decreases slowly from about 140^0 after 20 ns until it reaches 50^0 at 75 ns making a rotation of 90^0 in 45 ns. The angle started to increase very slowly at 75 ns to the end of the simulation indicating a gradual change in the orientation of the peptides. Pair 3 (300K) and Pair 4 (300K) show two and three transitions respectively. The angle in Pair 3 (300K) stays around 160^0 from 25ns to 75 ns before changing to 55^0 and stays the same for the rest of the simulation. In Pair 4 the angle stays around 150^0 from 20 ns to around 70 ns where upon it abruptly changes to 65^0 before it begins to slowly change back to 150^0 in about 10 ns.

The fact that the peptides were next to each other for a long time and did not change their orientations indicates that only a small conformational space was sampled at 300 K. At 400 K the number of times the angle between the planes of the peptides changed increased. This, together with the variation in COM indicates that the energy of dimerization is not very large.

To gain more insight into the conformational space that was sampled by the dimers, the trajectories of the four different simulations at 300 K were combined to produce the root mean square deviation (RMSD) matrix shown on Figure 4.3. The blue color indicates that the structures are very similar and the red color shows that they are different. The RMSD indicates that each simulation sampled an independent region of conformational space. This is because there are many red areas as we move away from the diagonal, which means there was very little overlap of the dimers sampled by the different simulations. There were small overlaps between Pair 1 and Pair 2 as well as between Pair 1 and Pair 3 as indicated by the small yellow areas in the intersecting areas of the RMSD matrix. These results show that very long simulations are required to completely sample the dimer conformational space.

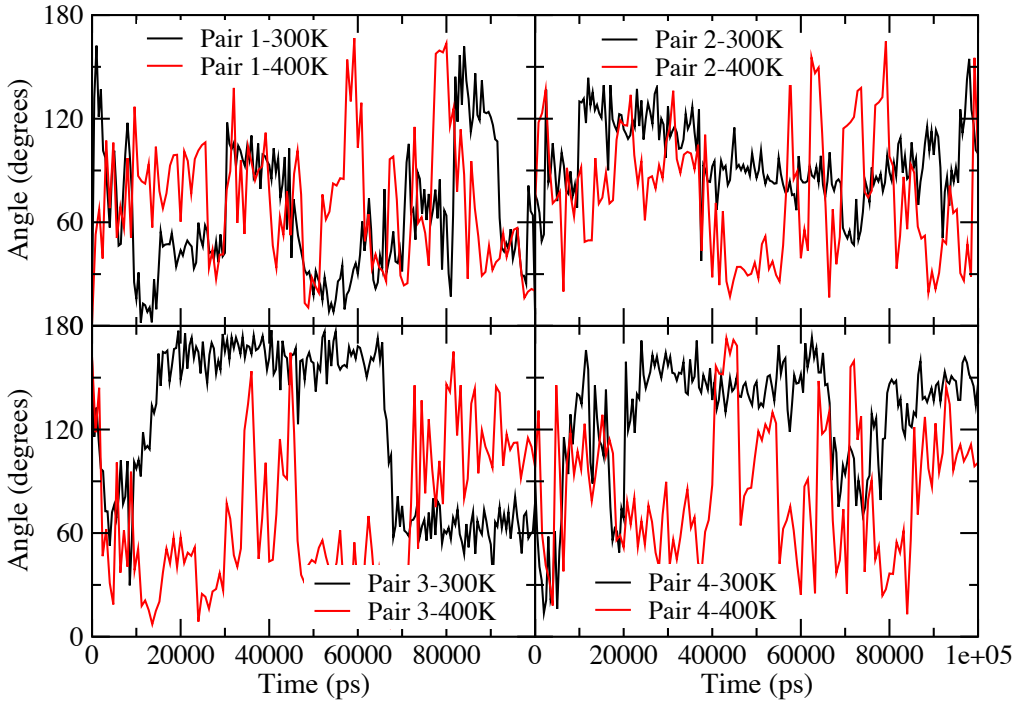

Figure 4.2: Variation of the angle between planes of peptide pairs as a function of time at 300 K and 400 K

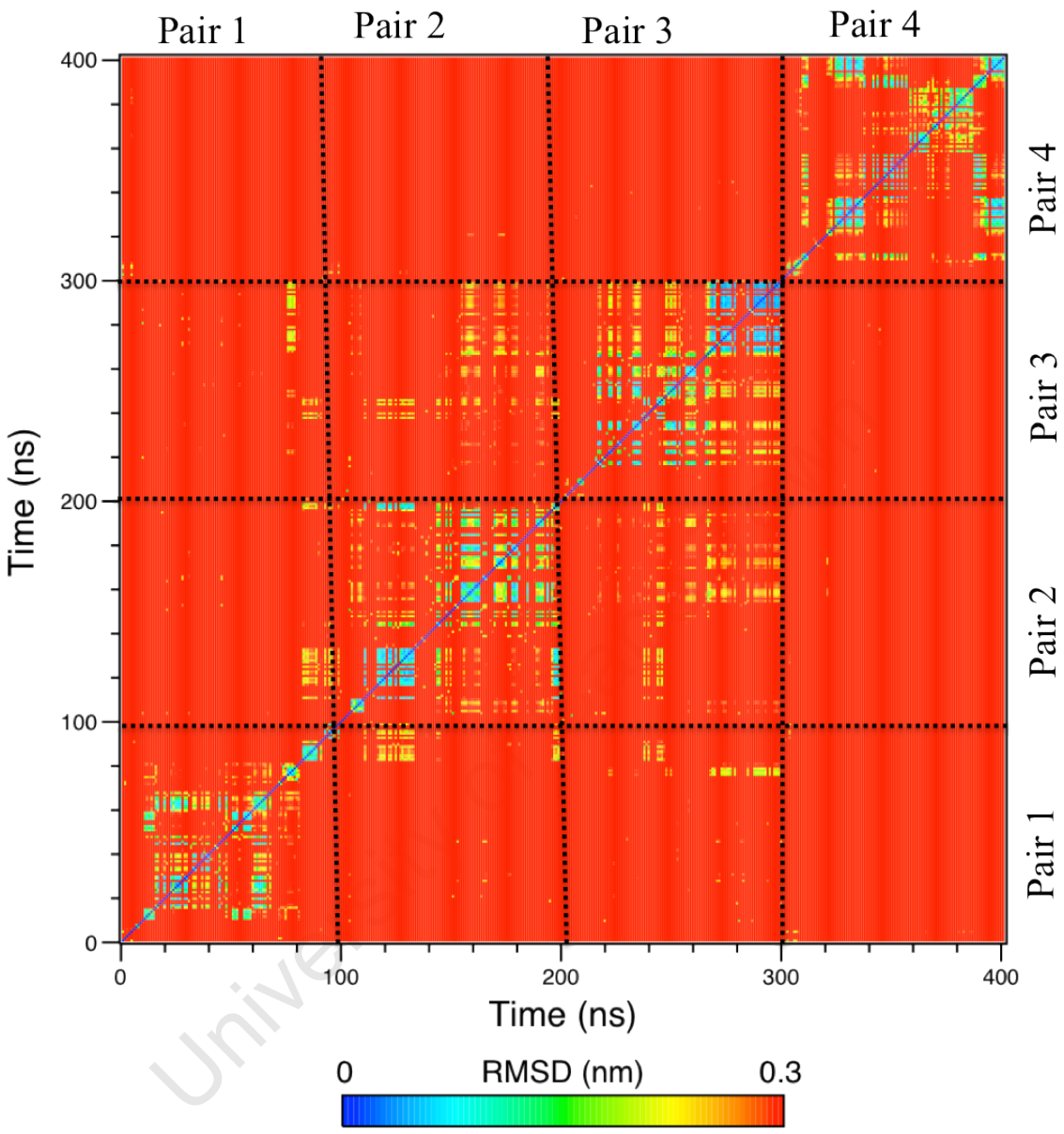

Figure 4.3: Root mean square deviation (RMSD) matrix of the dimer for the four simulations Pair 1, Pair 2, Pair 3 and Pair 4 of 100ns each. The values were calculated based on the backbone atoms. Two conformations were regarded as different when the RMSD value was greater than 0.30 nm. The simulations were performed at 300 K.

All of the starting conformations except Pair 3 did not result in any change in the secondary structure elements of the individual peptides in the dimers at 300 K. This can be confirmed by the evolution of secondary structure elements shown in Figure 4.4. The individual monomers maintained their secondary structure elements for most of the simulation. This basically means that the resultant dimers were formed by individual peptides coming together in different orientations without influencing the conformation of the monomers. Only Pair 3 showed a change in the secondary structure elements of Trp^3 in both peptide 1 and peptide 2 after 60 ns. The RMSD matrix shows that the dimer was sampling the same conformational space during this period. Figure 4.5 shows that the dimer of Pair 3 forms between 3 and 4 backbone-backbone hydrogen bonds during this period. This was because the peptides were forming a dimer by coming together a in sideways overlap.

The number of backbone-backbone intermolecular hydrogen bonds formed between the two peptides during the simulations is shown in Figure 4.5. At 300 K there were very few backbone-backbone hydrogen bonds formed between the two peptides. This basically indicates that the dimers formed were likely stabilized by hydrophobic interactions. Pair 3 formed between two and four backbone-backbone hydrogen bonds for the last 40 ns of the simulation, which was the largest number of backbone-backbone hydrogen bonds formed. These backbone-backbone hydrogen bonds resulted in a change in the secondary structure of residues Trp^3 in both peptides from bends to β-sheets. Pair 2 contains only one backbone-backbone hydrogen bond that was quite consistent for the

duration of the simulation but had no influence on the secondary structure of the individual peptides.

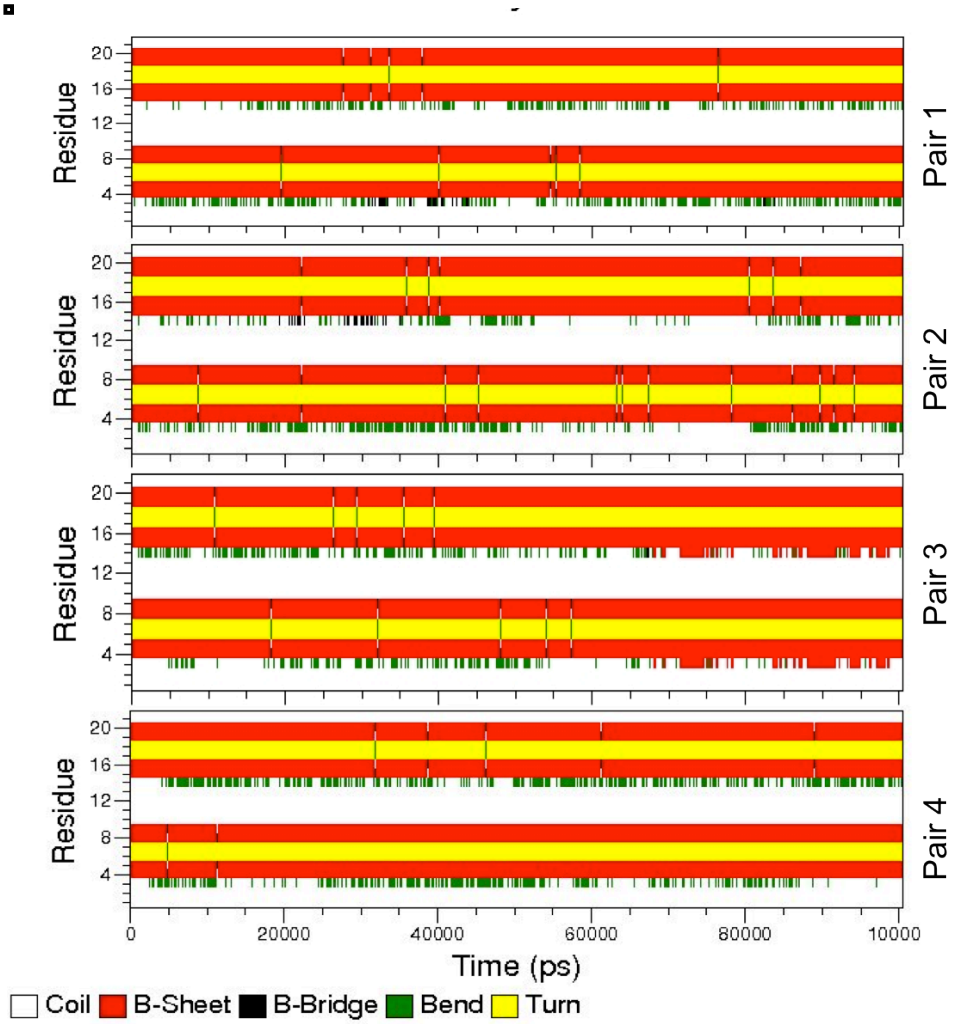

Figure 4.4: Secondary structure elements of peptides as a function of time in Pair 1, Pair 2, Pair 3 and Pair 4 at 300 K.

The number of backbone-backbone hydrogen bonds formed by Pair 1 kept changing between one and two from 30 ns - 40 ns. It also formed a backbone-backbone hydrogen bond that was not very consistent between 82 ns to 90 ns. It however showed no backbone-backbone hydrogen bonds for a good part of the simulation. During the time

when Pair 1 had backbone-backbone hydrogen bonds it was noted that Trp^3 from peptide 1 assumes a β-bridge secondary structure (data not shown). Pair 4 did not form any backbone-backbone hydrogen bonds for the duration of the simulation. However, the peptides in Pair 4 were bound to each other for the good part of the simulation as indicated in Figure 4.1. The RMSD matrix of pair 4 also indicates that there were areas where it was sampling dimers of the same conformation. These observations together with the lack of intermolecular backbone-backbone hydrogen bonds indicate that the dimers formed by Pair 4 were stabilized by hydrophobic interactions.

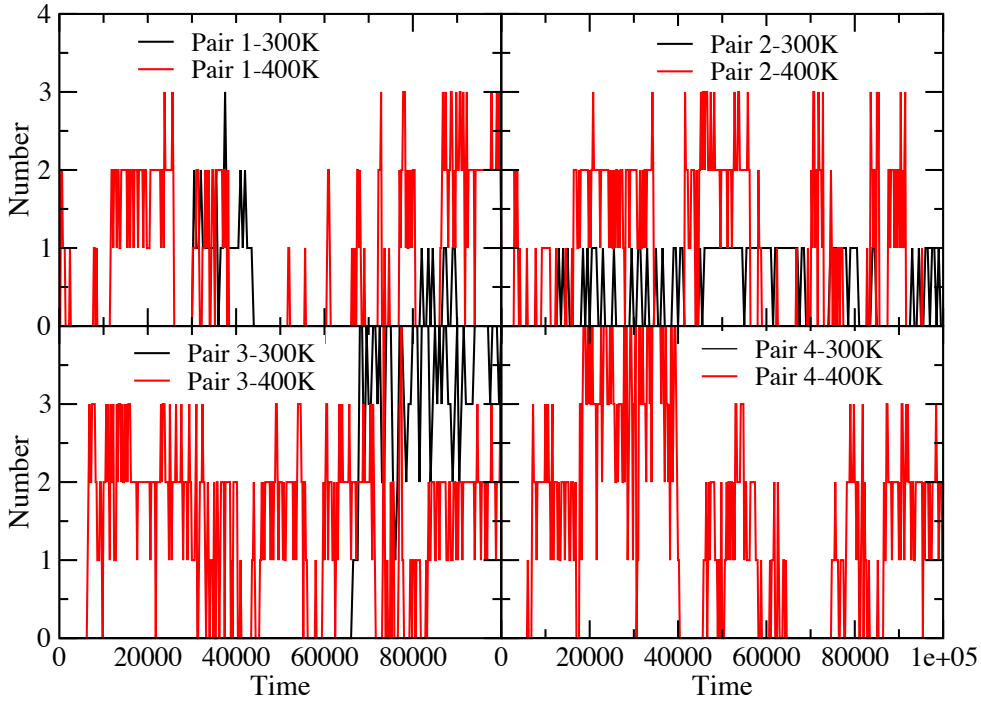

Figure 4.5: Variation of the backbone-backbone intermolecular hydrogen bonds with time at 300 K and 400 K

The 400 ns trajectory from the combined 100 ns simulation trajectories was used to determine the main dimer conformations in water. Dimer conformations were placed into different clusters using the method described in.[14] A least square rotational and translational fit was done on the backbone atoms of peptide A of each structure that was saved in the trajectory. Backbone atoms (N, Cα, C) of the whole structure were then used in determining the root-mean-square-difference (RMSD). Structures were regarded as similar if their atom-positional root-mean-square difference (RMSD) was ≤ 0.30 nm. The structure with the largest number of neighbors and all its neighbors were regarded as a cluster and eliminated from the pool of clusters. The process was repeated until all the structures were put in their respective clusters.

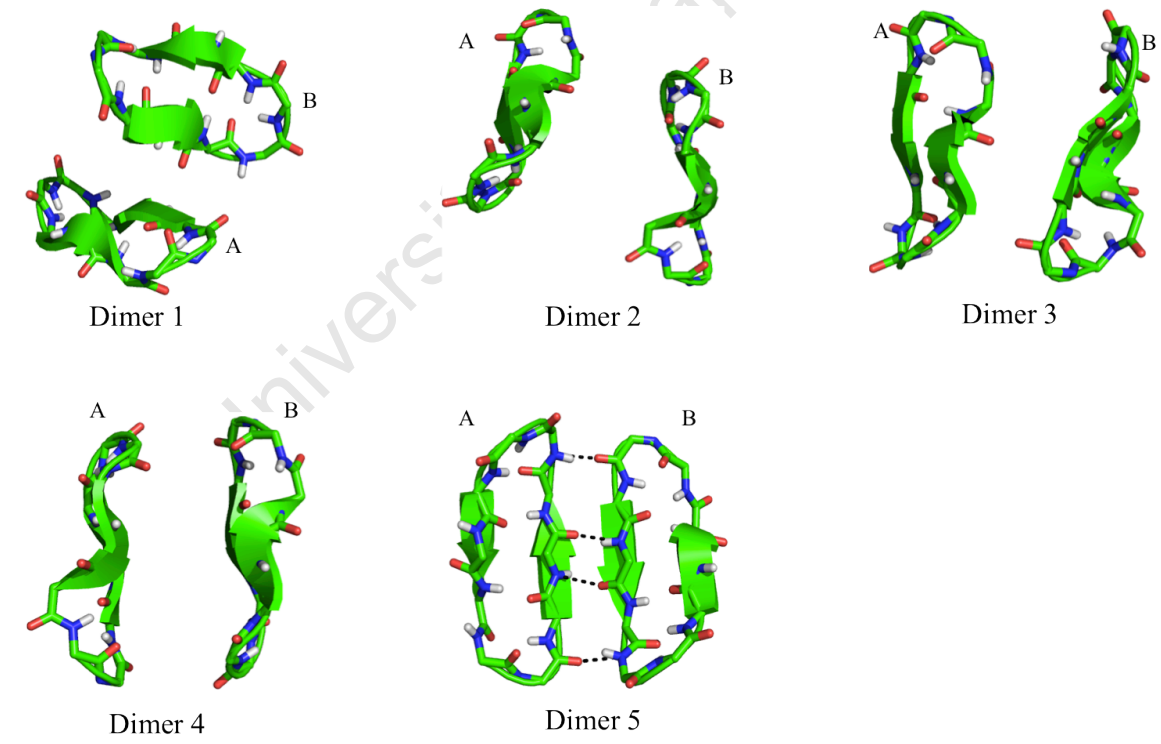

Figure 4.6: Backbone and secondary structure elements of the representative clusters of the dimer found from the 400 ns simulation. The similarity criterion of backbone RMSD ≤ 0.3 nm was used to cluster the dimers. The simulations were performed at 300 K.

The representative structures of the first five most populated clusters are shown in Figure 4.6. Only the backbone structures of the dimers are depicted. Cluster 1 is made of structures mainly from pair 2 (100 ns – 200 ns) and pair 3 (200 ns – 300 ns) and only four structures from Pair 1. Cluster 2 has structures from Pair 1 and Pair 3 only. Cluster 3 is made up of structures from Pair 4 only and cluster five has a mixture of structures from Pair 1 and 2. The first three clusters are almost of the same size and contain close to 17% of the total conformations sampled (see Figure 4.7). Only Cluster 5 contains an average of 3 backbone-backbone hydrogen bonds between the monomers in the dimer. All the other clusters contain less than two with a good number having zero backbone-backbone hydrogen bonds. It was noted that some dimers are stabilized by π-stacking interactions between Phe^{1} in peptide A and Trp^{3} in peptide B and between Trp^{3} in peptide A and Trp^{3} in peptide B.

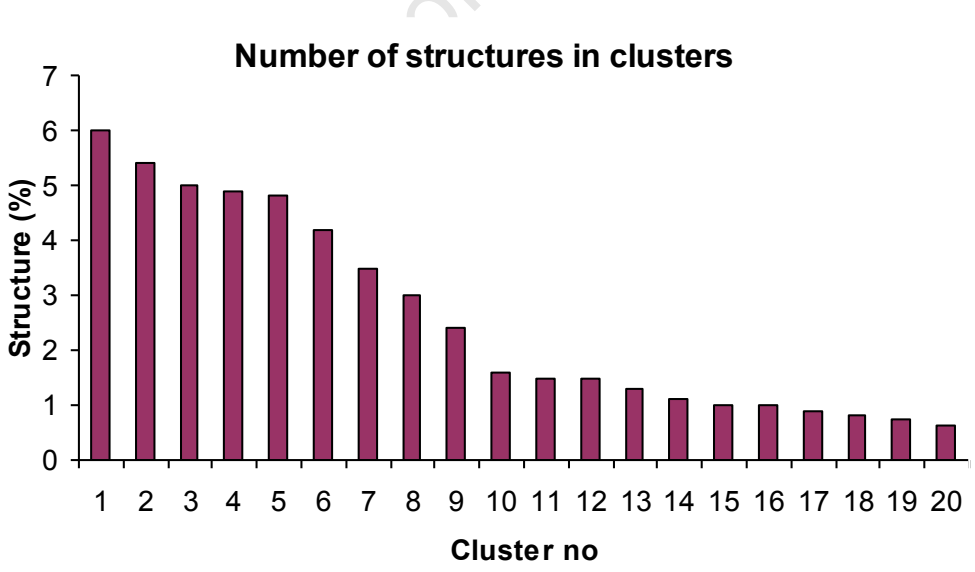

Figure 4.7: Size of the first twenty 20 clusters of the dimer simulation at 300 K for a combined simulation time of 400 ns. Clusters were obtained by using a similarity criterion of backbone RMSD < 0.30 nm.

There were several observations from the RMSD matrix (Figure 4.3) and cluster analysis of the dimer simulations performed. The first one is that dimers were formed by peptides either associating sideways or by stacking on top of each other. The dimers formed through sideways association were mainly stabilized by hydrogen bonding while the other dimers were stabilized by hydrophobic interactions. Another observation was the limited number of off diagonal elements on the RMSD matrix, which shows a lack of conformational overlap between the structures. It was also noted that the resultant dimers were highly dependent on the starting configurations.

The resultant simulations show that at 100 ns there are several possible dimers that can be formed. However most of these dimer states appear to be metastable, hence it is not possible to point out the preferred dimer conformation.

4.3.2 Effect of temperature on dimerization

The number of metastable dimers obtained at 300 K was the main motivation to do the simulations at a higher temperature. It is known that at high temperatures, systems are able to traverse energy barriers, allowing them to sample large conformational spaces.[19, 21] The variation of the COM distance with time in Figure 4.1 clearly shows that there was an increase in the number of times the peptides associated and dissociated at 400 K. This resulted in an increase in the area that was sampled by the peptide dimers. However a closer look at Figure 4.1 shows that after dissociating, the peptides quickly associated again. The RMSD matrix (Figure 4.8) showed a relatively small increase in the conformational space that was sampled by the dimers, as there were more non-blue

elements away from the diagonal compared to Figure 4.3. At 300 K the resultant dimers were very dependent on the starting structure.

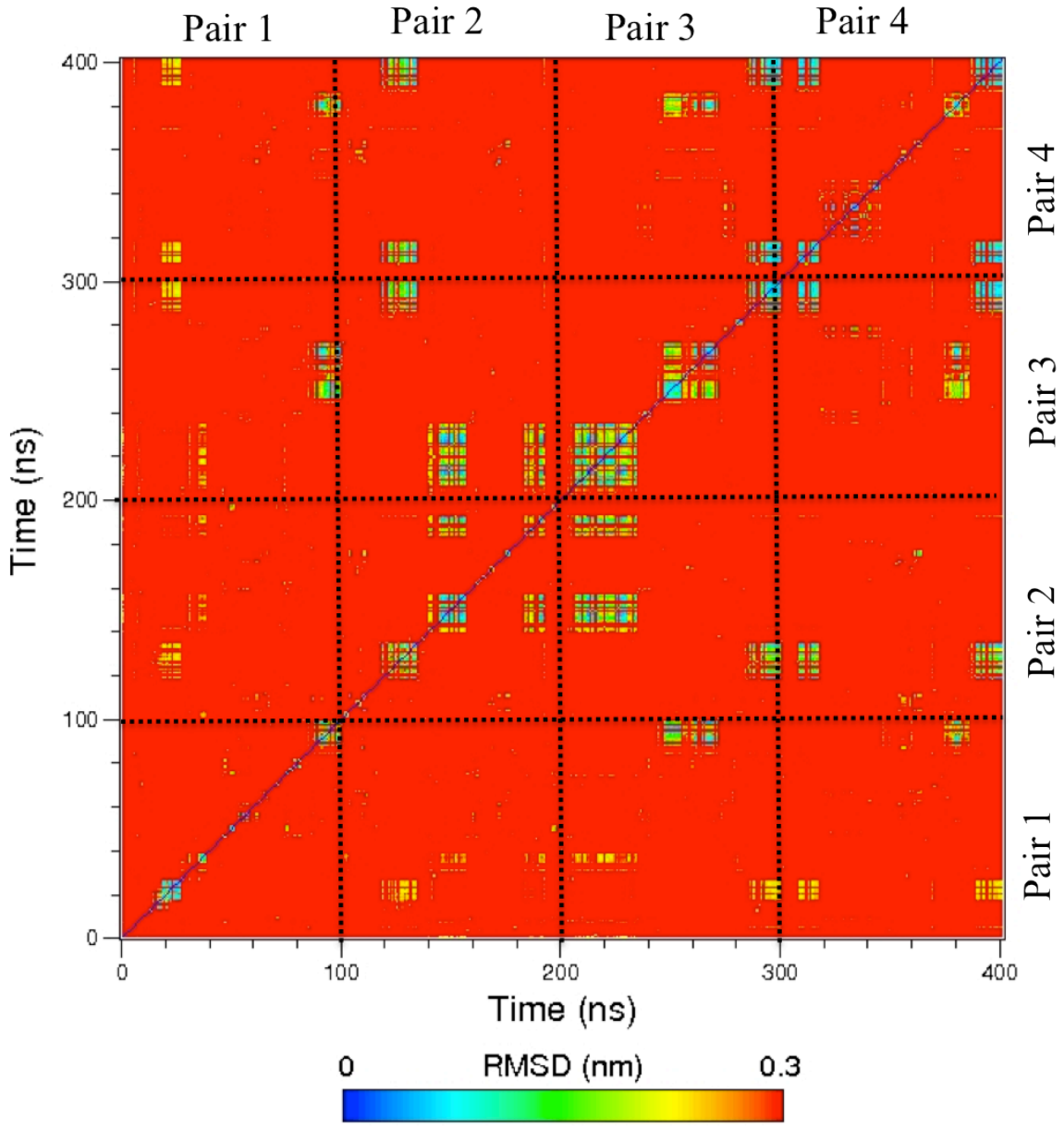

Figure 4.8: Root mean square deviation (RMSD) matrix of the dimer for the four simulations Pair 1, Pair 2, Pair 3 and Pair 4 of 100ns each. The values were calculated based on the backbone atoms. Two conformations were regarded as different when the RMSD value was greater than 0.30 nm. The simulations were performed at 400 K.

It is expected that the peptides might lose their secondary structure elements at high temperature. Though there were very small changes, the secondary structure elements of the peptides were very similar to the ones obtained at 300 K as shown in Figure 4.9. The ability to maintain the secondary structure by the cyclic peptides is attributed to the rigidity introduced by cyclisation and the NMR restraints that were used. At 300 K there were very few intermolecular backbone-backbone hydrogen bonds formed between the peptides when they associated, there was however a substantial increase in the backbone-backbone hydrogen bonds at 400 K as shown in Figure 4.5.

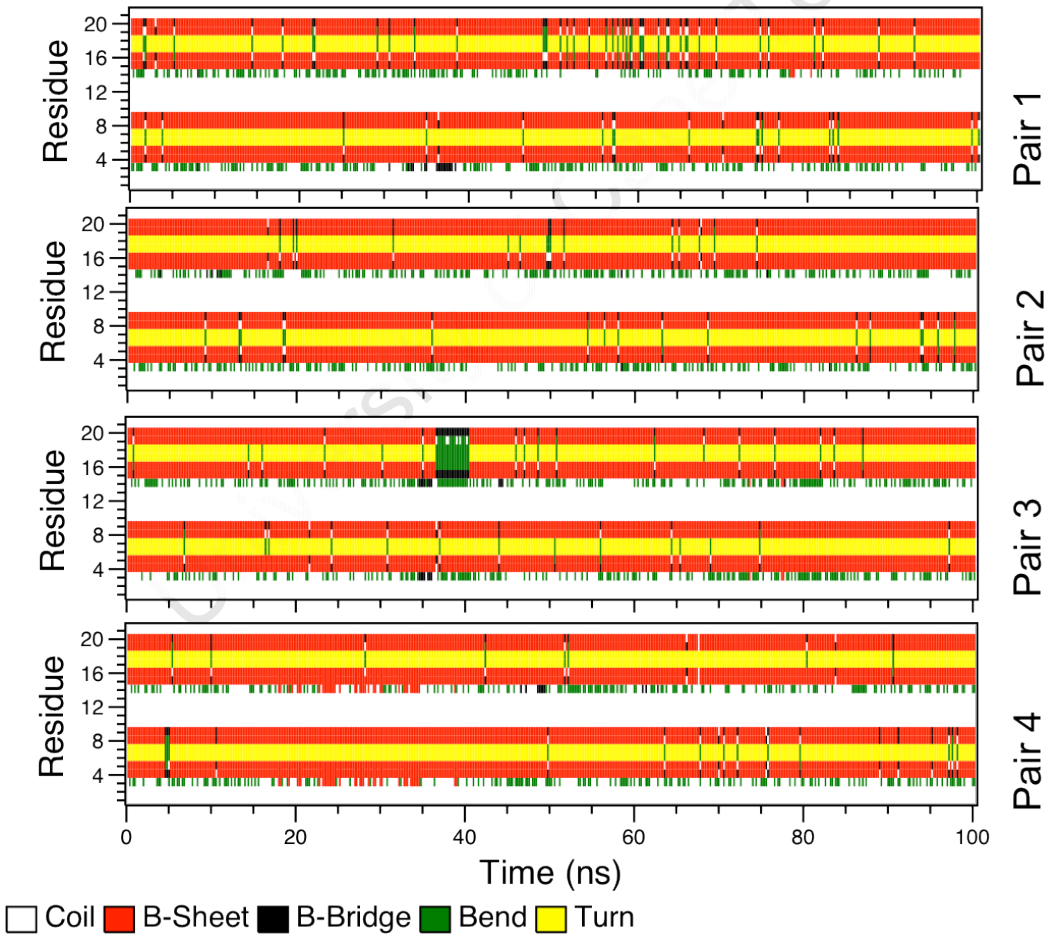

Figure 4.9: Secondary structure elements of peptides as a function of time in Pair 1, Pair 2, Pair 3 and Pair 4 at 400 K.

The first five most populated clusters of the dimers obtained at 400 K are shown in Figure 4.10; only the backbone of the representative structure in each dimer cluster is depicted. It was observed that the resultant dimers form both parallel and antiparallel β-sheets. These were formed by dimers coming together in different ways. The most populated cluster of the dimers has anti-parallel β-sheets between the two peptides. It was observed that in Dimer 2 and Dimer 3, monomer B attaches to opposite sides of monomer A. There were other different types of dimers that were formed. The ability to form different types of dimers where the peptides were bound together in different orientations and on different sides of either peptide points to the fact that it might be possible for peptides to be added on either side of the dimer, forming polymers. This is one of the properties that can be utilized by the peptide to disrupt the membrane where the polymerized peptides traverse the membrane barrier forming a non-partial ion channel in the membrane, which can cause the death of the cell.

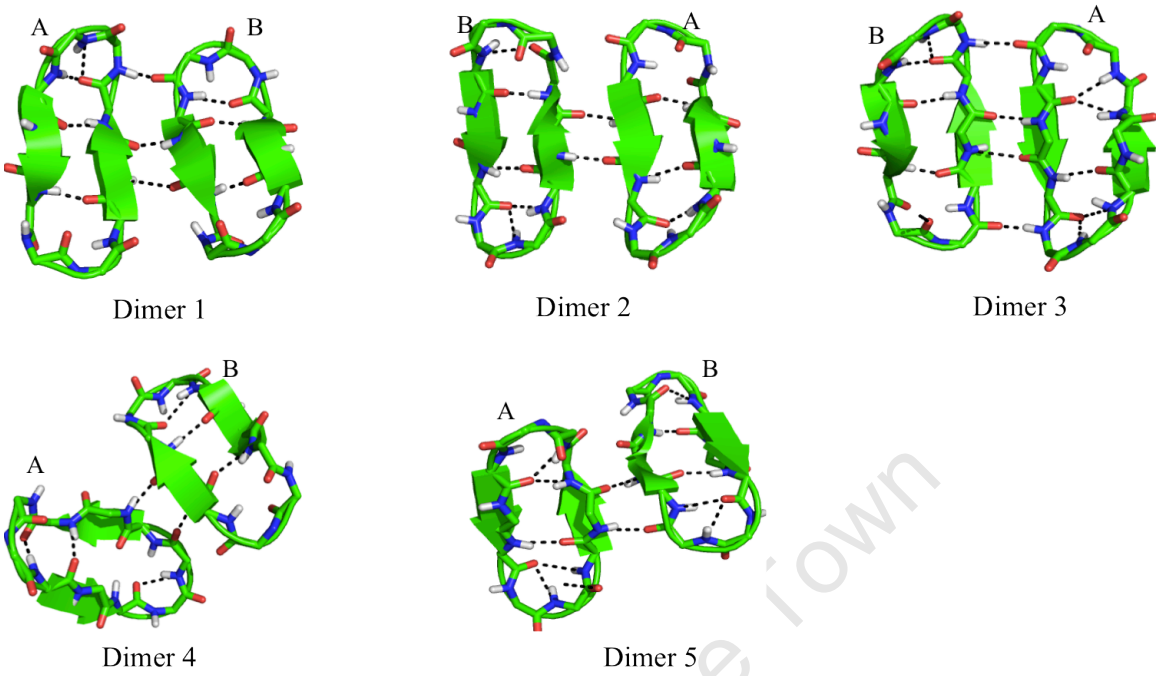

Figure 4.10: Backbone and secondary structure elements of the representative clusters of the dimer found from the 400 ns simulation. The similarity criterion of backbone RMSD ≤ 0.3 nm was used to cluster the dimers. The simulations were performed at 400 K.

4.3.3 Steered molecular dynamics

Classical molecular dynamics at 300 K produced dimers that were very dependent on the starting conformations. There was however a significant increase in the sampling of the conformational space of the dimer when the simulations were performed at a higher temperature. The first five possible dimers from the 400 K trajectories were subjected to center of mass pulling and umbrella sampling to determine the thermodynamic properties of the dimerization process.

One of the most useful applications of steered molecular dynamics is to provide qualitative insight into some biological processes such as protein-ligand and protein-protein binding and unbinding pathways.[22-24] In the current study, the COM pulling simulations focused on understanding the binding pathways of different TyrC dimers. No quantitative thermodynamic (ΔG) data about the unbinding process could be ascertained from the COM pulling simulations that were performed. This is because ΔG was path dependent and the interactions involved in the different dimers were different, hence only qualitative information could be obtained. For this reason umbrella sampling simulations were performed.

The overall shapes of the force-time graphs were similar for both pulling rates in all the five pulling simulations. The force gradually increased to a maximum, which corresponded to the maximum force needed to break the intermolecular backbone-backbone hydrogen bonds. The peptides stopped interacting when all the inter peptide hydrogen bonds were broken. In all the simulations the secondary structure of the pulled peptide was maintained. The unbinding pathways in all five dimers involved the breaking of the intermolecular peptide interactions. The peptides were completely dissociated after about 500 – 750 ps of pulling when a pulling rate of 0.001 nm/ps was used. The dissociation was quite fast when a 0.01 nm/ps pulling rate was used, and it occurred within the first 100 ps. Figure 4.11 shows the variation of force with time during the pulling simulations.

Dimer 3 required the largest maximum pulling force of 750 kJ/mol/nm at 170 ps during the 0.01 nm/ps pulling simulation (red in Figure 4.11). Dimer 2 required the second largest force. Dimer 1 and dimer 5 required the same maximum pulling force to unbind and dimer 4 seemed to be relatively easy to break.

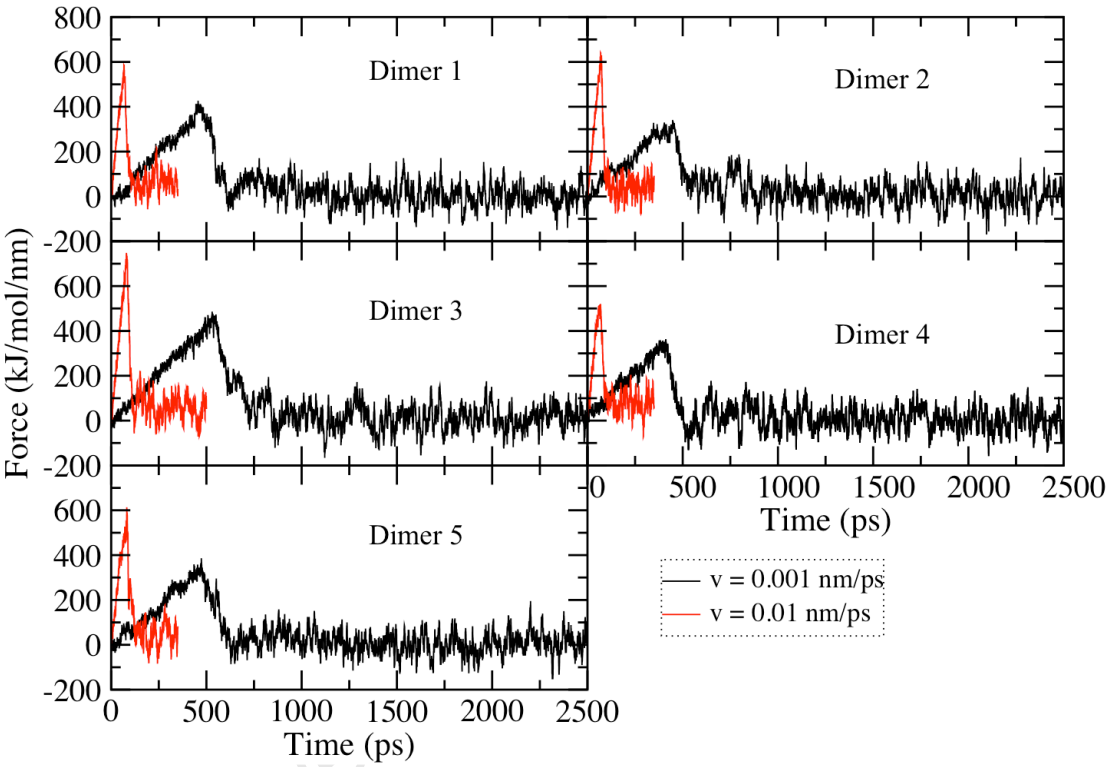

Figure 4.11: The variation of the pulling force with time for different dimers found in 300 K trajectories using two different pulling forces

Figure 4.12 shows the variation of the backbone-backbone hydrogen bonds for each dimer for the slower pulling rate. Dimer 1 is made up of three intermolecular backbone-backbone hydrogen bonds at the initial point of the pulling simulation. It reaches the maximum force after 531 ps and this corresponds to the time when the last backbone-backbone intermolecular hydrogen bond is broken. The hydrogen bond between $Trp^{4}NH$ and $Orn^{9}O$ is broken first followed by the middle hydrogen bond between $Trp^{4}O$ and

Orn^{9}NH. After the last backbone-backbone hydrogen bond is broken, the tyrosine side chain of peptide A begins to form intermittent hydrogen bonds with asparagine and glutamine side chains. As the simulation progressed, it began to interact with the backbone nitrogen atom of glutamine. During this time it also experiences some π-π interactions with tryptophan on peptide B. It completely dissociated after 500 ps.

Dimer 2 is made up of two intermolecular hydrogen bonds at the start of the simulation. During the first few picoseconds the backbone-backbone hydrogen bonds increase to three due to changes in the orientation of the monomers when the peptides were being pulled apart.

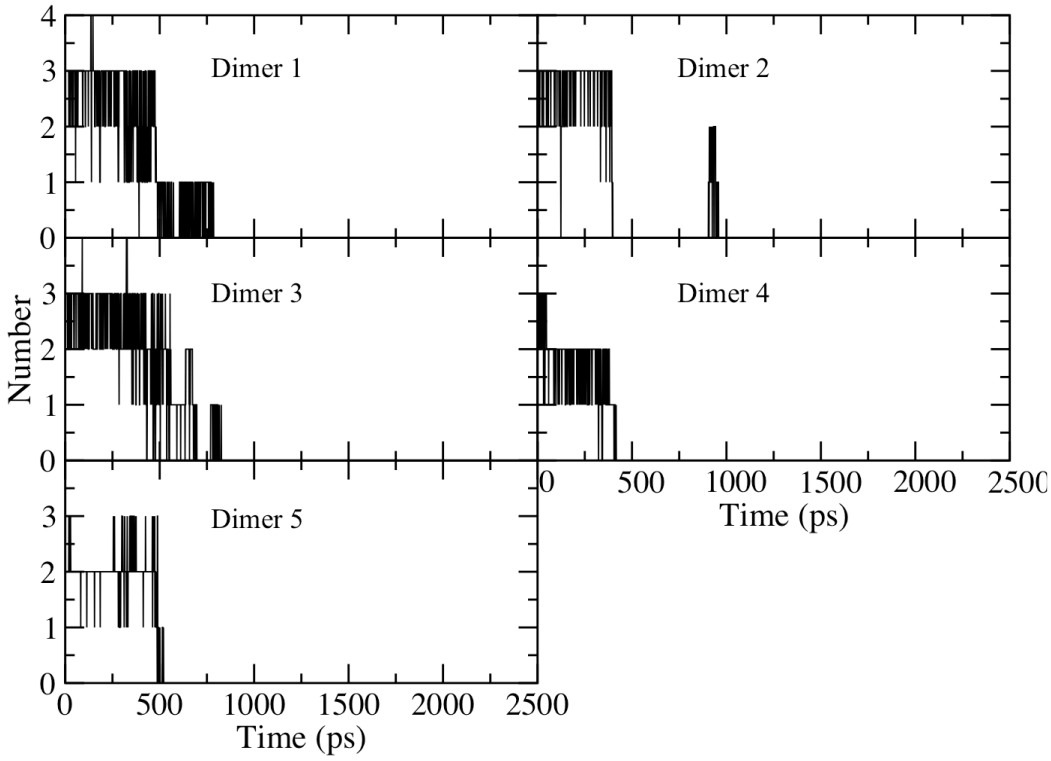

Figure 4.12: Backbone-backbone hydrogen bonds of dimers during the slower pulling simulation

All the backbone-backbone hydrogen bonds are broken simultaneously at 395 ps. The force-time graph shows the maximum peak at this point. When the pulling continues, the peptide forms very few intermittent hydrogen bonds with arginine from peptide A and it further orients itself such that it forms π-π interactions with tyrosine and it eventually dissociates completely after 700 ps.

Dimer 4 is made up of two backbone-backbone hydrogen bonds at the initial point and they quickly change to three when pulling began. The maximum force occured at the time that corresponded to the breaking of all the backbone-backbone hydrogen bonds.
At the beginning of the pulling simulation, dimer 5 has two backbone-backbone hydrogen bonds. The number of hydrogen bond changes to 3 after a very short time. It abruptly decreases and fluctuates between one and two until 250 ps. The hydrogen bonds increased again to 3 and continued to fluctuate between 2 and 3 until there were no hydrogen bonds after 510 ns. The maximum pulling force was generated at 510 ps, which corresponds to the breaking of the last backbone-backbone hydrogen bond.

It can be clearly seen from the steered molecular dynamics simulations that the force-time curves of the systems were very similar in all systems and the dissociation pathways seemed to depend on the backbone-backbone hydrogen bonding network.

4.3.4 Potential of mean force

The details of the free energy of dimerization of the five possible dimers of tyrocidine studied are shown on Table 4.1 and were obtained from the PMF profiles shown in Figure 4.13. The minimum energy in the five profiles occurred at a center of mass distance of 0.78 – 0.97 nm. Dimer 2 has the shortest center of mass separation of 0.79 nm, which suggests that the peptides were strongly bound together. This was confirmed by the fact that this dimer required the largest amount of free energy to dissociate. The free energies of dissociation of Dimer 1, Dimer 2 and Dimer 5 were very similar and had a value of about 33 kJ/mol. Dimer 3 and Dimer 4 were relatively weaker than the other dimers by about 6 kJ/mol. The low free energy of dissociation of dimer 3 can be attributed to the fact that the planes of the monomers were at an angle to each other and this affected the strength of the hydrogen bonds between them even though the inter-peptide distance was short. Dimer 1 and Dimer 2 had antiparallel beta-sheets and Dimer 5 had parallel beta-sheets between the two peptides. This indicates that there is no preferred dimer orientation in water.

Table 4: Binding free energies of the first five dimers

System	ΔG kJ/mol	Standard Deviation
Dimer 1	-32.8	± 0.6
Dimer 2	-33.3	± 1.2
Dimer 3	-27.0	± 0.6
Dimer 4	-27.5	± 0.8
Dimer 5	-32.8	± 0.8

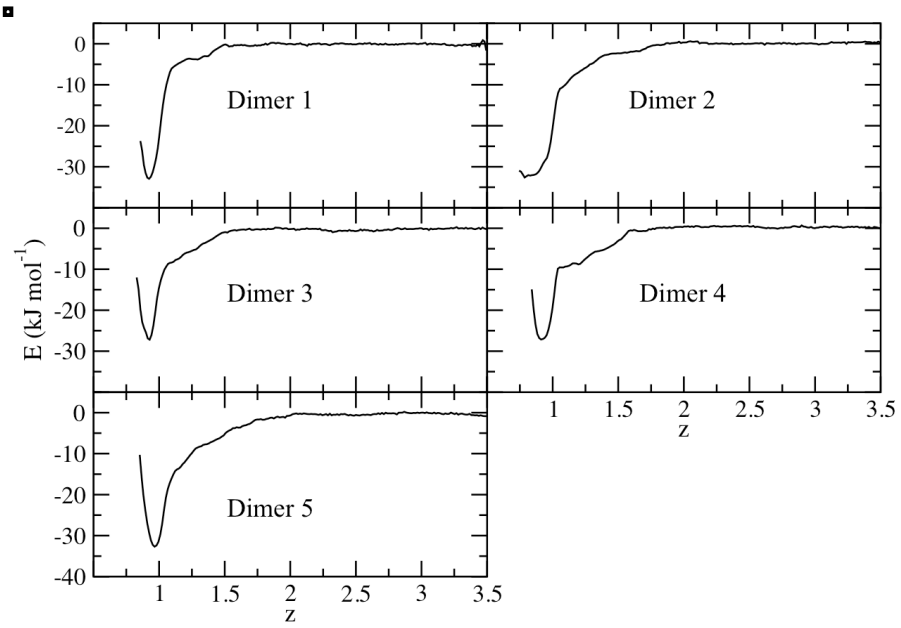

Figure 4.13: Potential of mean force for each of the five dimers obtained at 400 K

4.3.5 High order aggregation

Figure 4.14 shows the snapshots of the aggregation process of 12 peptides. The peptides form well-defined aggregates within the first 5 ns. These aggregates continue to grow and merge until there is 1 aggregate after 17 ns. The number of aggregates does not change until the end of the simulation. The aggregates formed do not show any higher form of organization like the formation of extended β-sheets within the simulated time. Visual inspection of the aggregation process showed that the rate of aggregation was slower in the systems containing four and six peptides.

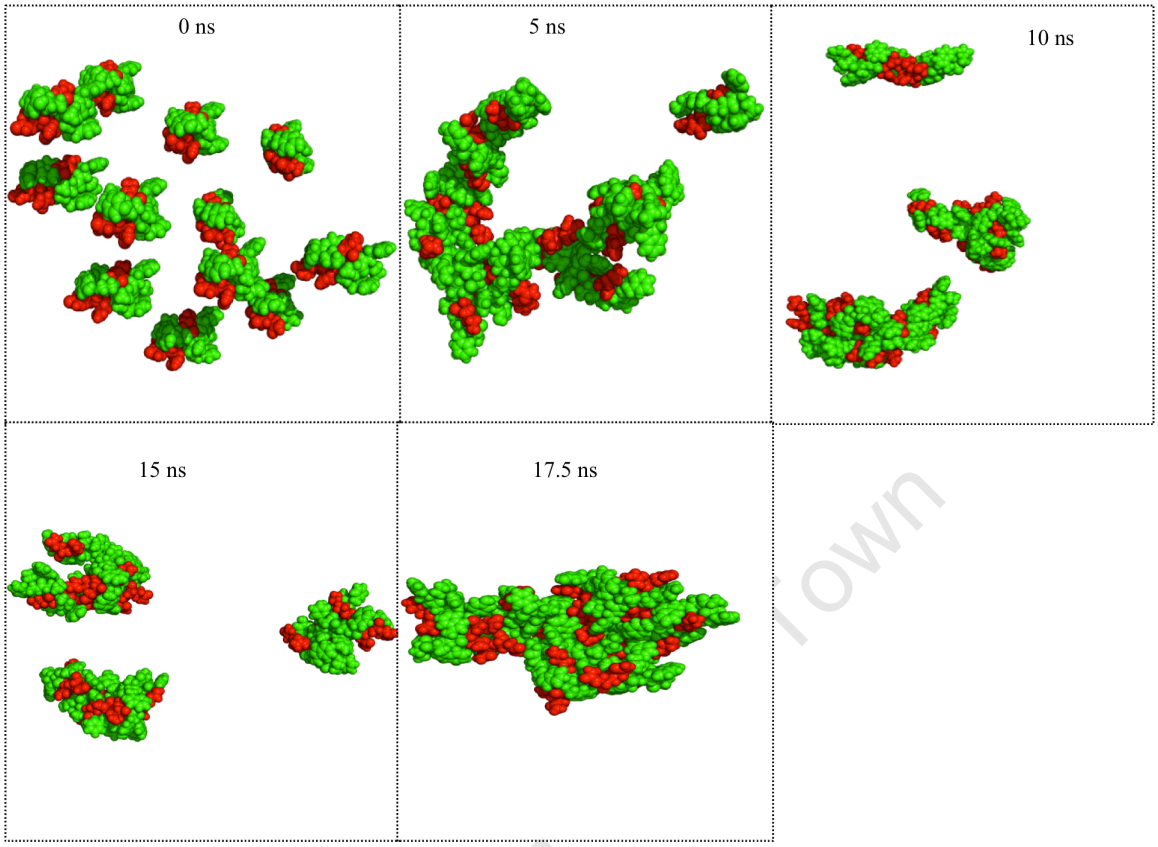

Figure 4.14: Time evolution of peptide aggregation of the system with 12 peptides. The system forms one aggregate in 17 ns. Atoms are shown as spheres, hydrophobic residues are colored green and hydrophilic residues are colored red.

To determine the state of aggregation, the distance between the centers of mass (COM) of each peptide was calculated for all possible pairs. When the distance between any pair of peptides was less than 1.2 nm the pair was considered to have aggregated. A peptide was considered to be part of an aggregate as long as any member of the aggregate was within 1.2 nm of the peptide in question.

The simulations show that the peptides rapidly aggregate with only one aggregate remaining after 7 ns, 10.5 ns and 15.5 ns for the six monomer, four monomer and twelve monomer systems respectively. Figure 4.15 shows that once the peptides are associated into one group, they never separate for the rest of the simulation.

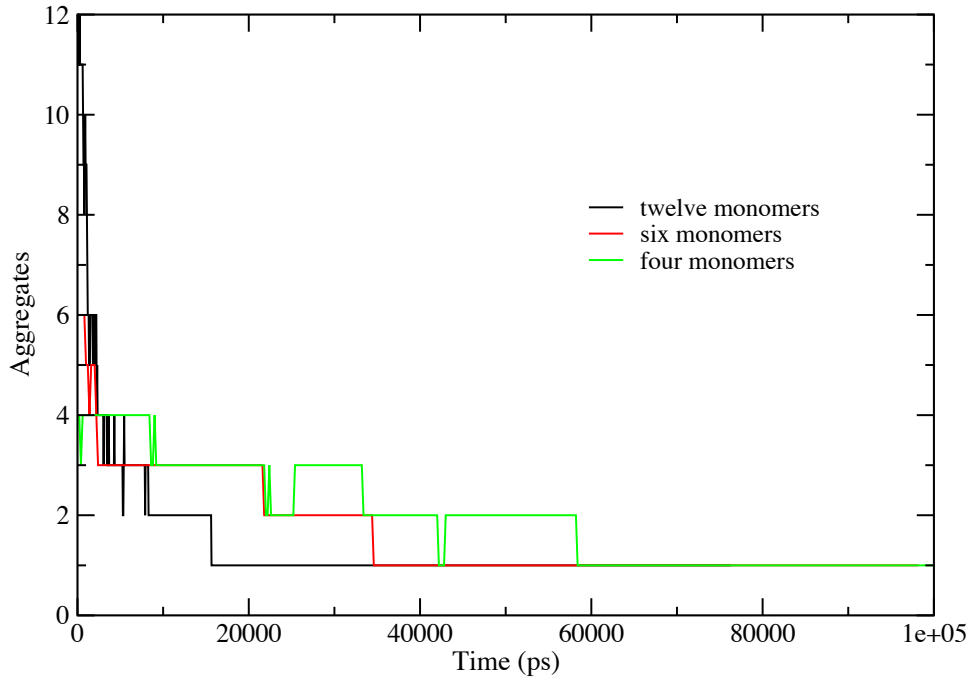

Figure 4.15: Variation of the number of aggregates with time. Two peptides were considered to be in the same cluster if the distance between their COM was < 1.2 nm

The variation of the solvent accessible area of the hydrophilic and hydrophobic residues in the simulations is shown in Figure 4.16. There was a decrease in the solvent accessible area of the hydrophobic surface, which correlates with the aggregation of the peptide. The change in hydrophilic surface is much less than that of the hydrophobic surface indicating some degree of orientation during the aggregation where the hydrophobic residues were being hidden from the solvent. This is consistent with what is known about protein folding.

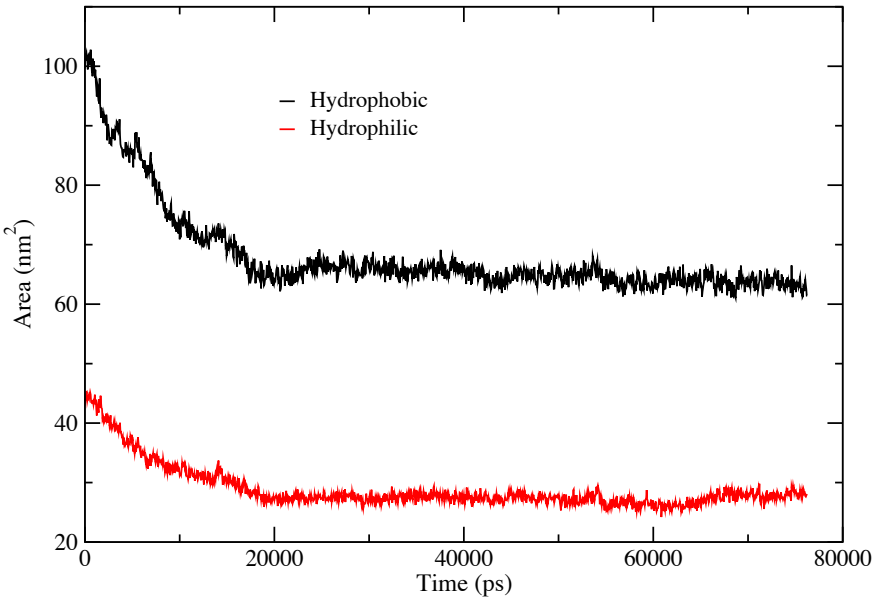

Figure 4.16*:* The variation of solvent accessible surface as a function of time of both hydrophobic and hydrophilic residues for a system with twelve peptides.

In order to characterize the packing of the peptides in the aggregate, the radius of gyration and the radial distribution functions were calculated. The radius of gyration gives a rough measure of the compactness of the aggregates formed by the peptides. Figure 4.17 shows the variation of the radius of gyration for the three systems under study. It was observed that the radius of gyration (Rg) varies in a similar fashion as the variation of the number of aggregates with time. The radius of gyration of the system of 12 monomers showed that during the simulation, the Rg varied significantly but gradually decreased until it reaches a minimum of 1.7 nm after 17 ns. This is also the same point when the system formed one aggregate. The value of the radius of gyration shows that the peptides were aggregating into a compact structure, as the radius of gyration was very low. The same observation was made for the systems with four and six

monomers, the radius of gyration decreased to a minimum, which indicates the formation of a compact structure.

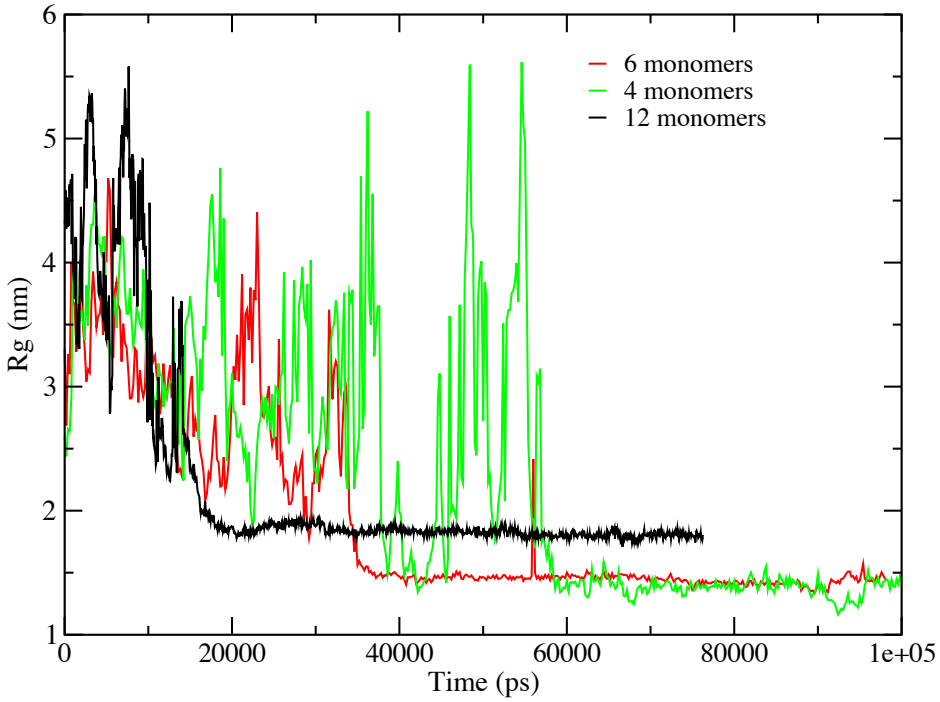

Figure 4.17: The time evolution of the radius of gyration (Rg) of peptides in systems containing four, six, and twelve monomers

The radial distribution function (RDF) of the peptides is shown in Figure 4.18. The maximum peak of the distribution occurs at 1.1 nm, which again shows that the peptides are closely packed together. The other systems also showed very similar RDFs with the first maximum peak at 1.1 nm.

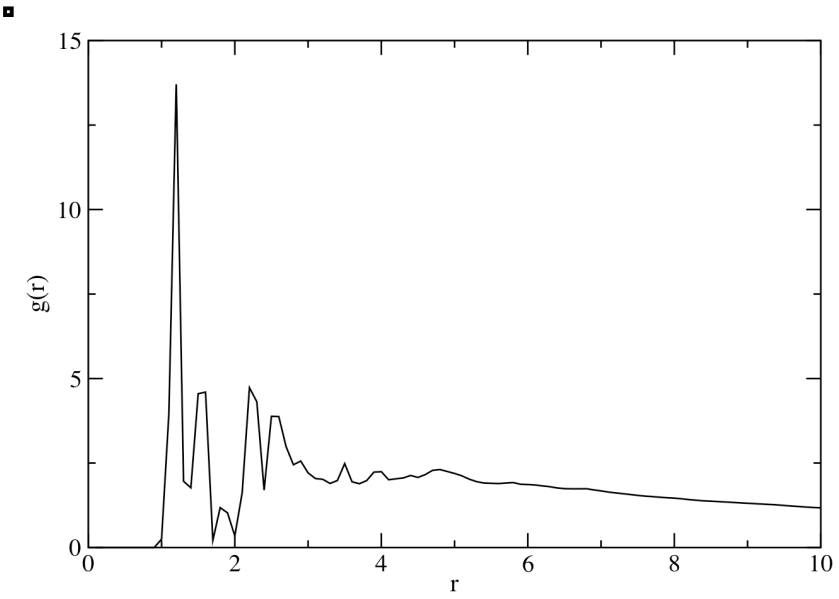

Figure 4.18: Radial distribution function for all peptide pairs for the system with twelve peptides.

Figure 4.19 shows the DOSY spectra of TyrC. The size of TyrC aggregate was calculated using DMF peak at 8.3 ppm as the reference as it is a more defined peak. Using this with a MM of 73, the aggregate size was found to be about 7 units. Equation 4.1 was used to calculate the size of the aggregate. The DOSY spectra also shows that there is hydrogen bonding between water and the TyrC aggregate as indicated by the spread of the peak from -8.4 to 9.45 m^2/s.

$$\frac{D_1}{D_2} = \sqrt[3]{\frac{M_2}{M_1}} \qquad 4.1$$

where D_1 and M_1, D_2 and M_2 represent the diffusion coefficients and the molar masses of the reference molecule and tyrocidine respectively.

The NMR results showed that TyrC forms small aggregates that are made up of about 7 units. This was contrary to what was obtained from MD simulations, which indicated that TyrC peptides could aggregate into very large aggregates with more than 7 monomers per aggregate. The differences in the aggregate formation between NMR and MD simulations can be explained by the differences in the concentrations of TyrC in the respective experiments. TyrC concentration used in the MD simulations is very high compared to that used in NMR experiments. It is expected that peptides would aggregate into single globular and unstructured aggregates at very high concentration.

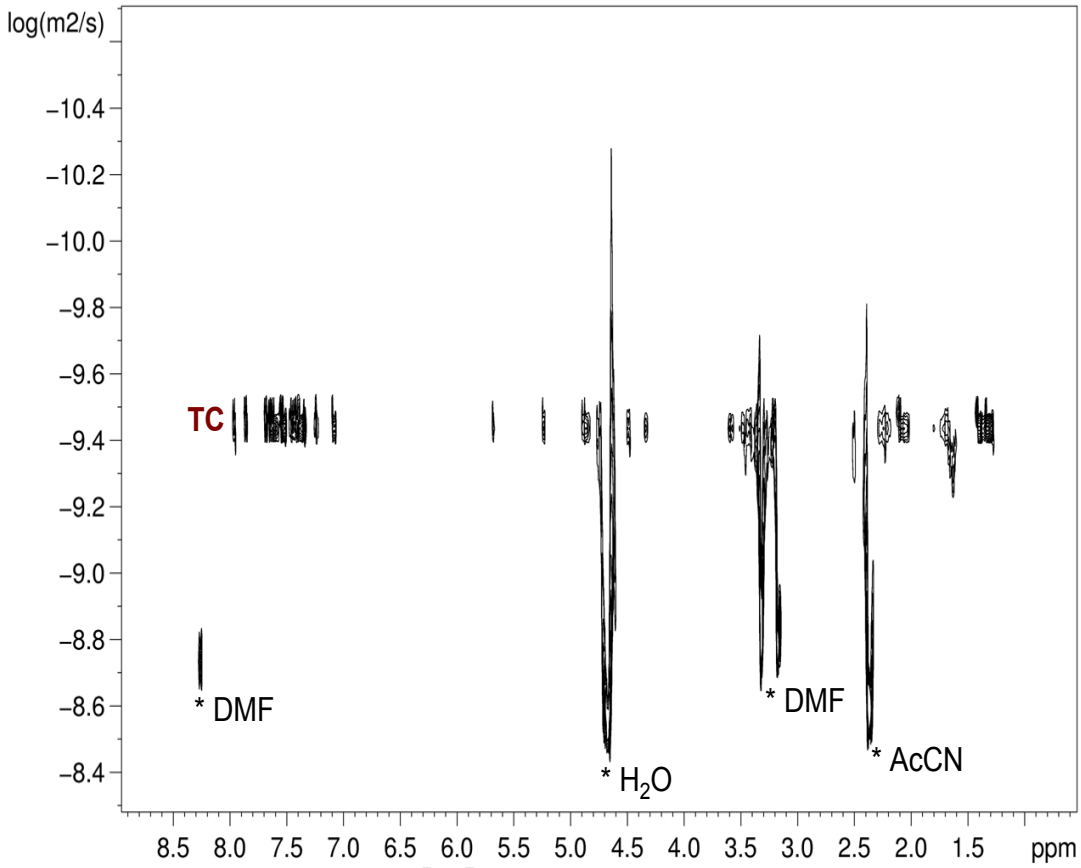

Figure 4.19: DOSY spectra on 1 mg tyrocidine C (TC) in 500 ml D_2O + AcCN-d3 + 1mM DMF

4.4 Conclusion

This study sought to understand the aggregation process of TyrC in water. This was investigated by looking at the dimerization process first. Classical molecular dynamics, steered molecular dynamics and umbrella sampling simulations were performed to determine the most favorable dimerization state, driving forces of dimerization and the possible dimerization pathways. The ability of tyrocidine to form oligomers was then studied using systems containing four, six and twelve peptides and the simulation data was compared to DOSY experimental data.

It was discovered that the conformational space accessible to tyrocidine dimers at 300K (the physiological temperature) is very small. This was because tyrocidine forms metastable dimers under these conditions and it would need very long simulations to access a representative conformational space. To overcome this problem, dimerization simulation were performed at 400 K. This resulted in an increase in the conformational space accessible to tyrocidine dimers. Monomers formed dimers by coming together in sideways orientation, suggesting that tyrocidines can form higher ordered structures though the addition of monomers on either side of the dimer.

The dimers of tyrocidine showed almost similar dissociation pathways as well as binding free energies, which led to the conclusion that there is no preferred dimerization state. This means that tyrocidine peptides can polymerize into high ordered β-sheets.

Systems with higher concentrations of the peptide showed that in water tyrocidine forms small aggregates, which eventually come together to form one large unstructured aggregate. This was in contrast to what was obtained from DOSY experiments, which indicated that TyrC forms aggregates made up of about 7 monomers in water. The formation of high ordered structures is expected to occur in big systems with low peptide concentrations and will definitely take much longer than the time simulated.

4.5 References

1. Ruttenberg MA, King TP, Craig LC. The chemistry of tyrocidine. VII. studies on association behavior and implications regarding conformation. Biochemistry 1966;5:2857-63.
2. Ruttenberg MA, King TP, Craig LC. The use of the tyrocidines for the study of conformation and aggregation behavior. Journal of the American Chemical Society 1965;87:4196-8.
3. Parente E, Giglio MA, Ricciardi A, Clementi F. The combined effect of nisin, leucocin F10, pH, NaCl and EDTA on the survival of listeria monocytogenes in broth. International Journal of Food Microbiology 1998;40:65-75.
4. Laiken SL, Printz MP, Craig LC. Studies on the mode of self-assembly of tyrocidine B. Biochemical and Biophysical Research Communications 1971;43:595-600.
5. Spathelf BM. Qualitative structure-activity relationships of the major tyrocidines, cyclic decapeptides from bacillus aneurinolyticus. Stellenbosch University; 2010.
6. Hancock REW, Chapple DS. Peptide antibiotics. Antimicrobial Agents and Chemotherapy 1999;43:1317-23.
7. Giuliani A, Pirri G, Nicoletto SF. Antimicrobial peptides: An overview of a promising class of therapeutics. Central European Journal of Biology 2007;2:1-33.
8. Bong DT, Clark TD, Granja JR, Ghadiri MR. Self-assembling organic nanotubes. Angewandte Chemie International Edition 2001;40:988-1011.
9. Ghadiri MR, Granja JR, Milligan RA, McRee DE, Khazanovich N. Self-assembling organic nanotubes based on a cyclic peptide architecture. Nature 1993;366:324-7.

10. Khuran E, Nielsen SO, Ensing B, Klein ML. Self-assembling cyclic peptides: Molecular dynamics studies of dimers in polar and nonpolar solvents. The Journal of Physical Chemistry B 2006;110:18965-72.

11. Tarek M, Maigret B, Chipot C. Molecular dynamics investigation of an oriented cyclic peptide nanotube in DMPC bilayers. Biophysical Journal 2003;85:2287-98.

12. Bolintineanu DS, Kaznessis YN. Computational studies of protegrin antimicrobial peptides: A review. Peptides 2011;32:188-201.

13. Yeaman MR, Yount NY. Mechanisms of antimicrobial peptide action and resistance. Pharmacological Reviews 2003;55:27-55.

14. Berendsen HJC, Van der Spoel D, Van Drunen R. GROMACS: A message-passing parallel molecular dynamics implementation. Computational Physics Communication 1995;91:43-56.

15. Jorgensen WL, Severence DL. Aromatic-aromatic interactions: Free energy profiles for the benzene dimer in water, chloroform, and liquid benzene. Journal of the American Chemical Society 1990;112:4768-74.

16. Berendsen HJC, Postma J, van Gunsteren WF, Hermans J. Interaction models for water in relation to protein hydration. Dordrecht: D. Reidel 1981.

17. Berendsen H, Postma J, DiNola A, Haak J. Molecular dynamics with coupling to an external water bath. The Journal of Chemical Physics 1984;81:3684-90.

18. Hess B, Bekker H, Berendsen HJC, Fraaije, J. G. E. M. LINCS: A linear constraint solver for molecular simulations. Journal of Computational Chemistry 1997;18:1463-72.

19. DiNola A, Berendsen HJC, Edholm O. Free energy determinations of polypeptides conformations generated by molecular dynamics. Macromolecules 1984;17:2044-50.

20. Hub JS, de Groot BL, van der Spoel D. g_wham - A free weighted histogram analysis implementation including roburst error and autocorrelation estimates. Journal of Chemical Theory and Computation 2010;6:3713-20.

21. Pieffet PG. The application of molecular dynamics techniques and free energy. 2005.

22. Izrailev S, Stepaniants S, Isralewitz B, Kosztin D, Lu H, Molnar F, Wriggers W, Schulten K. Steered molecular dynamics. Springer-Verlag: Berlin, 1998;4.

23. Isralewitz B, Gao M, Schulten K. Steered molecular dynamics and mechanical functions of proteins. Current Opinion in Structural Biology 2001;11:224-30.

24. Yang LJ, Zou J, Xie HZ, Li L, Wei YQ, Yang SY. Steered molecular dynamics simulations reveal the likelier dissociation pathway of imatinib from its targeting kinases c-kit and abl. PLoS One 2009;4:e8470.

Chapter 5

Study of peptide-lipid bilayer interactions

5.1 Introduction

Most antimicrobial peptides specifically kill bacteria, and are non-toxic to mammalian cells.[1] However, certain cationic antimicrobial peptides target both mammalian and bacterial cells.[2, 3] This is attributed to a number of peptide and membrane properties. The difference in the lipid composition of bacterial and mammalian cells has been postulated to be the main reason for antimicrobial peptides' specificity. Mammalian cells are made up of lipids such as (1-palmitoyl-2-oleoyl phosphatidylcholine) POPC or (1-palmitoyl-2-oleoyl phosphatidylethanolamine) POPE that are predominantly zwitterionic. Certain bacterial cells, on the other hand, are made up of a mixture of (1-palmitoyl-2-oleoyl phosphatidylglycerol) POPG and POPE lipids at a ratio of 1:3 respectively. Since POPG lipids are negatively charged, bacterial membranes are anionic in nature. Research has proposed that positively charged antimicrobial peptides prefer to bind negatively charged bacterial cells to largely zwitterionic mammalian cells.[4, 5] The positively charged antimicrobial peptides are electrostatically attracted to the negatively charged antimicrobial membrane surface.[6-10] When the peptides are close enough to the membrane surface, they attach themselves to the membrane. Peptides are then believed to self-aggregate on the surface of the membrane until they reach a threshold concentration.[11, 12] This is then followed by a number of different events depending on

the antibiotic mechanism of action. The transmembrane potential of bacterial membranes is also attributed to the specificity of antimicrobial peptides. The transmembrane potential of bacterial membranes is more negative than that of mammalian membranes, and this facilitates the insertion of positively charged antimicrobial peptides into the bacterial membranes.[1] On the other hand, the presence of cholesterol in mammalian cells protects them from attack by antimicrobial peptides.[1] Other peptide properties such as amphipathicity and hydrophobicity play major roles in the integration and permeation of peptides into the membrane.[13-15] High hydrophobic values are associated with mammalian membrane selectivity.[16]

Previous studies have shown that tyrocidine peptides have antimicrobial properties.[17-19] Despite their potential as antimicrobial agents, tyrocidine peptides have also been shown to cause lysis of mammalian cells. The lack of specificity of tyrocidine peptides has limited their use to topical applications.[20, 21] There is also a lack of understanding in their mechanism of action. Tyrocidine peptides are believed to disrupt the membrane structure by creating channels that allow ions and solutes to move across the membrane, causing cell lysis.

In this chapter, the effect of tyrocidine peptides on mammalian and bacterial membranes was studied. In order to do that, the study focused on understanding the initial interactions between tyrocidine peptides and the membrane structures. These initial interactions could cause the peptides to attach themselves to the membrane and trigger

membrane perturbation. Systems with various peptide:lipid ratios were studied to understand the effect of peptide concentration on the membrane structure.

5.2 Simulation methods

Several peptide-membrane systems with different peptide:lipid molar ratios were simulated using two different membrane model systems, POPE, and a mixture of POPG and POPE lipids at a molar ratio of 1:3 respectively. Table 5.1 below shows the summary of details of peptide-membrane systems.

The GROMACS software package was used to perform all the molecular dynamic simulations. For POPE membrane systems, Berger parameters[31] were used to describe the lipid force field. The protein-protein and protein-solvent interactions were described by the OPLS force field. GROMOS96 force field parameters[32] were used to describe the parameters of both the peptides and lipids in simulations that involved mixed membrane models of POPE:POPG. All simulations were performed at 298 K. The SPC model was used to describe water in all the simulations. The LINCS algorithm was also used to constrain all bonds. Non-bonded interactions (Lennard-Jones and Coulombic terms) were treated with a cut-off and a PME function respectively. Protein, lipid and solvent were coupled separately to an external temperature bath using a time constant of 0.5 ps using the Nose-Hoover method. The pressure was also weakly coupled using a semi-isotropic scheme to allow the membrane to deform in the *x-y* plane independently of the *z*-axis. A coupling constant of 2.0 ps and compressibility of 4.5×10^{-5} bar^{-1} with the reference pressure of 1 bar were used. All simulations were performed using periodic boundary conditions and a time step of 2 fs. The peptides were placed in the system in

such a way that that they were not fully inserted into the membrane at the beginning of the simulations. They were either partially inserted or in the water section of the membrane. This was done to determine how their positions in the membrane influenced their ability to permeabilize the membrane.

Table 5.1: Summary of all simulations performed for peptide-membrane systems

Peptide	Membrane Model	Peptide:Lipid Ratio	Water Molecules	Simulation Time	Counter Ions
TyrA	POPE	1:322	11380	80 ns	-
	POPE	4:322	11185	100 ns	-
	POPE	6:320	11051	100 ns	-
	POPE	9:322	10842	100 ns	-
	POPE	12:322	10664	100 ns	-
	POPE	20:320	10128	100 ns	-
	POPE:POPG	9:128	4100	100ns	32
TyrB	POPE	1:322	11396	100 ns	-
	POPE	4:322	11181	100 ns	-
	POPE	6:322	11051	100 ns	-
	POPE	9:322	10842	100 ns	-
	POPE	12:322	10653	100 ns	-
	POPE	20:319	10071	100 ns	-
	POPE:POPG	9:128	4119	100 ns	32
TyrC	POPE	1:320	6664	150 ns	-
	POPE	4:320	11071	100 ns	-
	POPE	6:321	11049	200 ns	-
	POPE	9:320	10855	100 ns	-
	POPE	12:320	10626	1500 ns	-
	POPE:POPG	9:128	4109	100 ns	32
	POPG	9:128	4000	100 ns	32

5.3 Results and Discussion

5.3.1 Peptide-membrane penetration

The penetration of individual peptides into the membrane was measured by determining the distance between the center of mass of the peptide and the center of mass of headgroup-phosphorous atoms on the closest bilayer leaflet. Figure 5.1 below shows that TyrA and TyrB were not able to penetrate the membrane. The centers of mass of both peptides were always above the center of mass of the phosphorus atoms. TyrC managed to insert into the membrane. After 50 ns, the center of mass of TyrC moved below the headgroups boundary inserting into the tails section of the membrane. Visual inspection showed that TyrC was already on the membrane interface at the beginning of the simulation (Figure 5.2). Figure 5.2 shows that TyrC was oriented in such a way that the hydrophilic residues were towards the water section at the beginning of the simulation. The hydrophobic residues of TyrC were towards the lipid tails section of the membrane. The residues Phe^{1}, Pro^{2} and Trp^{3} were the first ones to insert deeper into the membrane compared to all the other residues. This was consistent with previous experimental work, which suggested that Trp residues prefer to reside between the lipid tails and the lipid headgroups.[22-25] It was also expected that Phe and Pro would insert into the lipid tails first since they are hydrophobic. TyrA and TyrB did not have the same starting orientation as TyrC, and this may be the reason why they did not move into the membrane. These two peptides first had to re-orient themselves and establish favorable interactions with the membrane before they could penetrate the membrane.

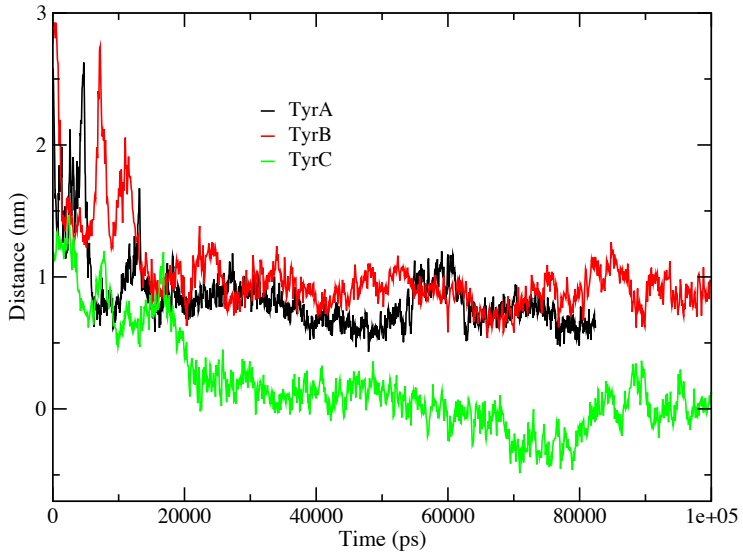

Figure 5.1: Distance between the center of mass of TyrA, TyrB and TyrC and phosphorus atoms in the closest bilayer leaflet

5.3.2 Peptide-membrane interaction

In order to have a better understanding of the binding mechanism of peptides on the membrane, contacts made between peptide residues and the lipid membrane were calculated. A residue was considered to be in contact with the membrane when the distance between the residue and the membrane was ≤ 0.4 nm. The number of contacts for each residue in the peptide was normalized by the total number of contacts with the membrane across all residues in the peptide giving the fraction of contacts between each residue and the membrane.[26]

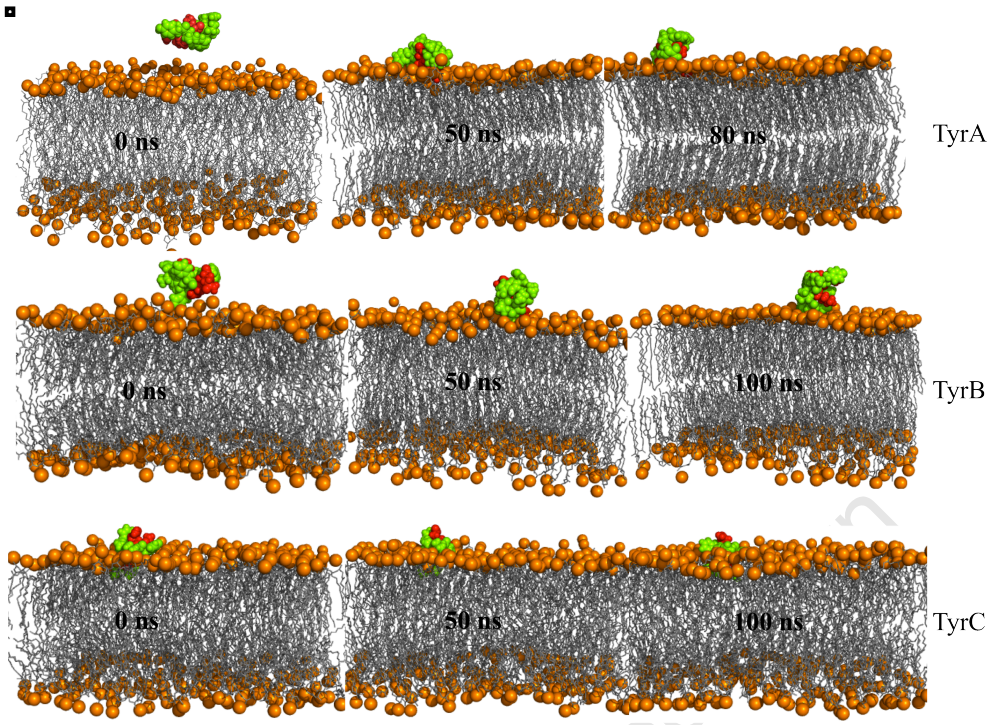

Figure 5.2: Snapshots of the progress of membrane simulations containing one tyrocidine peptide. The peptides are depicted as spheres, hydrophobic residues are represented as green spheres and hydrophilic residues are represented as red spheres. Orange spheres represent phosphorus atoms in the lipid headgroups.

Figure 5.3 shows the variation of the fraction of contacts against time for certain residues in TyrA, TyrB and TyrC during the simulation. Residues of TyrC showed low fraction of contacts because it had more residues in contact with the membrane at a time. The total number of fraction of contacts at any instance would add up to one if there were any residues in contact with the membrane. There were instances where most residues in TyrA and TyrB were not in contact with the membrane. At these instances, few residues that were in contact with the membrane would have very high fraction of contacts values. Overall, there was no consistent mechanism through which the peptides were interacting with the bilayer in TyrA and TyrB. The residues that were in contact with the membrane, and the fraction of contacts between the residues and the membrane constantly kept on

changing during the simulations as peptides were rotating at the membrane interface. These results indicated that these two peptides were probably searching for the correct orientation relative to the membrane.

The simulation of TyrC showed that residues Phe[1], Pro[2] and Trp[3] were in contact with the membrane at the early stages of the simulation. This was because of the orientation and the position of the peptide in the membrane at the beginning of the simulation. The contacts of Phe[1], Pro[2] and Trp[3] instantly began to decrease, at the same time, the contacts of Orn[9] and Tyr[7] began to increase. This suggests that there was a change in the orientation of the peptide. At around 110 ns, probably due to reorientation, the contacts of Orn[9] began to decrease, and those of Trp[3] and Tyr[7] continued to increase. Visual inspection showed that Trp[3] and Tyr[7] moved slightly into the membrane. The penetration of Trp[3] into the membrane is consistent with previous studies.[22-25]

5.3.3 Effect of peptide aggregation on membrane interaction

Simulations of different lipid:peptide ratios were conducted to determine the effect of aggregation on peptide-membrane interactions. Systems that had more peptides aggregating in the water section of the membrane had few peptide-lipid interactions. On the other hand, systems that showed less self-aggregation formed the largest number of aggregates and had more peptide-lipid interactions. The systems that had the largest number of aggregates in the respective peptide:membrane systems were 6:320, 9:320 and 12:320 for TyrA, TyrB and TyrC respectively.

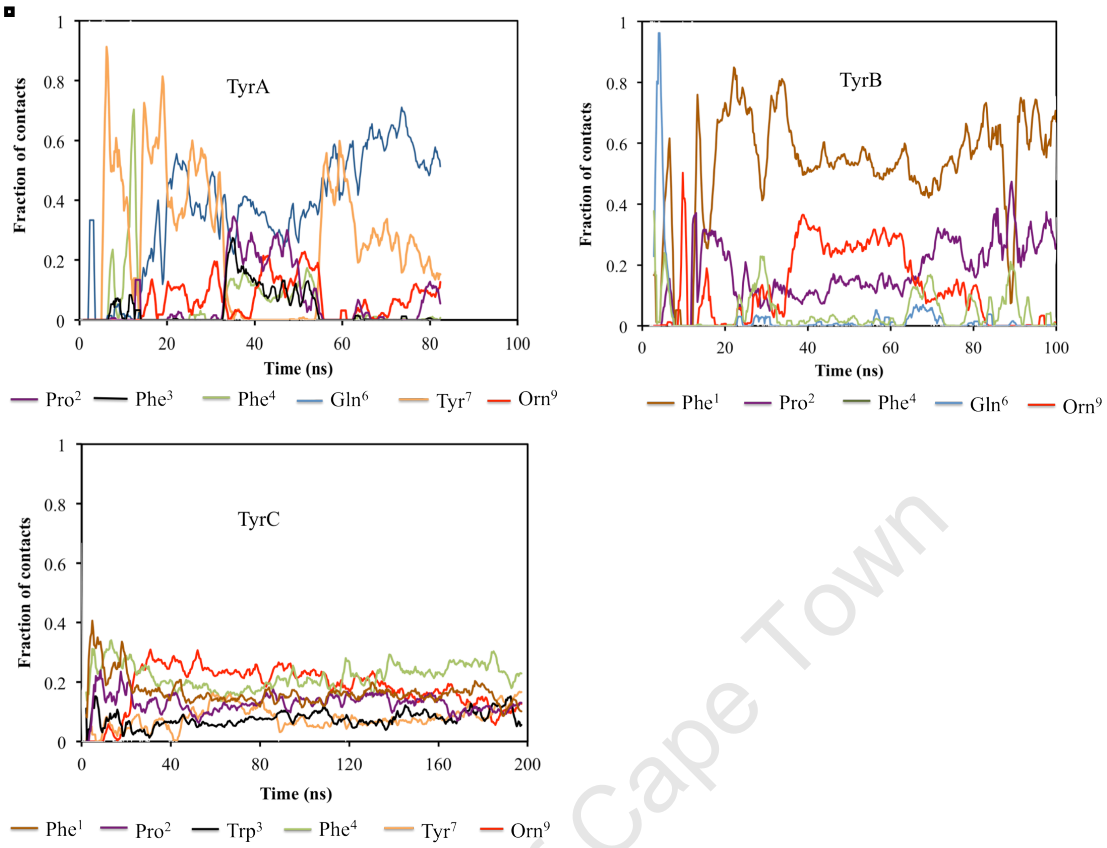

Figure 5.3: Fraction of contacts between peptide residues and the membrane. Only residues that made significant contacts with the membrane are shown

It is expected that peptides would self-aggregate more in systems that contain high peptide concentration, and less in low peptide concentration systems. From Figure 5.4, it can be seen that the aggregation of tyrocidine peptides was independent of concentration of peptides in the systems. Aggregation is likely to have been influenced by the initial orientation of the peptides at the beginning of the simulations.

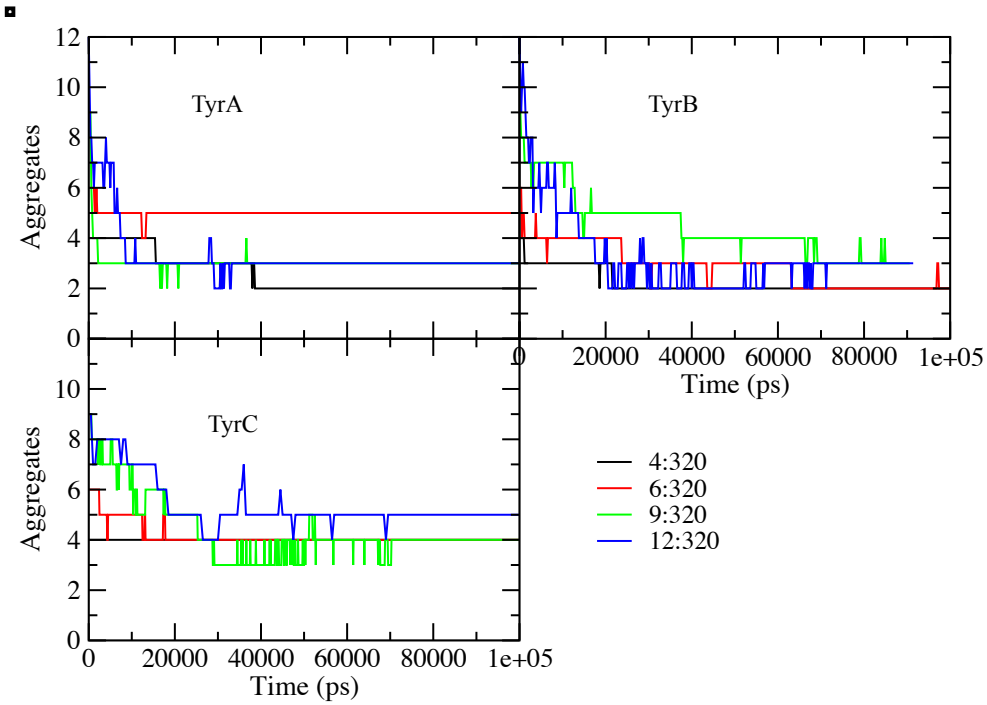

Figure 5.4: Aggregation of tyrocidine peptides in peptide:membrane systems.

The system of TyrC that contained 12:320 peptide:lipid concentration was simulated further to 1500 ns to get a clearer picture of the effect of peptides on the membrane. This system was chosen because, after 100 ns, there were many more aggregates compared to the other systems. Figure 5.5 shows the density distribution of different components of the system at different times during the simulation. TyrC peptides slowly diffused into the lipid with time. Within the first 500 ns, a large part of the peptides density was within the headgroups section. A substantial part of this peptide density moved into the tails section of the lipid membranes after 1000 ns. Figure 5.6 shows that the peptide density was predominantly found in the lipid headgroups and the tails section at the end of the simulation. There was little membrane thinning observed during the simulation. This could be because the peptide concentration was below the threshold concentration required for TyrC to perturb the membrane. TyrC peptides diffused to both membrane leaflets, as a result, fewer peptides were attached to one leaflet at a time.

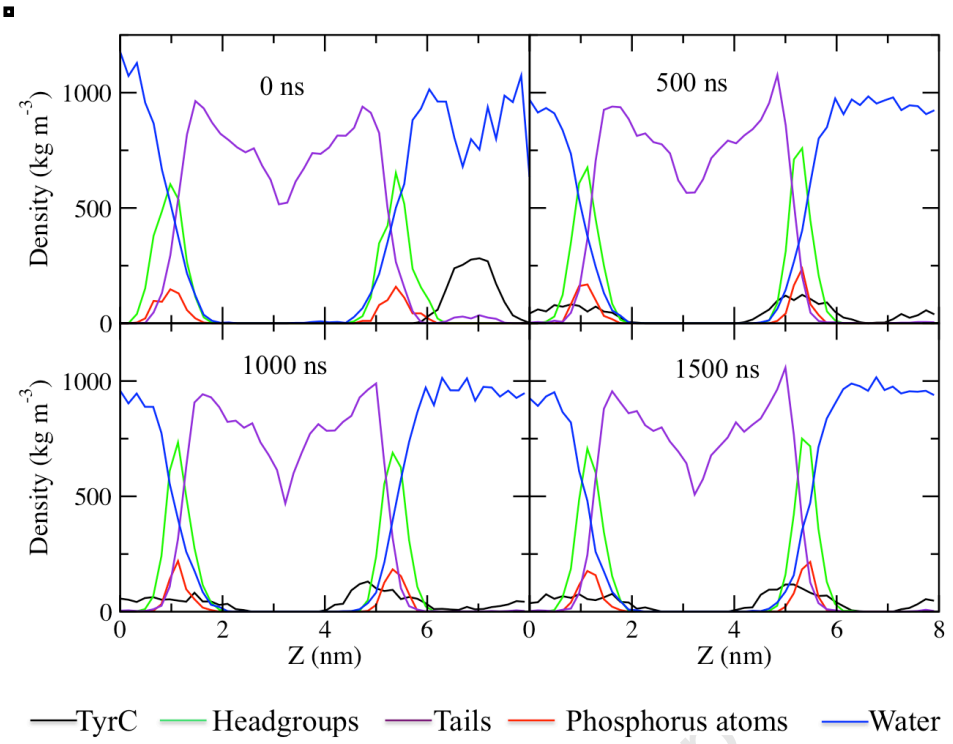

Figure 5.5: Density profiles of TyrC and different membrane components at different times during the simulation.

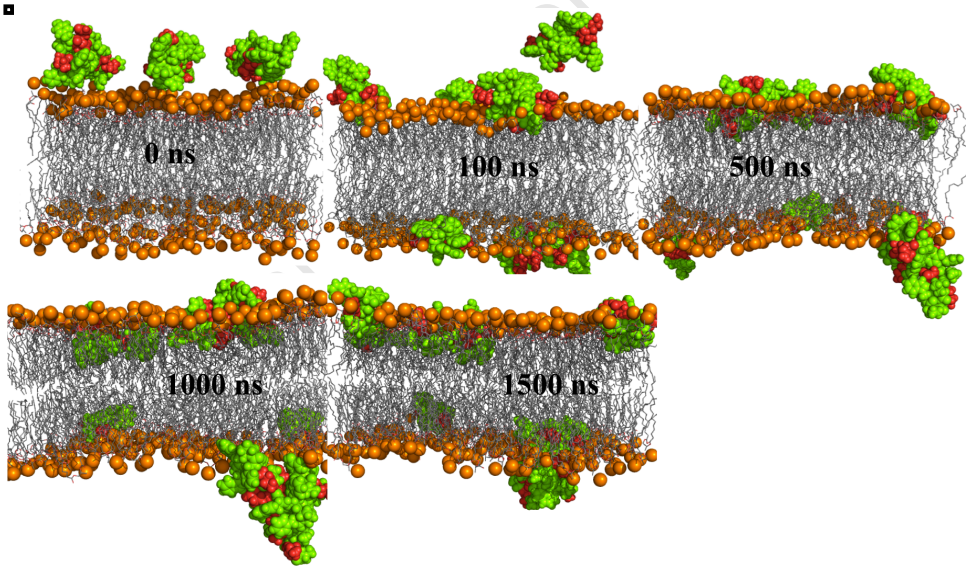

Figure 5.6: Snapshots of the progress of the simulations containing 12 TyrC peptides in a membrane. The peptide atoms are depicted as spheres, hydrophobic residues are shown in green and hydrophilic residues are coloured red. Orange spheres represent phosphorus atoms in the lipid headgroups.

The extent of membrane perturbation was further analysed by calculating the deuterium order parameters, $S_{CD,}$ for carbons in the lipid tails. The deuterium order parameter is defined by the following equation

$$S_{CD} = \frac{1}{2}\langle 3\cos^2\theta - 1\rangle \quad (5.1)$$

where θ is the angle between the bilayer normal and the vector of atoms $C_i - 1$ to $C_i + 1$, C_i is a carbon atom in the lipid chain, and the brackets denote an average over time and all lipids. The order parameter of each carbon atom in the lipid tail is calculated separately. The order parameter is 0 if the vector is randomly oriented (highly disordered), ½ if it is perpendicular to the bilayer normal and 1 if it is parallel to the bilayer normal (highly ordered). However, it should be noted that the orientation where the lipid chain is in a fixed orientation perpendicular to the bilayer normal makes no physical sense for a membrane. S_{CD} goes smoothly from 1 through ½ to zero as the disorder in the averaged chain position increases. The lipid tails have two acyl chains denoted as sn1 and sn2. There are 16 carbon atoms in the acyl chains for which only 14 order parameters can be calculated. The carbonyl and terminal methyl carbons are not included in the calculations. For the purpose of this thesis, the carbon atoms in sn2 were considered.

Figure 5.7 shows the order parameters of the sn2 chains from the system of TyrC that contained 12:320 peptide:lipid concentration. The order parameters were calculated for three different time segments during the simulation. This was done in order to have a clear picture of how the lipid membrane structure was changing with time. The general shape of the profiles is consistent with experimental results for other lipids [27-29]. The order parameters form a plateau close to the top of the chain and showed a gradual decrease towards the bottom of the chain. There was an increase in the order parameters of the lipid chains after the 0 ns – 500 ns time segemnt, indicating an increase in the orderliness of the lipids as the simulations progressed. There was no significant difference between the order parameters of the lipids during the 500 ns - 1000 ns and 1000 ns - 1500 ns time segments. The results showed a decrease in the proportion in which the order parameters were increasing as one moves towards the bottom of the chain after 0 ns - 500 ns time segment. The carbon atoms close to the headgroups showed the largest increase and those close to the bilayer center showed insignificant changes. The order parameters of carbon atoms 13 and 14 were very similar for all the three time segments. It would be expected that when peptides interact with the lipids they perturb the membrane thereby decreasing order of the lipids. However, a slight opposite effect was noted. This is likely to be a result of close packing of the lipids as peptides diffuse into the membrane. This caused the lipids to align with each other more, thereby increasing the order parameters.[30] The small change in the bilayer thickness from ~4.200 nm to ~4.167 nm during the whole simulation confirmed the close packing of the lipids.

5.3.4 Effect of tyrocidine peptides on putative bacterial membranes

Three systems made up of putative anionic bacterial membranes were simulated. The membrane systems were made up of lipids at a ratio of 3:1 POPE to POPG respectively. Each system had 128 lipid and 9 peptide molecules.

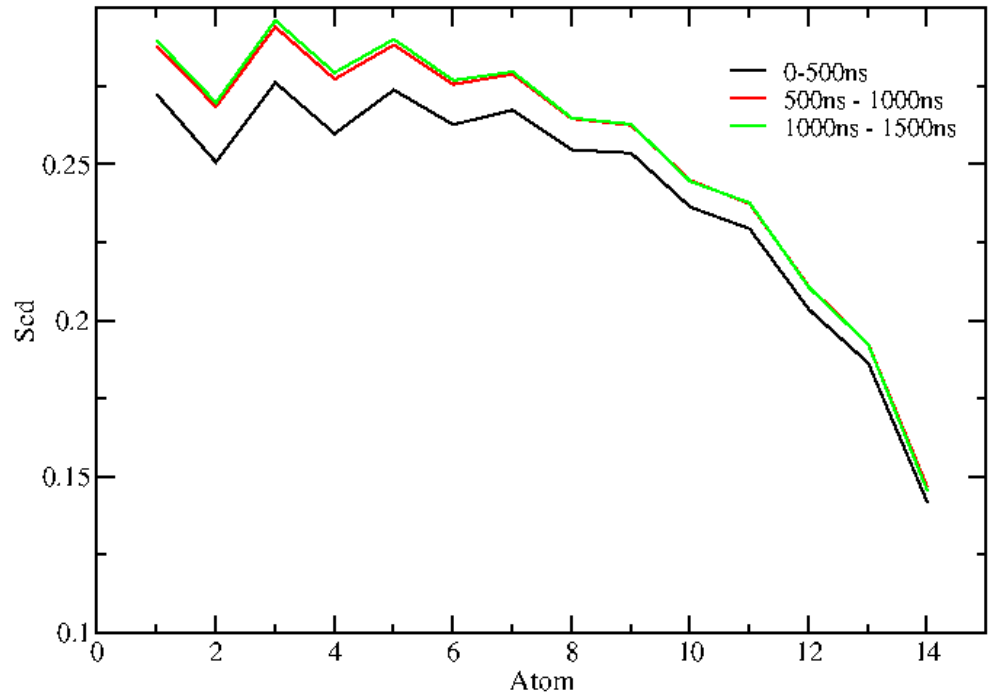

Figure 5.7: Order parameters of sn2 chain of lipid tails at different time zones during the 12:322 TyrC simulation. Atom numbers increase from head to tail.

Figure 5.8 shows the details of the variation of fraction of contacts between peptides and different components of the membrane. The contacts between the peptides and water decreased as the simulations progressed, on the contrary, contacts between the peptides and the lipids increased with time. This indicates that the peptides were moving closer to the lipid interface. The general pattern of contacts between peptides and the membrane components was the same in all three systems. The contacts between the peptides and

POPE and POPG were consistent with the ratio of POPG:POPE in the membrane systems. TyrA showed more contacts between the peptides and the membrane compared to TyrB and TyrC. TyrB had the least number of contacts between the peptides and the membrane, however, they were not remarkably different from those of TyrC.

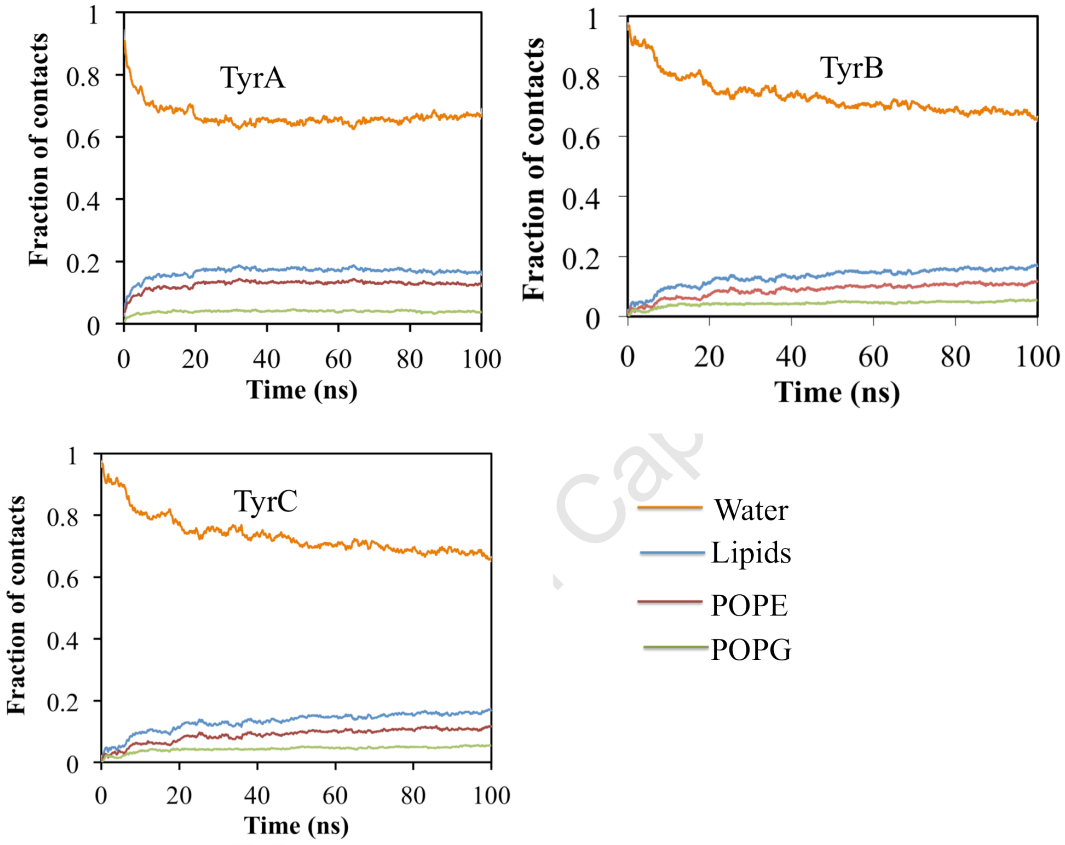

Figure 5.8: Variation of the fraction of contacts between peptides and different components of the membranes

TyrB had fewer peptides-membrane contacts compared to the other peptides because it self-aggregated more in the water section of the system. TyrB peptides also diffused to both membrane leaflets. Figure 5.9 shows that TyrA and TyrC peptides distorted the membrane surfaces and some hydrophobic residues penetrated the membrane. In both

cases, hydrophobic residues inserted deeper into the membrane compared to hydrophilic residues.

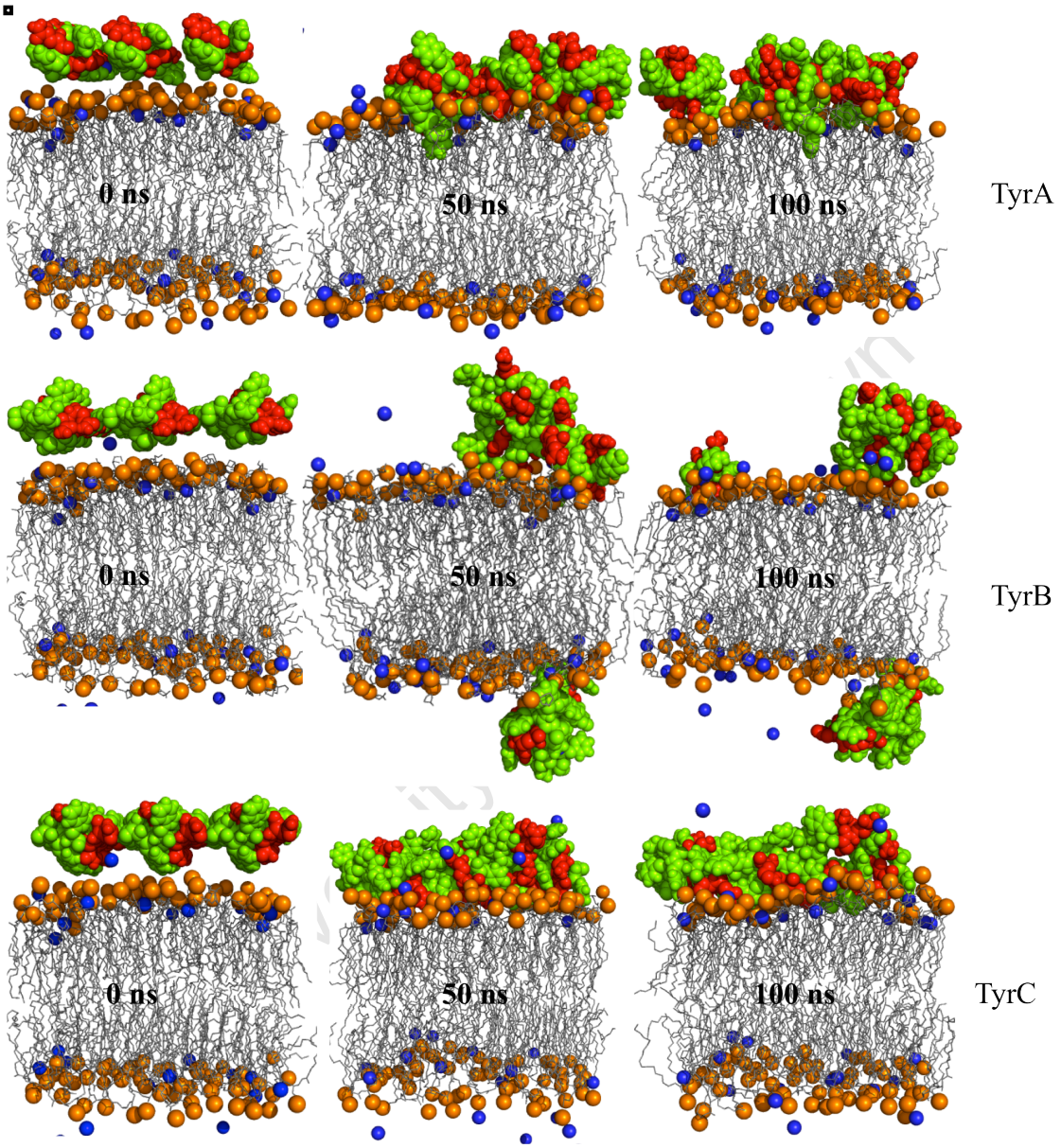

Figure 5.9: Snapshots of the progress of mixed membrane simulations. The peptide atoms are depicted as spheres, hydrophobic residues are colored in green and hydrophilic residues are colored in red. Orange spheres represent phosphorus atoms in the lipid headgroups. Sodium ions are depicted as blue spheres. The snapshots were taken at 0 ns, 50 ns and 100 ns.

In order to determine the effect of the peptides on the membrane structure, the order parameters of the lipids were calculated for different time segments during the

simulations. Three different time segments of the simulation were considered, that is, the beginning of the simulation (0 – 10 ns), the middle of the simulation (40 - 50 ns) and towards the end of the simulation (90 – 100 ns). Figure 5.10 shows the order parameters that were calculated for the mixed membranes.

The order parameters of POPE lipids were significantly larger than those of POPG peptides. However, they both showed a plateau near the top of the chain and a gradual decrease towards the bottom of the chain, which is expected for most lipids.[27-29] The largest values of the order parameters for POPE lipids were around 0.32, whereas POPG lipids had their largest values around 0.20. The largest order parameters were recorded for carbon atom 6 in all systems. POPE lipids showed small order parameter changes for different time segments while POPG showed relatively large changes. In TyrA simulation, the order parameters of POPE lipids increased between 90 – 100 ns for the part of the lipid that was closer to the headgroups and decreased for the lipid tails. The changes in the order parameters of the system that contained TyrC were very similar to the ones of the system that had TyrA during the 90 -100 ns simulation time segment. The increase in the order parameters at the top of the chain was probably because lipids were aligning with each other as the peptides were penetrating the membrane.[30] The order parameters of lipids in TyrB simulation showed a small decrease as the simulation progressed.

There were significant variations in the order parameters of POPG lipids between the time segments for all three simulations. The maximum values of order parameters of POPG lipids varied from 0.2 to 0.25. In TyrA simulations, the order parameters increased during the second time segment (40-50ns) and slightly decreased during the (90-100ns) time segment but were still higher that those of the first time segment. This was also observed in the TyrC simulation. In TyrB simulations, the order parameters of lipids decreased during the (40-50ns) time segment before returning to their initial values towards the end of the simulation. Peptides seemed to have the same effects on both POPE and POPG lipids, however, the effects were more prominent on POPG lipids. There was very little overall effect of the peptides on the lipids in the system that contained TyrB.

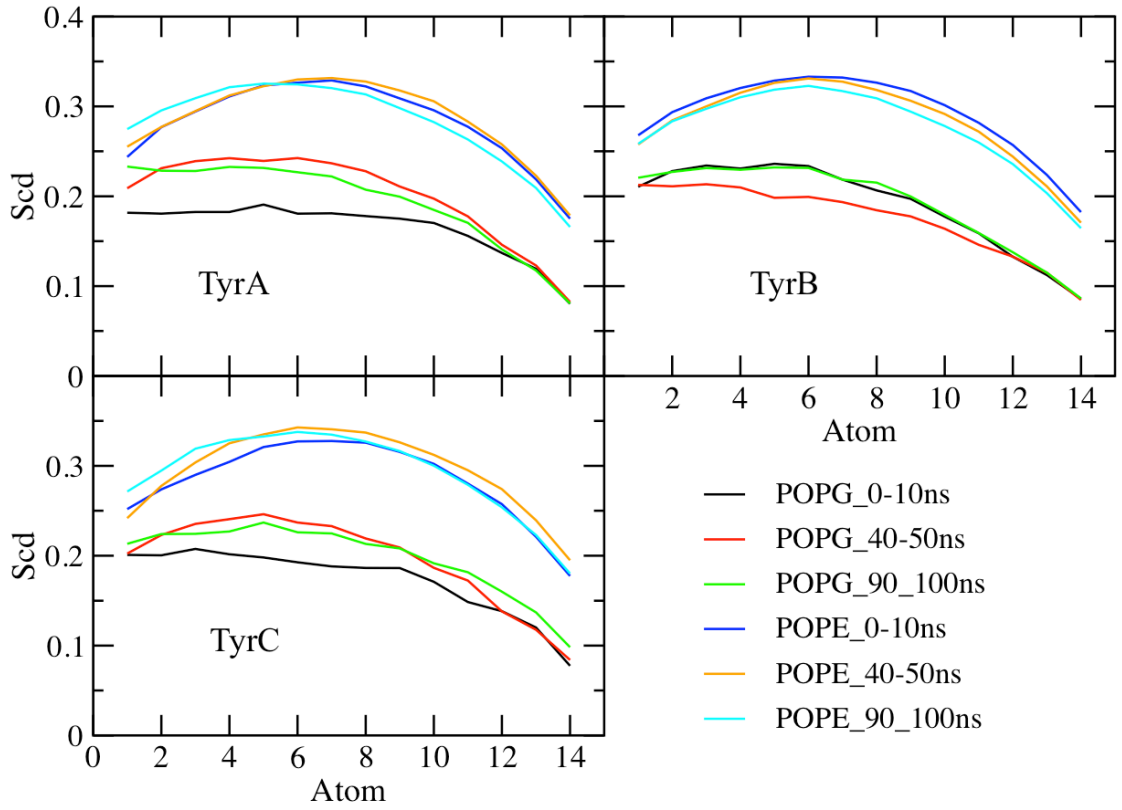

Figure 5.10: Order parameters of sn2 chain of lipid tails at different time zones during the mixed membrane simulations. Atom numbers increase from head to tail.

A comparison of the effect of tyrocidine peptides on both membrane types was considered. Figure 5.6 and Figure 5.9 show the snapshots of the systems as the simulations were progressing. Upon looking at the 100 ns snapshots, the general observation was that peptides were diffusing into both, putative microbial membranes and POPE membranes at almost the same rate. This was quite evident in simulations of TyrA and TyrC in mixed membranes as well as the simulation of POPE membrane. It could be seen that there was little membrane surface disruption by TyrB in the mixed membrane simulation. This is likely to have been caused by self-aggregation of TyrB peptides in the water section of the membrane. TyrB peptides formed one large aggregate, and this limited their ability to perturb the membrane. These results are

consistent with previous experimental work, which indicated that tyrocidine peptides are not specific.[17-21] From the results, the peptides could diffuse into the membrane and form aggregates that traverse the membrane thereby forming channels that destroy the cell.

Tyrocidine peptides have a charge of +1, which is relatively small compared to the charges between +2 and 5 that have been shown to influence antimicrobial activity of cationic peptides.[1] Visual inspection showed that tyrocidine peptides did not assume any preferred orientation when they were approaching the bacterial membrane surface. This was because tyrocidine peptides have an exceptionally small charge and at the same time are highly hydrophobic. This could have resulted in weaker electrostatic interactions between the peptides and the membrane compared to the hydrophobic interactions. The interactions between the peptides and the membrane were therefore driven by hydrophobic interactions.

5.4 Conclusion

The objective of this study was to investigate the effect of tyrocidine antibiotics on mammalian and bacterial membranes. To this end POPE was used as a model mammalian membrane while a mixed system of POPE and POPG were used as a model for a bacterial membrane. There was very little difference in the manner in which tyrocidine peptides interacted with both membrane structures. This indicated that tyrocidine peptides could perturb both mammalian and bacterial cells using the same mechanism. This confirms previous experimental results that tyrocidine peptides are non-selective.

The simulations of single tyrocidine peptides indicated that TyrA and TyrB were diffusing on the membrane surface. It was therefore not possible to identify if there are any specific residues that could be involved in the initial peptide-membrane interactions. TyrC peptide inserted much deeper into the membrane starting with tryptophan residues, indicating the hydrophobicity of tyrocidine peptides plays a significant role in membrane perturbation.

The results also indicated that aggregation of tyrocidine peptides in the water section of the membrane reduces their ability to interact with the membrane. This was a general observation in all the systems containing different membrane types.

5.5 References

1. Yount NY, Yeaman MR. Immunocontinuum; perspectives in antimicrobial peptide mechanisms of action and resistance. Protein & Peptide Letters 2005;12:49-67.
2. Shai Y. Mechanism of membrane permetion and pore formation by antimicrobial peptides. In: L. K. Tamm, editor. Protein-lipid interactions. Weinheim, Germany: Wiley-VCH; 2005.
3. Bechinger B. The structure, dynamics and orientation of antimicrobial peptides in membranes by multidimensional NMR spectoscopy. Biochemica Et Biophysical Acta 1999;1462:157-84.
4. Dolis D, Moreau C, Zachowski C, and Devaux PF. Aminophospholipid translocase and proteins involved in transmembrane phospholipid traffic. Biophysical Chemistry 1997;68:221-31.
5. Devaux PF. Static and dynamic asymmetry in cell membranes. Biochemistry 1991;30:1163-73.
6. Bessalle R, Haas H, Goria A, Shalit I, Fridkin. M. Augmentation of the antibacterial activity of magainin by positive-charge chain extension. Antimicrobial Agents and Chemotherapy 1992;36:313-7.
7. Vaz Gomes A, de Waal A, Berden JA, Westerhoff HV. Electric potentiation, cooperativity and synergism of magainin peptides in protein-free liposomes. Biochemistry 1993;32:5365-72.
8. Matsuzaki K, Sugishita K, Harada M, Fujii N, Miyajima K. Interactions of an antimicrobial peptide, magainin 2, with outer and inner membranes of gram-negative

bacteria. Biochimica Et Biophysica Acta (BBA) - Biomembranes 1997 7/5;1327:119-30.

9. Matsuzaki K, Yoneyama S, Fujii N, Miyajima K, Yamada K, Kirino Y, Anzai K. Membrane permeabilization mechanisms of a cyclic antimicrobial peptide, tachyplesin I, and its linear analog. Biochemistry 1997;36:9799-806.
10. Dathe M, Nikolenko H, Meyer J, Beyermann M, Bienert M. Optimization of the antimicrobial activity of magainin peptides by modification of charge. FEBS Letters 2001;501:146-50.
11. Ludtke JS, He K, Wu Y, Huang HW. Cooperative membrane insertion of magainin correlated with its cytolytic activity Biochemica Et Biophysical Acta-Biomembranes 1994;1190:181-4.
12. Ludtke JS, He K, Heller WT, Harroun TA, Yang L, Huang HW. Membrane pores induced by magainin. Biochemistry 1996;35:13723-8.
13. Shai Y. Mechanism of the binding, insertion and destabilization of phospholipid bilayer membranes by alpha-helical antimicrobial and cell non-selective membrane-lytic peptides. Biochemica Et Biophysical Acta-Biomembranes 1999;1462:55-70.
14. Shai Y. Mode of action of membrane active antimicrobial peptides. Biopolymers 2002;66:236-48.
15. Shai Y. From innate immunity to de-novo designed antimicrobial peptides. Current Pharmaceutica Design 2002;9:715-25.
16. Matsuzaki K, Sugishita K, Fujii N, Miyajima K. Molecular basis for membrane selectivity of an antimicrobial peptide, magainin 2. Biochemistry 1995;34:3423-9.

17. Dubos RJ, Hotchkiss RD. The production of bactericidal substances by aerobic sporulating bacilli. Journal of Experimental Medicine 1941;73:629-40.

18. Hotchkiss RD, Dubos RJ. Bactericidal fractions from an aerobic sporulating bacillus. Journal of Biological Chemistry 1940;136:803-4.

19. Hotchkiss RD. Gramicidin, tyrocidine and tyrothricin. In: F. F. Nord, C. H. Werkman, editors. Advances in enzymology and related areas of molecular biology. ; 1944.

20. Van Epps HL. René dubos: Unearthing antibiotics. The Journal of Experimental Medicine 2006;203:259

21. Rammelkamp CH, Weistein L. Toxic effects of tyrothricin, gramicidin and tyrocidine. The Journal of Infectious Diseases 1942;71:166-73.

22. de Planque MRR, Kruijtzer JAW, Liskamp RMJ, Marsh D, Greathouse DV, Koeppe II RE, de Kruijff B, Killian AJ. Different membrane anchoring positions of tryptophan and lysine in synthetic transmembrane α -helical peptide. Journal of Biological Chemistry 1999;274:20839-46.

23. Yau WM, Wimley WC, Gawrisch K, White SH. The preference of tryptophan for membrane interfaces. Biochemistry 1998;37:14713-8.

24. Grossfield A, Woolf T. Interaction of tryptophan analogs with POPC lipid bilayers investigated by molecular dynamics calculations. Langmuir 2002;18:198-210.

25. Norman KE, Nymeyer H. Indole localization in lipid membranes revealed by molecular simulation. Biophysical Journal 2006;91:2046-54.

26. Romo TD, Bradney LA, Greathouse DV, Grossfield A. Membrane binding of an acyl-lactoferricin B antimicrobial peptide from solid-state NMR experiments and

molecular dynamics simulations. Biochemica Et Biophysical Acta 2011;1808:2019-30.

27. Seelig J, and Seelig A. Lipid conformation in model membranes andbiological membranes. Quarterly Reviews of Biophysics 1980;13:19-61.

28. Seelig A, and Seelig J. Effect of a single cis double bond on the structure of a phospholipid bilayer. Biochemistry 1977;16:45-50.

29. Seelig J. Deuterium magnetic resonance : Theory and application to lipid membranes. Quarterly Reviews of Biophysics 1977;10:353-418.

30. Appelt C, Eisenmenger F, Kühne R, Schmieder P, Söderhäll JA. Interaction of the antimicrobial peptide cyclo(RRWWRF) with membranes by molecular dynamics simulations. Biophysical Journal 2005;89:2296-306.

30. Berger O, Edholm O, Jahnig F. Molecular dynamics simulations of a fluid bilayer of dipalmitoylphospatidylcholine at full hydration, constant pressure and constant temperature. Biophysical Journal 1997;72:2002-2013.

31. Schuler LS, Daura X, van Gunsteren WF. An improved GROMOS96 forcefield for aliphatic hydrocarbons in the condensed phase. Journal of computational chemistry 2001;22:1205-1218.

Chapter 6

Homology modeling and molecular dynamics study of peptide channels in lipid bilayers

6.1 Introduction

A number of modes of action of antibiotic peptides involve aggregation of the peptides resulting in either formation of channels or disruption of the membrane potential.[1-4] In Chapter 4 we showed that the tyrocidine peptides form dimers and higher oligomers by coming together in a sideways fashion. In this chapter we wish to explore the possibility that tyrocidine peptides also form channels within a membrane.

Gramicidin S (GrS), a peptide very similar to tyrocidine, is known to have antibiotic properties.[1, 5, 6] A crystal structure of a GrS channel has been solved.[7] The three-dimensional arrangement of the channel has hydrophilic and hydrophobic regions distinctly separated making it compatible with the lipid environment.[7] It is also long enough to be able to traverse a lipid membrane. The stability of a GrS channel, when inserted into a membrane has not been studied, and can influence its mechanism of action. The channel would function as an ion channel if it can steadily align itself parallel to the normal axis when inserted into a model membrane. However, if the channel structure is unstable upon insertion into the membrane, it could mean that GrS utilizes mechanisms different from the channel mechanism to kill bacterial cells.

The structure of the solved GrS channel is made up of two strands, a longer helical twisted (LHT) β-sheet and a shorter helical twisted (SHT) β-sheet as shown in Figure 6.1. The LHT β-sheet is comprised of 9 peptides, and the SHT β-sheet has 6 peptides making a total of 15 peptides in the channel. The monomers of GrS are very amphipathic. Hydrophilic ornithine residues make up one face of the peptide, and hydrophobic residues, Pro, Phe, Val, and Leu make up the other side of the peptide.[7] The monomers are arranged in such a way that the pore contains the side chains of hydrophilic Orn residues, and the hydrophobic residues make up the periphery of the channel. GrS monomers have on average of 3.5 direct hydrogen bonds, per monomer between the main chain atoms. A network of hydrogen bonds connects the monomers in the following sequence $(3,3,2,3,3)_n$.[7] The hydrophobic side chains of the Phe residues stabilize the channel through π-stacking interactions. The hydrogen bonding patterns, as well as the hydrophobic interactions, seem to play a major role in stabilizing the GrS channel. The inner radius of the GrS channel is 0.47 nm.[7]

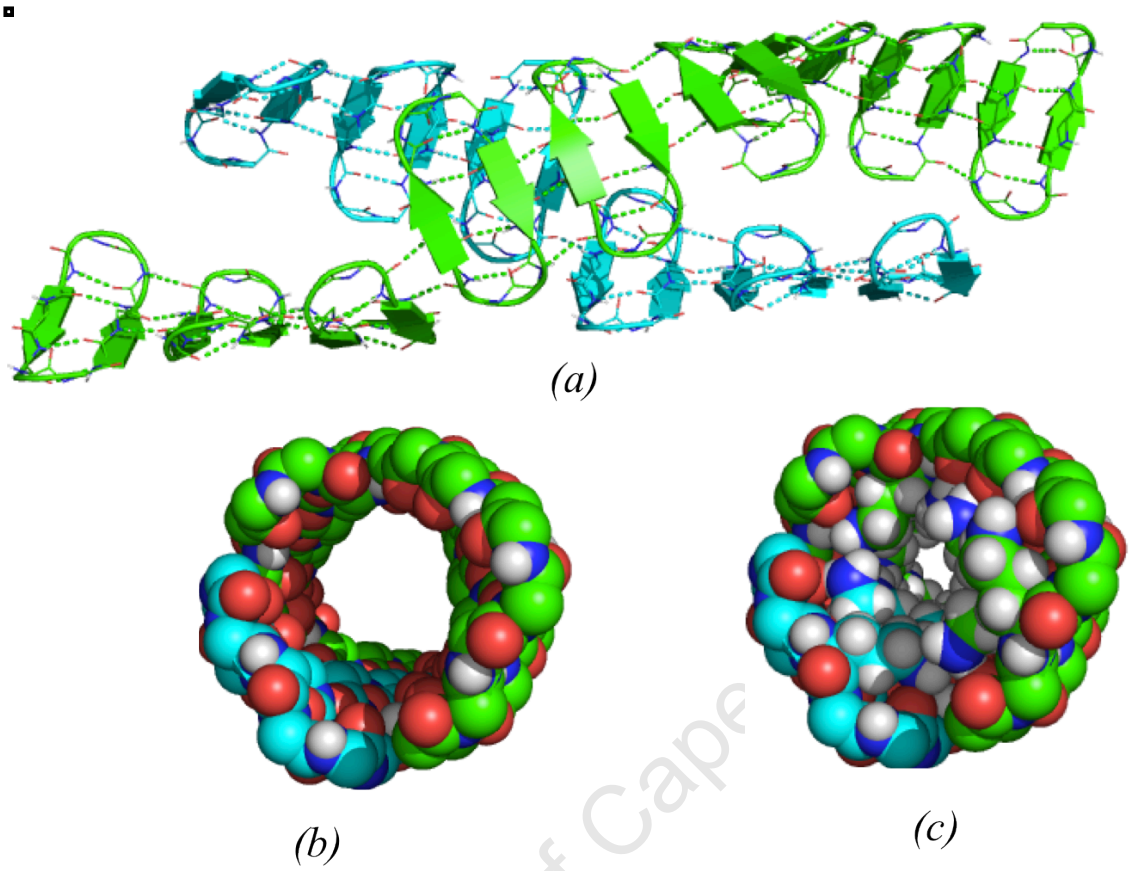

Figure 6.1: The schematics representation of the gramicidin S channel. (a) The two ribbons of gramicidin S that form the tube like channel are colored in cyan and green respectively. Hydrogen bonds are shown as broken lines. (b) Top view of the channel showing backbone atoms as spheres. (c) Top view of the channel showing the interior channel residues and backbone atoms as spheres. Structure obtained from Cambridge Crystallographic Data Centre (CCDC), accession number 626343.

The primary sequences of GrS and the major tyrocidines are very similar. It is, therefore, possible for tyrocidines and GrS to form similar channels. The purpose of this study was to construct tyrocidine channels, using homology modeling with the GrS channel as a template. Once the model tyrocidine channels had been constructed, molecular dynamics simulations were performed in model membranes to determine their stability. The GrS channel was also subjected to molecular dynamics in model membrane for comparison purposes.

6.2 Homology Modeling and Simulation Methods

The crystal structure of the GrS channel was obtained from the Cambridge Crystallographic Data Centre (CCDC), accession number 626343. It was used as the template in the homology modeling of tyrocidine channels. Pairwise sequence alignments were done using Modeller9v4[8] making sure that the conserved sequence VOLFP was aligned. This was also done in order to make sure that hydrophilic ornithine residues were inside the pore just like in the GrS channel. Homology modeling was performed using Modeller9v4.[8]

A pre-equilibrated 1-palmitoyl-2-oleoyl-sn-glycero-3-phosphoethanolamine (POPE) lipid membrane model was used. The water model used was SPC, [9] which behaves well in lipid bilayer/water simulations.[10] VMD[11] was used to make sure the channels were aligned to the membrane and that they had the same box coordinates. The channels were then centered within the saved box coordinates before being merged with the lipids. The lipids and water molecules that overlapped with the channel were removed.

Molecular dynamics simulations of the channel/membrane systems were carried out using the GROMACS software package.[12] The systems were energy minimized using the BFGS algorithm[13] for 1000 steps. After minimization, the systems were neutralized by the addition of Na+ ions. Position restrained MD simulations were performed for 1 ns, and water molecules were allowed to soak into all the channels except the TyrA channel. A force constant of 1000 $KJmol^{-1}nm^{-2}$ was used to keep the

backbone atoms of the channels immobile. Free MD simulation was performed for 100ns with structures being saved every 1 ns using a time step of 2 fs. Periodic boundery conditions were applied during the simulation. The simulations were carried out at constant temperature, pressure and number of particles (NPT). A cut-off of 1.15 nm was used for van der Waals interactions, and the particle–mesh Ewald method[14] was used to compute the electrostatic interactions. The peptide, POPE and solvent/Na^+ were coupled separately using the Berendsen coupling method to a temperature of 300 K using a coupling constant, τ_T, of 1 x 10^{-4} ns. The pressure coupling constant τ_p was 5.0 ps, and a compressibility of 0.000045 (1/bar) was used. Neighbour lists were updated every tenth integration time step.

6.3 Results and Discussion

6.3.1 Homology modeling

The representations of the channel models obtained from homology modeling are shown in Figure 6.2. The TyrA and TyrB pores are packed with Orn and Phe residues whereas the TyrC channel is packed with Orn and Trp residues. The periphery of TyrA channel is made up of a mixture of Pro, Phe, Tyr, Val, Leu, Asn and Gln. In TyrB and TyrC, Pro, Phe, Trp, Asn, Gln, Tyr and Leu residues form the periphery of these channels. The hydrogen bonds that connect the monomers do not follow any pattern. The average number of hydrogen bonds connecting the monomers is 2.5 in all the tyrocidine channels. The hydrophobic Phe and Tyr residues in the turn regions of the sheets were expected to pack the two β-sheets via hydrophobic interactions in the same way Phe residues pack β-sheets in GrS channel. Instead, the side chains of these particular residues were randomly placed on the periphery of the channels with very few forming π-π interactions. In some

peptides, the Gln side chains were oriented towards the inside of the channel such that it could interact with atoms inside the channel. The pore sizes were a bit smaller than that of the GrS channel because of the presence of bulk aromatic residues. The average size was about 0.40 nm.

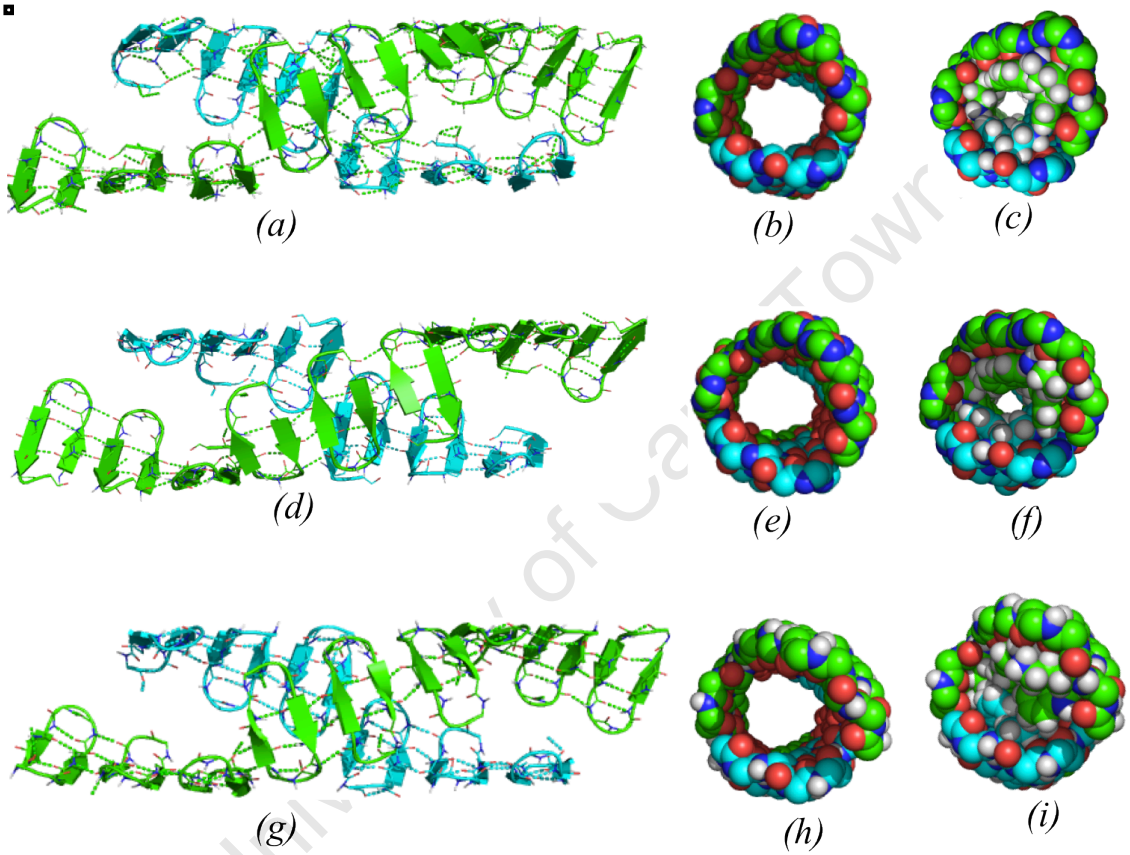

Figure 6.2. Tyrocidine pores from homology modeling. (a), (d) and (g) show the representation of TyrA, TyrB and TyrC pores respectively. The two β-sheets forming the pores are shown in green and cyan, respectively. Intramolecular and intermolecular hydrogen bonds are shown as broken lines along the pore axis. (b), (e) and (h) depict the top views of TyrA, TyrB and TyrC pores respectively, backbone atoms are represented as spheres. (c,) (f) and (i) are representations of the top views of TyrA, TyrB and TyrC pores respectively, only backbone atoms and side chains of residues packed inside the pores are shown.

The monomers of tyrocidines making up the channels were not entirely amphipathic; their hydrophilic and hydrophobic residues were not completely separated. Figure 6.3 shows the arrangement of side chains on the faces of the peptides. One face of TyrA and one of TyrB were made up of Phe and Orn residues. The other face of TyrA was comprised of Phe, Pro, Phe, Asn, Gln, Tyr, Val and Leu whereas that of TyrB has Phe, Pro, Trp, Asn, Gln, Tyr, Val and Leu residues. TyrC has Trp and Orn residues on one face, and the rest of the residues Pro, Phe, Trp, Asn, Gln, Tyr, Val and Leu make up the second face of the peptide. All the peptides had two antiparallel β -sheets that were connected together by two turns. The turn residues were conserved in all the peptides. The first turn was made up of Phe-Pro, and Gln-Tyr made up the second turn. Each peptide had an average of 3 hydrogen bonds between the main chain atoms.

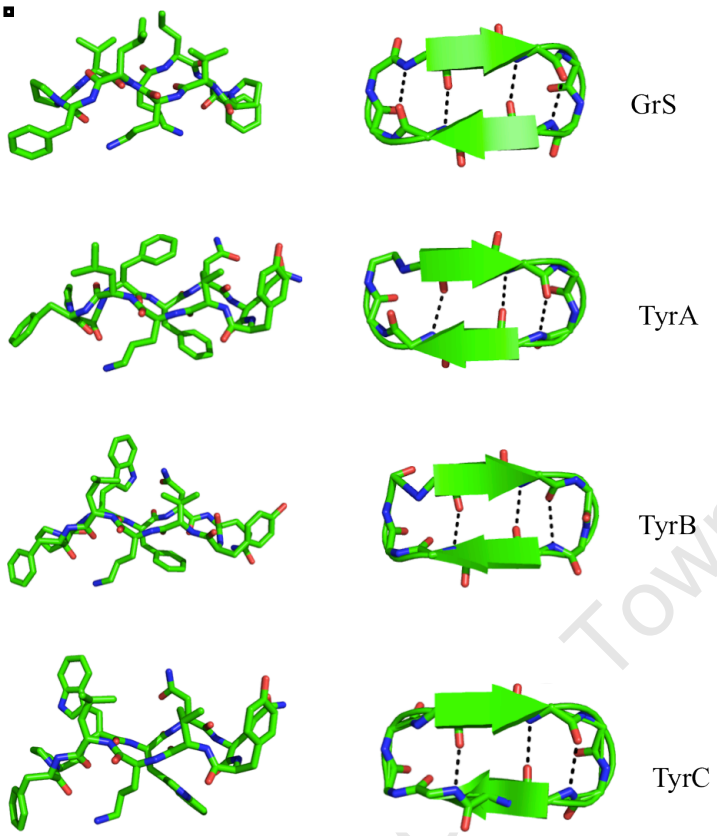

Figure 6.3: The structures of monomers extracted from channel models. Structures on the left side show the heavy atoms of the peptides. Structures on the right hand side represent the backbone atoms and the secondary structure representations of the monomers. The top structure was taken from the GrS channel used as the template during homology modeling.

6.3.2 Molecular Dynamics

6.3.2.1 Channel Stability

The ability of tyrocidines and GrS to form channels can only be confirmed by the stability of their model channels in membrane environments. Different aspects of the model channels were studied in order to determine their stability and water permeability.

Figure 6.4 shows the representations of the channels at the beginning and end of the simulations. The channels were inserted into the lipid membrane such that the last two peptides at the top of the LHT β-sheet were located in the water section of the simulation box. In all the systems, the last peptide at the bottom of the LHT β-sheet was also located in the water section. The peptides making up the SHT β-sheets were found in the lipid region of the membrane, with peptides at both ends found in the headgroups section of the lipids.

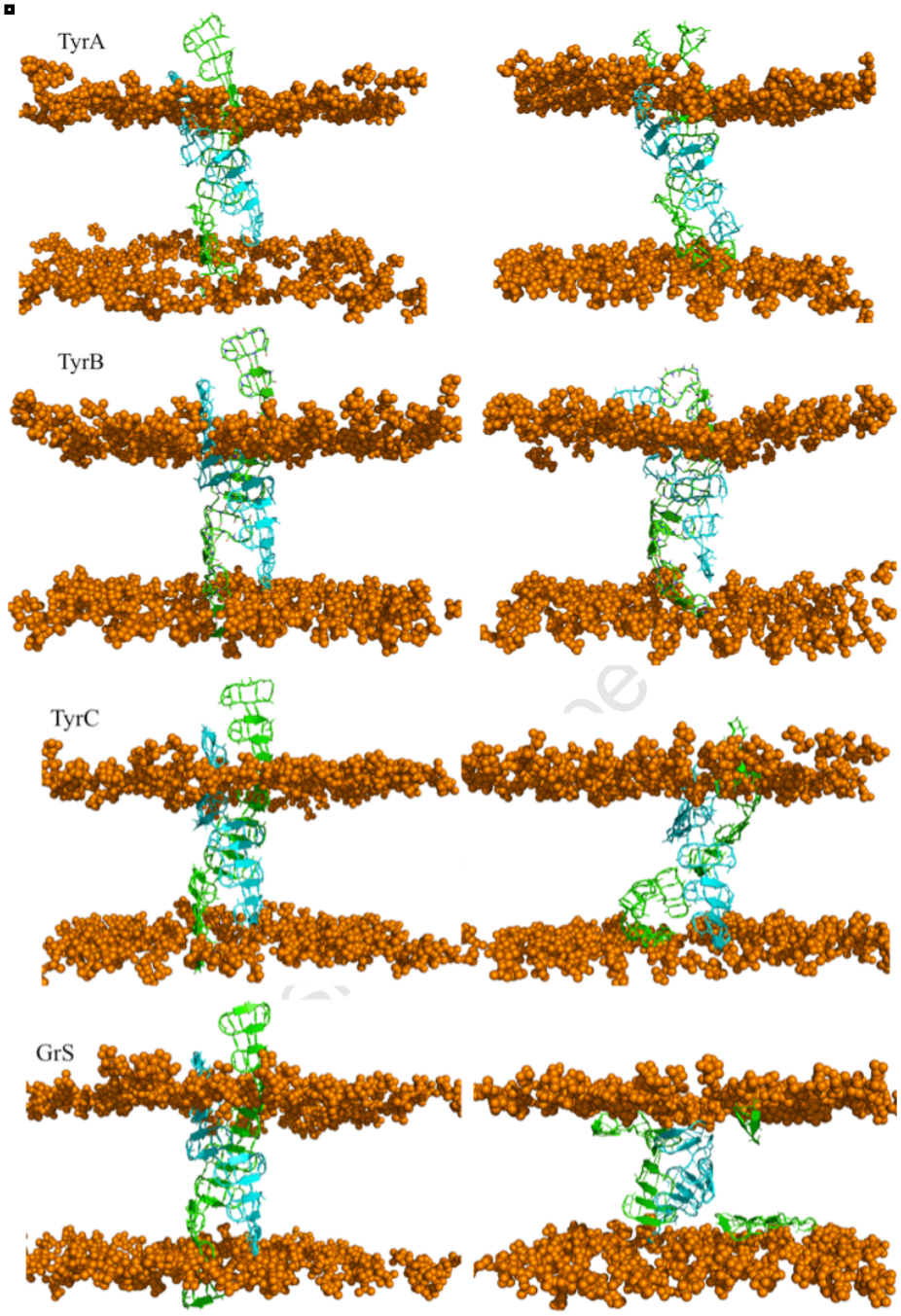

Figure 6.4: Structures of channel models in membrane before and after MD. Structure representations on the left hand side show the model channel in the membrane before molecular dynamics. The snapshots of the model channels after 100 ns MD are shown on the right hand side. The LHT β-sheets are shown in green and SHT β-sheets are colored in cyan, respectively. For clarity, the water section and the lipid tails were hidden in all the snapshots, lipid headgroups are shown as orange beads.

During the course of the simulations, peptides in the mouth regions (top and bottom ends) of the tyrocidine channels moved into the lipid headgroups area. The LHT β-sheet was distorted more than the SHT β-sheet in all the tyrocidine channels, and the TyrC sheet showed the biggest distortion. The last two peptides at the bottom of the LHT β-sheet of TyrC channel were tilted. At the end of the simulation the backbone structures of the last two peptides had changed from being perpendicular to being almost parallel to the surface of the lipid headgroups. The peptides in the water section at the top of the LHT β-sheet drifted to the lipid headgroups section. At the end of the simulation, only the terminal peptide at the top end of the LHT β-sheet was in the water section of the membrane. This peptide lost all of its main chain hydrogen bonding interactions with the peptide adjacent to it. This phenomenon resulted in the enlargement of the mouth regions of the TyrC channel.

For GrS, all the peptides of the LHT β-sheet that were in the water section at the beginning of the simulation completely detached from the channel during the simulation. The peptides separated from the LHT β-sheet after about 24 ns. The detached peptides quickly drifted into the lipid membrane. Once in the lipid section, the hydrophilic side of the peptides interacted with the lipid headgroups, and the hydrophobic side was in the hydrophobic tail section of the lipids. All the detached peptides retained the main chain interactions and the secondary structures.

In order to check the stability of the channels in the lipid membranes, the variation of root mean squared displacement (RMSD) with time was evaluated (Figure 6.5). The RMSD values for TyrA and TyrB increased sharply before leveling off at 0.5 nm within the first 20 ns of the simulation time. The structures that were formed corresponded to stable structures of these respective channels. The RMSD value of TyrC decreased gradually until it started to increase after 40 ns before stabilizing after 70 ns. GrS had an RMSD value that kept on increasing until the end of the simulation, however the rate at which it increased was decreasing with time. The maximum RMSD value of GrS was 1.5 nm at the end of the simulation. The variations of the RMSD values showed that TyrA and TyrB channels were more stable than the TyrC channel. The GrS channel was the least stable of the four channels.

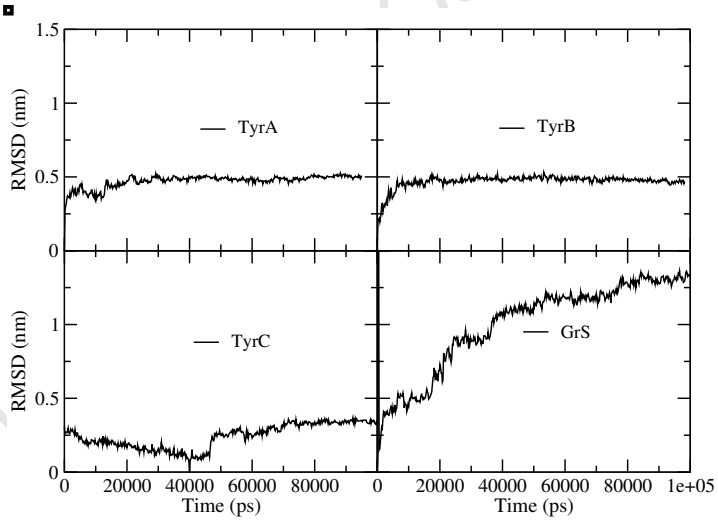

Figure 6.5: RMSD of the backbone atoms of the four channels, TyrA, TyrB, TyrC and GrS as a function of time.

The general trend of the stabilities of tyrocidine and GrS channels can be explained in terms of physicochemical properties of their respective peptides listed in Table 6.1. GrS channel was the least stable in the water section of the membrane because of its lipophilicity. TyrC has a lipophilic value that is higher than that of TyrA and TyrB hence its LHT β-sheet was more distorted than those of TyrA and TyrB. However, its peptides did not separate from the channel like the GrS peptides.

Table 6.1: Physicochemical properties of individual tyrocidines and GrS peptides.

Parameter	TyrA	TyrB	TyrC	GrS
Hydropathy[16]	24	23.7	23.4	29.2
Lipophilicity (L)[17,18]	9.55	10.01	10.47	11.66
Charge	+1	+1	+1	+2
Amphipathicity (Q/L)	0.105	0.100	0.096	0.172

The tilt angle was calculated between the longest axis of the SHT β-sheet and the z-axis of the simulation box as shown in Figure 6.6. This was because the SHT β-sheet was relatively stable and did not disintegrate for the duration of the simulations in all the channels. The centers of mass of the top and bottom peptides were used to define the axis of the SHT β-sheet.

The tilt angles of all the tyrocidine channels were maintained during the course of the simulations except for the TyrA channel. The tilt angle of TyrA increased to 17^0 before decreasing to 10^0 within the first 20 ns of the simulation. The fluctuation of the tilt angle was probably due to unfavorable interactions between the hydrophobic and hydrophilic groups of the channel and the membrane at the start of the simulation leading to a change in orientation of the channel.

There were no big changes in the tilt angles of TyrB and TyrC during the simulation. The angles were 7^0 and 20^0 respectively. The tilt angle of GrS channel increased gradually from 20^0 to 56^0 at the end of the simulation. The change in tilt angle was due to the movement of the 'terminal' peptides from the hydrophilic phase to the hydrophobic lipid tail region. Hydrogen bonding interactions stabilized the SHT β-sheet. The hydrogen-bonding network was so strong that the whole sheet tilted when the terminal peptides drifted into the membrane.

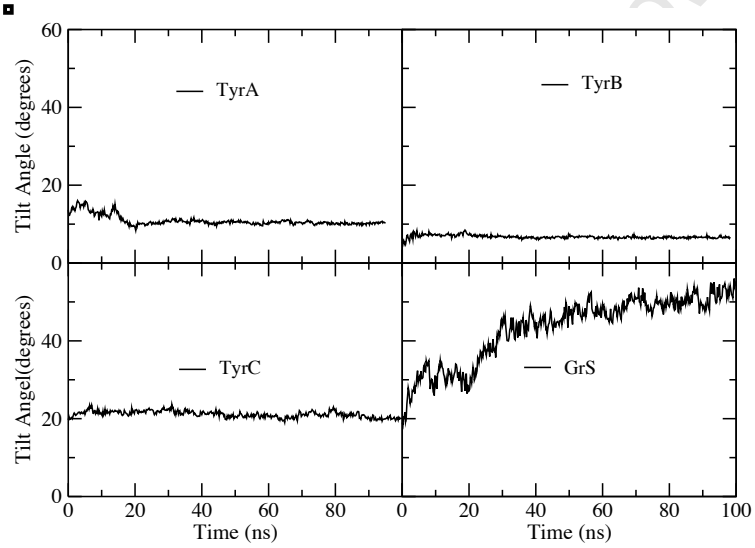

Figure 6.6. The tilt angle as a function of time for the four MD simulations of tyrocidines and gramicidine S channels. The tilt angle was defined as the angle between the z-axis of the SHT β-sheet and the normal of the bilayer plane.

The relatively stable tilt angles in tyrocidine channels were due to favorable interactions between the lipid molecules and the peptide residues. The presence of both hydrophilic and hydrophobic residues in the peripheries of tyrocidine channels is likely to be responsible for the relative stability in their tilt angles. As soon as the systems are equilibrated and the channels are tightly packed in the membrane the tilt angle stayed the

same. GrS channel had the biggest tilt angle and this is due to its lipophilicity, the periphery of GrS channel is made up of hydrophobic residues only, and these interact well with the hydrophobic lipid tails of the membrane, and poorly with the polar lipid headgroups.

6.3.2.2 Secondary structure Analysis

The DSSP program was used to analyze the secondary structure elements of the channels, and the results are shown in Figure 6.7. Peptide residues of the GrS channel maintained the same secondary structural features for most of the simulation. The tyrocidine channels did not. There were large variations in the secondary structural features of the peptides in the tyrocidine channels. However, the general oval shape of the peptides was maintained in almost all the peptides. When the β-sheet structures were lost, the peptides retained a β-bridge structure. In situations where the peptides lost their turn structures they formed bends. Residues 61-70 and residues 111-120 make up the peptides at the bottom and top of the LHT β-sheet respectively. The secondary structure elements of the peptides at both ends of the LHT β-sheet changed substantially during the simulations in TyrA, TyrB and TyrC channels and rarely formed β-sheet and β-turns. TyrB had the largest number of peptides that changed their secondary structure. For 50% of the simulation time, eight peptides of TyrB did not have the same secondary structural elements they had at the beginning of the simulation. TyrA and TyrC had 4 such peptides each. The change in the secondary structure of the peptides was independent of the environment. Peptides in both hydrophilic and hydrophobic environments lost their secondary structure elements during the simulations. Channels produced by homology modeling had fewer hydrogen bonds between the main chain atoms of different peptides

compared to the GrS channel hence GrS retained its secondary structure better than the tyrocidine channels.

6.3.2.3 Water Properties inside the channels

Water molecules were regarded to have entered the channel when they were within the central 1.5 nm of the lipid tails section of the membrane. The number of water molecules found in the channel systems varied between the channels as shown in Figure 6.8. This was attributed to the type and interactions between the side chains of residues that were packed inside the channels. TyrA channel had the lowest number of water molecules. During position restrained MD, water molecules were not allowed to soak into the TyrA channel hence it had no water molecules at the start of the free MD simulation. The amount of water molecules in the channel increases slowly to about 10 at the end of the simulation. Visual inspection showed that water molecules did not form a continuous channel as they were permeating the membrane region. They permeated the channel as small clusters by forming water-water, water-ornithine side chain, water-carbonyl oxygen or water-amide nitrogen hydrogen bonds. The rate at which water molecules permeated the membrane was slow. This was mainly because hydrophobic Phe residues formed π-stacking interactions in the central region of the channel thereby blocking water molecules for a good part of the simulation (Figure 6.9). A few water molecules managed to permeate the membrane through the pore and a few more through the periphery of the channel.

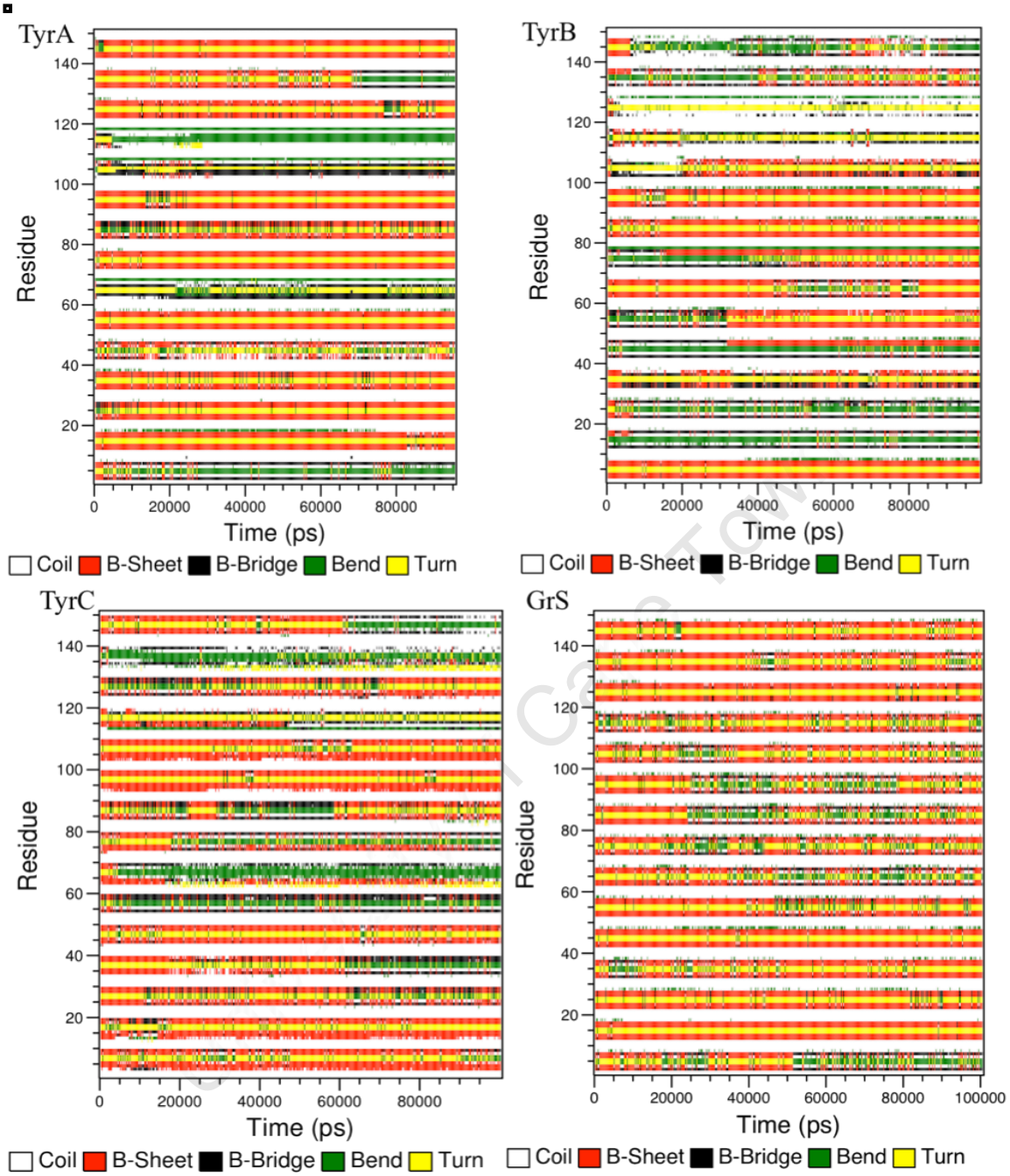

Figure 6.7: Secondary structure elements of residues in the model channels. Each peptide is made up of 10 residues and each channel has 15 peptides. Residues 1 - 30 and 121 - 150 make up the SHT β-sheet that is comprised of 6 peptides. Residues 31 - 120 make up the LHT β-sheet comprised of 9 peptides.

In the TyrB channel, the amount of water molecules decreases drastically from 60 to about 20 within the first 10 ns and thereafter remained constant until the end of the simulation. This was due to an increase in π-interactions between the hydrophobic phenyl rings of the Phe residues inside the channel, which resulted in water molecules being pushed out of the channel.

TyrA and TyrB contain the same residues, Orn and Phe, inside their channels, and so were expected to have the same channel properties. The difference in the number of water molecules permeating the channels was due to differences in orientations of the residues inside the channels. Figure 6.10B shows that the Phe residue at the bottom of the channel is oriented in such a way that it allows water molecules to pass through the channel. This may be regarded as an open state of the channel in that section. Phe residues found in the top section were oriented in such a way that they blocked water molecules from permeating the channel thereby producing what can be regarded as a closed state of the channel at that particular point. Most Phe residues in TyrA were oriented in such a way that they were blocking water molecules from permeating the channel (Figure 6.9B) hence TyrA contained the lowest number of water molecules. The hydrophobic residues inside the tyrocidine channels allow them to form a series of hydrophobic gates [15] within the same channel.

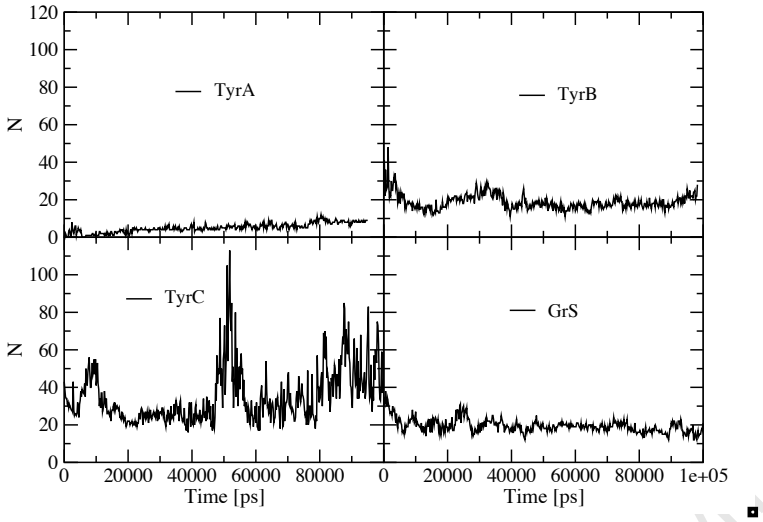

Figure 6.8: Variation of the number of water molecules (N) with time in model channels

In place of Phe, TyrC contains a more bulky Trp residue. The Trp residue contains an indole ring, which can form hydrogen bonds with water molecules. The number of water molecules in TyrC was greater than that found in the other channels. The LHT β-sheet of TyrC was distorted and allowed more water molecules to permeate the channel. An increase in the number of water molecules after 40 ns was due to the lateral movement of the LHT and SHT β-sheet from each other. Towards the end of the simulation, three Tyr residues on the exterior of the SHT β-sheet form intermittent hydrogen bonds. The Tyr residue at the top interacted with water molecules in the hydrophilic headgroup section resulting in the formation of an intermittent single file of water molecules on the periphery of the TyrC channel as shown in Figure 6.11.

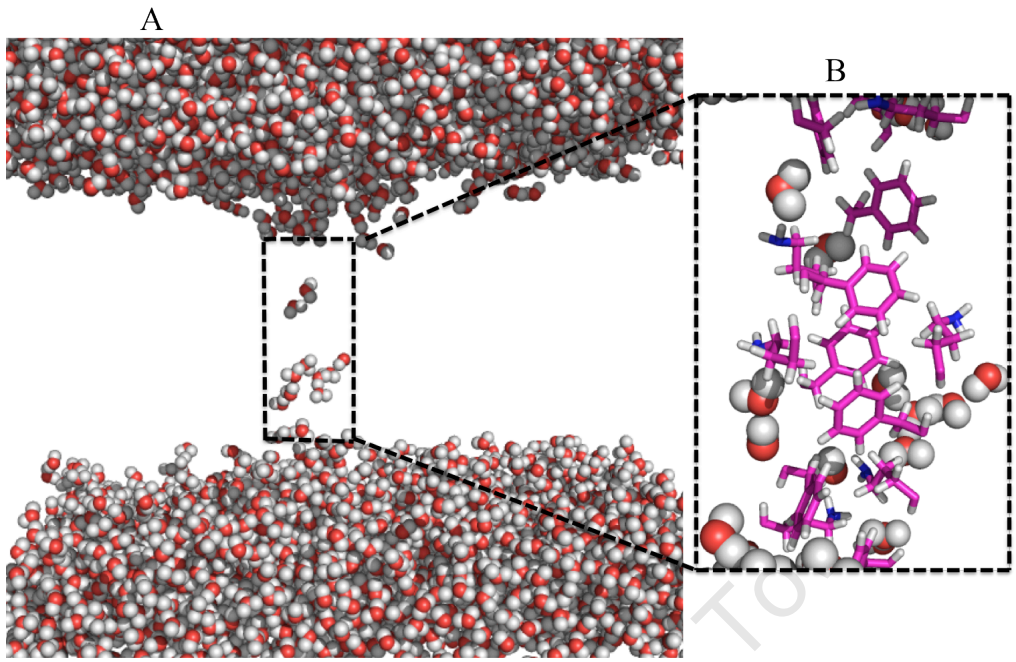

Figure 6.9: An illustration of a water filling event in TyrA channel. A. Only water molecules are shown for clarity. B. Enlargement of a section of the TyrA channel showing only water and residues that are located in the inside of the channel.

Only hydrophilic Orn residues are packed inside the GrS channel making it very hydrophilic. However at the beginning of free MD, the amount of water in the channel started to decrease. It decreased from ~40 water molecules to ~20 within the first 10 ns. This was mainly because of the reorientation of the β-sheets causing a reduction in the size of the channel thereby pushing some water molecules out of the channel.

It was also noted that the flux rate of water molecules through the channels was zero for a good part of the simulation. This implies that the number of water molecules moving in either direction of the channel was equal.

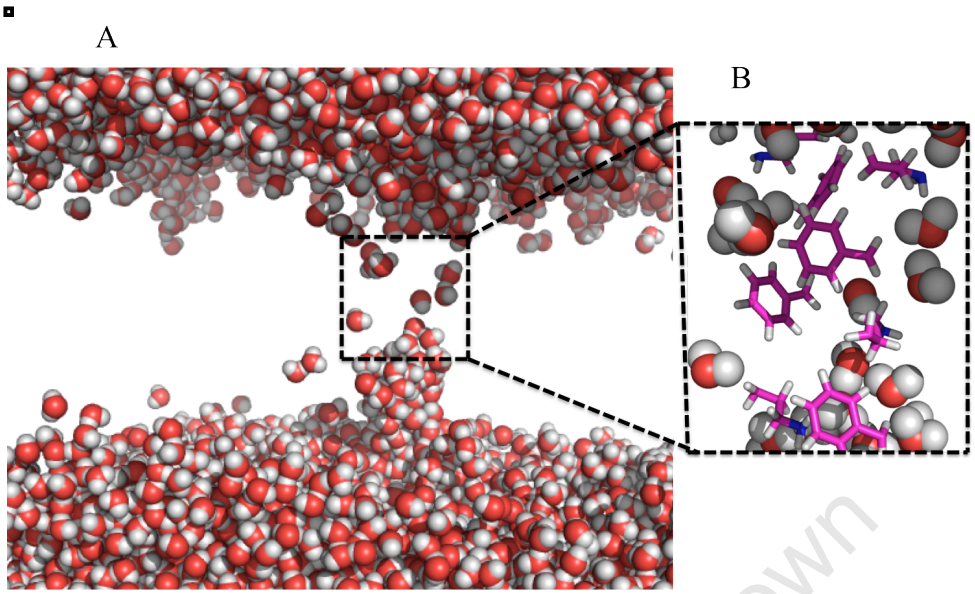

Figure 6.10: An illustration of a water filling event in Tyr B channel. A. Only water molecules are shown for clarity. B. Enlargement of a section of the TyrB channel showing only water and residues that are located on the inside of the channel.

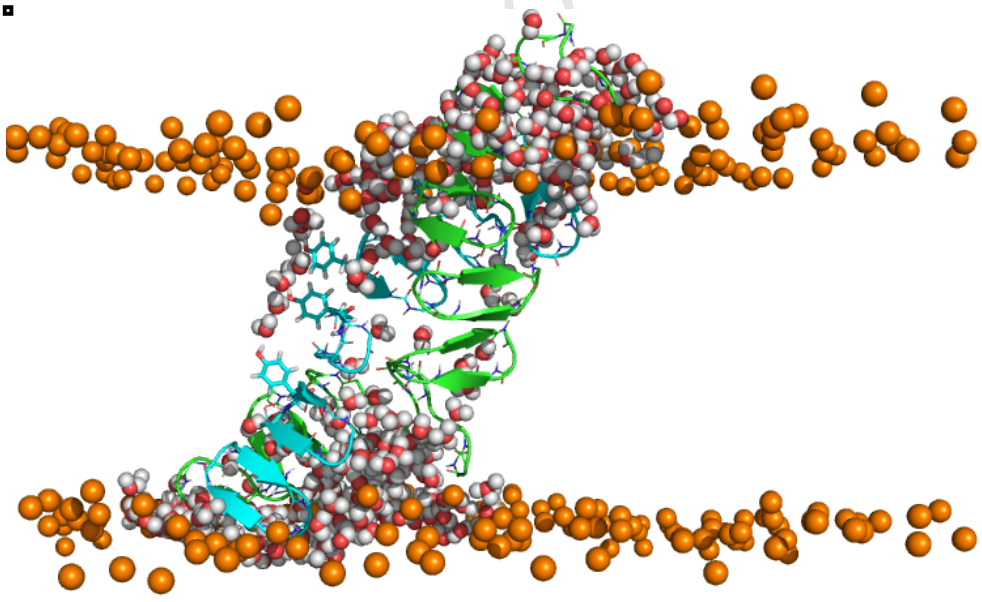

Figure 6.11: Snapshot of a molecular dynamic simulation showing water molecules in the interior and exterior sections of a TyrC channel. Tyr residues interacting with water molecules on the exterior side of the SHT β-sheet are shown as sticks. Phosphorous atoms in the headgroups section of the membrane are shown as orange beads. Water molecules in the lipid tails section and inside the channel are shown as red and white beads. The other parts of the lipids and water are hidden for clarity.

6.4 Conclusions

The channel models of tyrocidines obtained from homology modeling have low amphipathicity. This is because of the lack of total separation between hydrophobic and hydrophilic elements in the individual peptides. Notwithstanding this, all three tyrocidine peptides were able to form channels in the model membrane. The inside sections of the tyrocidine channels contained both hydrophobic and hydrophilic residues. The hydrophobic residues inside the tyrocidine channels could act as hydrophobic gates thereby regulating the rate at which water permeates the channels.

All the channels were relatively stable in the hydrophobic region of the membrane and unstable in the water section of the membrane. GrS channel was the least stable in the water section of the membrane due to the high lipophilicity of GrS peptides compared to tyrocidine peptides. The length of the channels influences their stability in the lipid membrane. Channels that are shorter or only equal in length to the length of the lipid bilayer are likely to be more stable. Starting orientations for the peptide channels tilted away from the normal to the bilayer surface, such that all monomers are within the lipophilic part of the membrane are also likely to be stable. That would still allow water (and ions) to diffuse through the polar head groups to the opening.

Water was able to permeate all the channels. However the rate at which water permeated was influenced by a number of factors such as the length of the channel, the stability of the channel, the radius of the channel and residues inside the channel.

6.5 References

1. Hancock REW, Chapple DS. Peptide antibiotics. Antimicrobial Agents and Chemotherapy 1999;43:1317-23.

2. Rozek A, Friedrich CL, Hancock RE. Structure of the bovine antimicrobial peptide indolicidin bound to dodecylphosphocholine and sodium dodecyl sulfate micelles. Biochemistry 2000;39:15765-74.

3. Gazit E, Bach D, Kerr ID, Sansom MS, Chejanovsky N, and Shai Y. The α-5 segment of bacillus thuringiensis δ-endotoxin: In vitro activity, ion channel formation and molecular modeling. Biochemical Journal 1994;304:895-902.

4. Strahilevitz J, Mor A, Nicolas P, Shai Y. Spectrum of antimicriobial activity and assembly of dermaseptin-b and its precusor form in phospholipid membranes. Biochemistry 1994;33:10951-60.

5. Bechinger B. The structure, dynamics and orientation of antimicrobial peptides in membranes by multidimensional NMR spectoscopy. Biochemica Et Biophysical Acta 1999;1462:157-84.

6. Prenner EJ, Lewis RNAH, McElhaney RN. The interaction of the antimicrobial peptide gramicidin S with lipid bilayer model and biological membranes. Biochimica Et Biophysica Acta (BBA) - Biomembranes 1999;1462:201-21.

7. Llamas-Saiz AL, Grotenbreg GM, Overhand M, van Raaij MJ. Double-stranded helical twisted -sheet channels in crystals pgf gramicidine S grown in the presence of trifluoroacetic and hydrochloric acids. Acta Crystallographica Section D 2007;63:401-7.

8. Šali A, Blundell TL. Comparative protein modelling by satisfaction of spatial restraints. Journal of Molecular Biology 1993;234:779-815.

9. Berendsen HJC, Postma J, van Gunsteren WF, Hermans J. Interaction models for water in relation to protein hydration. Dordrecht: D. Reidel 1981.

10. Tieleman DP, Berendsen HJC. Molecular dynamics simulations of a fully hydrated dipalmitoylphosphatidylcholine bilayer with different macroscopic boundary conditions and parameters. Journal of Chemical Physics 1996;105:4871-80.

11. Humphrey W, Dalke A, and Schulten K. VMD - visual molecular dynamics. Journal of Molecular Graphics 1996;14:33-8.

12. Berendsen HJC, Van der Spoel D, Van Drunen R. GROMACS: A message-passing parallel molecular dynamics implementation. Computational Physics Communication 1995;91:43-56.

13. Leiu DC, Nocedal J. On the limited memory BFGS method for large scale optimization. MATHEMATICAL PROGRAMMING 1989;45:503-28.

14. Darden T, York D, Pedersen L. Particle mesh ewald: An W log(N) method for ewald sums in large systems. Journal of Chemical Physics 1993;98:10089.

15. Beckstein O, Sansom MSP. The influence of geometry, surface character, and flexibility on the permeation of ions and water through biological pores. Physical Biology 2004;1:42-52.

16. Tossi A, Sandri L., Giangaspero A. New consensus hydrophobicity scale extended to non-proteinogenic amino acids, in: E. Benedetti, Pedone,C. (Ed.), Proceedings of the 27th European Peptide Symposium, Sorrento, 2002

17. Frecer V. QSAR analysis of antimicrobial and haemolytic effects of cyclic cationic antimicrobial peptides derived from protegrin-1. Bioorginic & Medicinal Chemistry 2006;14:6065-74.

18. Fauchere JL, Pliska V. Hydrophobic parameters pi of amino acide chains from the partitioning of N-acetyl-amino-acid amides. European Journal of Medicinal Chemistry 1983;18:369-75.

Chapter 7

Study of tyrocidine-Ca^{2+} complexation using NMR spectroscopy and quantum mechanical methods

7.1 Introduction

Studies have shown that in high Ca^{2+} concentration solutions, TyrC forms complexes, which can kill bacterial cells via a non-lytic mechanism,[1] that is a different mechanism from that proposed in Ca^{2+} free environments. The activities of cyclic daptomycin and other antimicrobial lipopeptides are also regulated by Ca^{2+}.[2-4] One of the proposed roles of Ca^{2+} is to lock daptomycin into an active conformation. This phenomena has also been observed in another relatively flexible molecule tsushimycin.[5-7] Metal ions lock these molecules into functional conformations that are more amphiphilic, which promotes their insertion into the membrane. The presence of Ca^{2+} also increases the cationic charge of the lipopeptide allowing it to readily interact with the negatively charged head groups.[5] This results in further membrane perturbation which may induce leakage. Other studies have also shown that Ca^{2+} promotes aggregation of TyrC peptides, which results in the formation of higher-order structures.[1] The aggregates formed by TyrC in Ca^{2+} environment are different from those formed in Ca^{2+} free environments, enabling them to kill bacterial cells using a non lytic mechanism.[1] In other studies calcium has been reported to cause membrane depolarization. This may not in itself be lethal as shown by potassium ion bound valinomycin, which has been found to be bacteriostatic.[4,8] However

when the membrane potential gradient is disrupted cells cannot synthesise ATP or take up nutrients needed for growth, and this may result in many other effects such as inhibition of protein, DNA, RNA, peptidodyglycan and lipid biosynthesis, which will eventually cause cell death.[5] These events may happen independent of each other or may together be responsible for cell death in divalent binding antibiotics. TyrC has also been shown to have antilisterial properties against a number of *Listeria monocytogenes* resistant strains,[9] which suggests that it may be used as a biopreservative. Some *Listeria monocytogenes* survive in the presence of cations. Antimicrobial properties of most molecules decrease in the presence of Na^{+}, Mg^{2+} and Ca^{2+} [10-14] making it difficult for them to destroy *Listeria monocytogenes* that are high temperature, salt and pH tolerant.[15-17] Understanding how TyrC binds Ca^{2+} is very important, and it can help in the development of new antibiotics that utilize more than one mechanism to destroy bacteria. This chapter focused on understanding the effect of Ca^{2+} binding on TyrC structure using quantum mechanics and NMR spectroscopy.

7.2 Methods

7.2.1 NMR titrations

^{1}H NMR experiments were performed on a Bruker Avance 400 MHz (Department of Chemistry, University of Cape Town) and an Avance II 500MHz (Department of Chemistry, University of Debrecen). TOCSY (mixing time, 60 ms),[18] NOESY (mixing time, 100ms)[19] and ROESY (mixing time, 150ms)[20, 21] spectra of the peptide, in water, were collected in the phase sensitive mode using the WATERGATE sequence to suppress the water resonance.[22] Spectral assignments were based on the method of Wüthrich.[21, 23] TyrC was a kind gift from Prof M. Rautenbach, Stellenbosch University,

and was isolated from natural sources. For the aqueous studies, 1.6 mg of TyrC was dissolved in 0.5 ml of 10:1 (v/v) H_2O:D_2O solution buffered at pH 5 with 50 mM sodium phosphate buffer solution. Trimethylsilylpropionate (TSP) was used as internal chemical shift reference. Ca^{2+} titrations were performed by adding Ca^{2+} solution ($CaCl_2$, 0.1M) directly to the NMR tube.

7.2.2 Quantum calculations

The root conformation of TyrC obtained from MD simulations was used as the starting structure in quantum mechanical calculations. Quantum calculations were carried out using Gaussian 09 software. The optimization of the geometries of the TyrC free peptide and the TyrC-Ca^{2+} complexes was done at the density functional level of theory (DFT) using the B3LYP functional and the 6-31G(d) basis set. Placing calcium ions in two different positions on the TyrC peptide generated two TyrC-Ca^{2+} complexes. The calcium ion was placed closer to atoms that were believed, from the NMR results, to be involved in binding. One Ca^{2+} was placed close to the carbonyl moeties of Phe^{1} and Leu^{10} whereas the other one was placed on the other end of the the peptide close to the carbonyl moeties of Asn^{5} and Gln^{6}.

The Gaussian optimized structures were used to determine the NMR properties of the amide protons. Chemical shielding calculations were performed using the GIAO method. The calculated absolute shielding constants were converted into chemical shifts in order to be able to compare them with the experimental values. To convert the shielding constants to the chemical shifts in ppm, the isotropic value of the concerned proton *i* was subtracted from the isotropic value of the protons in the reference (REF) as

shown in equation 7.1 below.

$$\delta_i \text{ (ppm)} = \text{isotropic (REF)} - \text{isotropic } (i) \qquad (7.1)$$

Acetamide was used as a reference instead of trimethylsilylpropionate (TSP) because acetamide has a chemical environment similar to the one in the peptide chains. The reference value for amide protons used was 27.31 ppm calculated with the B3LYP functional using the 6-311+G(2d,p) basis set. A value of 6.40 ppm was added to the calculated chemical shifts to take into account the fact that TSP was used as the reference when experimental chemical shifts were determined. 6.40 ppm is the experimental amide proton chemical shift of acetamide with respect to TSP.

7.3 Results and Discussion

7.3.1 NMR titrations

The NMR titration showed very small chemical shift changes for the amide protons with progressive addition of $CaCl_2$. The fact that there were differential shifts indicates that the effect is due to specific residue binding rather than a change in dielectric constant due to the added calcium. Similar small changes in the H^N chemical shift were shown in the second Ca^{2+}-binding domain of a sodium–calcium exchanger. [24] Phe^1 was responsible for the largest chemical shift change recorded, and it was -0.039 ppm. The other chemical shifts that were relatively large compared to the rest belonged to amide protons of Asn^5, Val^8 and Leu^{10}. The values of the chemical shift changes were -0.021, 0.013 and -0.019 respectively. The rest of the amide protons had chemical shift changes that were less than 0.01 ppm. The amide proton of ornithine could not be detected during the titration

(presumably due to exchange with deuterium). The resistance to change of amide protons of the free peptide upon addition of a metal indicates that Ca^{2+} binds weakly to the TyrC peptide. The residues that showed significant shift changes are very far from each other in the calcium free peptide. This could be because some of the shift changes are not caused by the involvement of the particular residues in Ca^{2+} binding or could indicate that there are two potential Ca^{2+} binding sites. The residues that showed some chemical shift changes are not acidic in nature except Asn^{5}. This could mean that carbonyl moieties of the respective residues are involved in Ca^{2+} binding. An attempt to probe the strength of binding between Ca^{2+} and TyrC using isothermal titration calorimetry (results not shown) were unsuccessful as the heats of solvent mixing were greater than the heat of complexation.

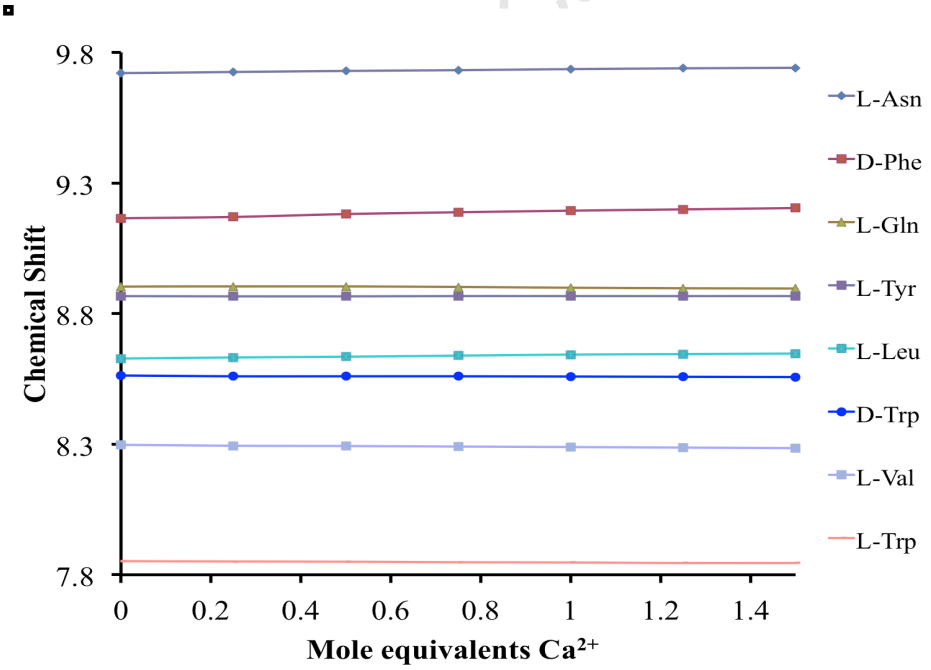

Figure 7.2: Variation of the amide proton chemical shifts with Ca^{2+} concentration.

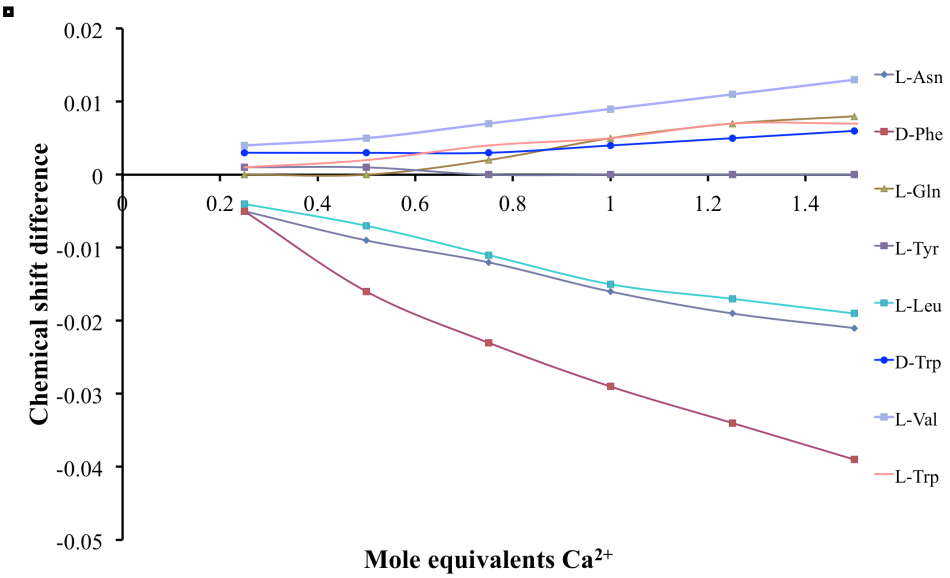

Figure 7.3: Variation of the amide proton chemical shift with Ca^{2+} concentration.

7.3.2 Quantum calculations

The optimized structure of TyrC is shown in Figure 7.4. There was not much change in the structure of the free peptide during geometry optimization. The conformation that was determined from MD calculations was largely retained. The electro potential surface of the peptide was also determined to show how charge was distributed around the peptide (Figure 7.5). Since calcium ion is positively charged it would be expected to bind to regions with high concentration of negative charge. The electro potential surface shows that the negatively charged areas were very far from each other and would require a large conformational change of the peptide for Ca^{2+} to form a stable complex with the peptide. These negative charges were also from residues that had not shown significant chemical shift changes during the NMR experiments.

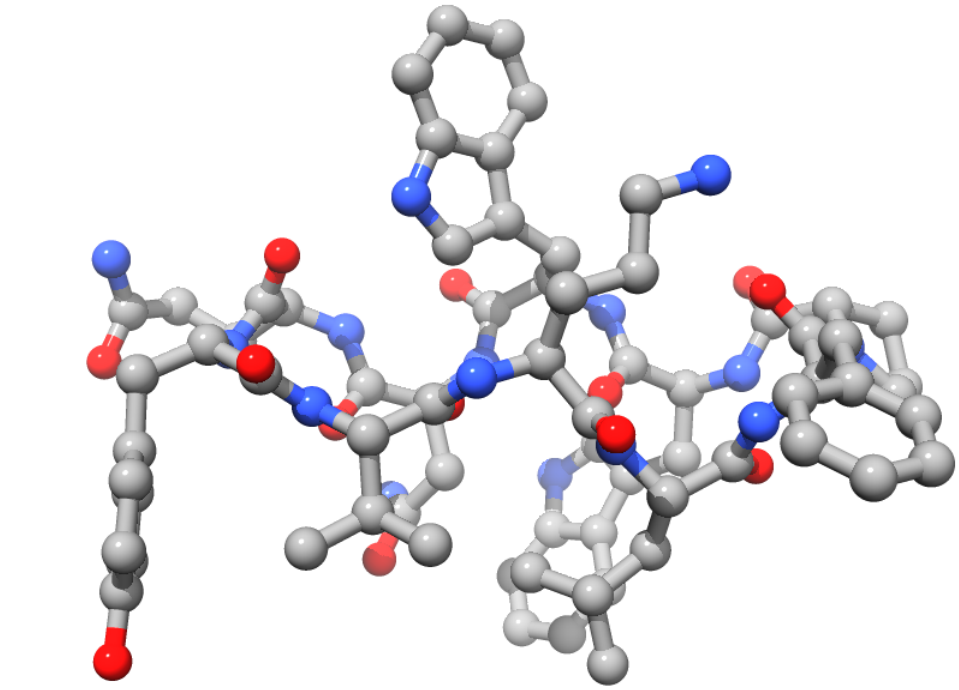

Figure 7.4: The DFT optimized structure of TyrC using B3LYP/6-31G(d)

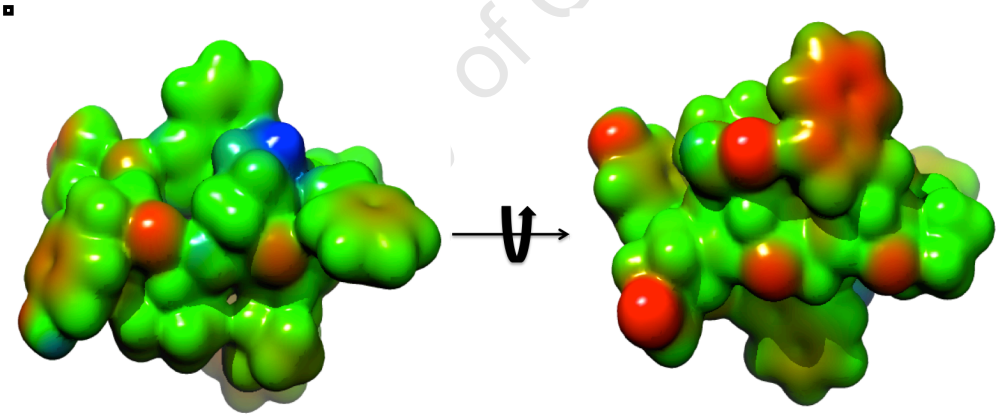

Figure 7.5: The electro potential surface for the optimized geometry of TyrC. Red indicates a region with high negative charge, blue indicates a region with high positive charge and green indicates a neutral region.

The theoretical chemical shift values of the free peptide were compared to those determined experimentally (Figure 7.6). There was a general correlation in the trends of the theoretical and experimental chemical shifts for most residues. However, for most residues, theoretical chemical shifts were lower than their experimental counterparts. The

chemical shifts of residues Phe[1] and Orn[9] were significantly lower than their corresponding experimental values. The theoretical chemical shift of Phe[1] was lower by 0.8 ppm, and that of Orn[9] was lower by 1.8 ppm. Only Val[8] and Leu[10] had their chemical shift values higher than their corresponding experimental values. The chemical shift value of Val[8] was slightly bigger by 0.1 ppm while that of Leu[10] was bigger by 0.9 ppm. Results indicated that the chemical shift values of residues Phe[1],Orn[9] and Leu[10] were significantly different from their corresponding experimental values. Overall, it can be concluded that the geometries of the theoretical and experimental peptides were similar, and the theoretical chemical shifts were generally underestimated.

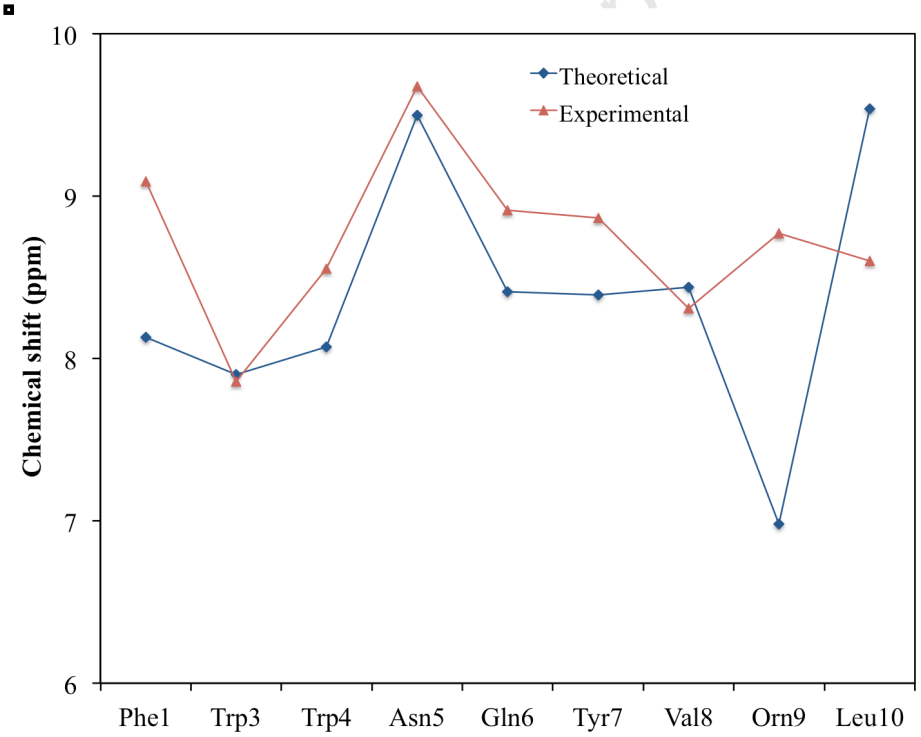

Figure 7.6: Free peptide theoretical vs experimental chemical shifts of the amide protons.

The optimized geometries of TyrC-Ca^{2+} complexes are shown on Figure 7.7 and Figure 7.8. In the first complex, the Ca^{2+} ion is bound to four amide carbonyl oxygens of TyrC. The average Ca^{2+} … O distance in the first complex is 0.25 nm. Figure 7.7 shows that in the second complex, Ca^{2+} ion is bound to three amide carbonyl oxygens. The average Ca^{2+} … O distance in the complex is 0.24 nm. It can also be noted that the Ca^{2+} ion is interacting with the pi-electrons of Trp^{3} residue. The binding energies of both complexes is -17.78×10^{5} $kJmol^{-1}$indicating that they have the same stabilities. However it should be noted that in the presence of a solvent the binding energy may be different. This is beccause in the presence of a solvent, the binding energy is not determined by the bare potential energy of interaction of the two species, but rather by the difference in the free energy of the complex plus the solvated calcium ion plus the solvated tyrocidine molecule and the free energy of the complex plus the free energy of the liberated water molecules now interacting with themselves.

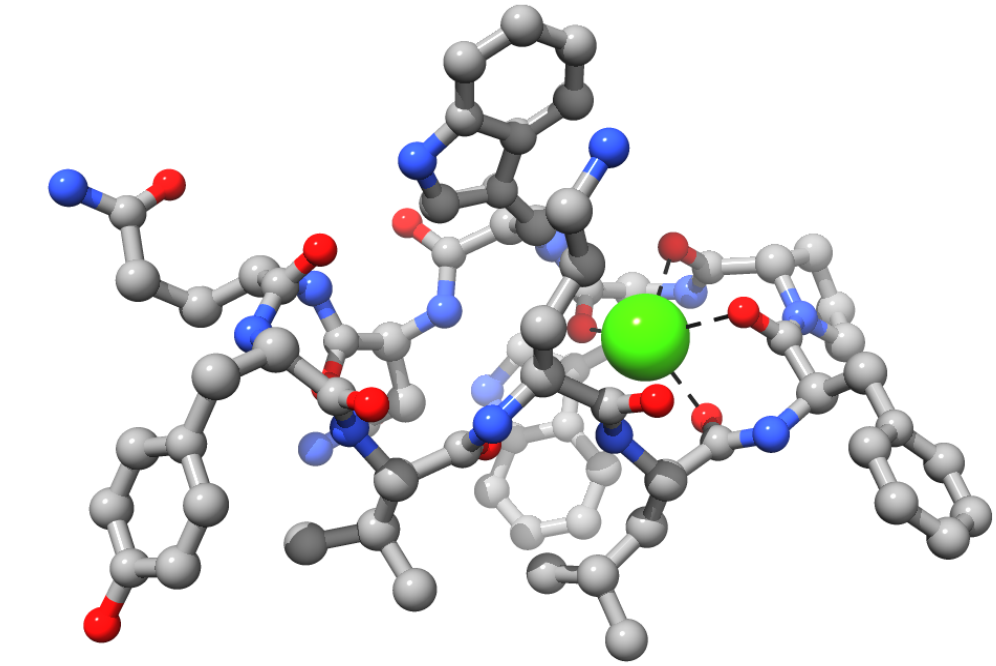

Figure 7.7: DFT optimized structure of TyrC-Ca^{2+} complex 1 (B3LYP/6 – 31G(d)) Ca^{2+} is shown as a green sphere. Bonds between carbonyl oxygens and Ca^{2+} are shown in black.

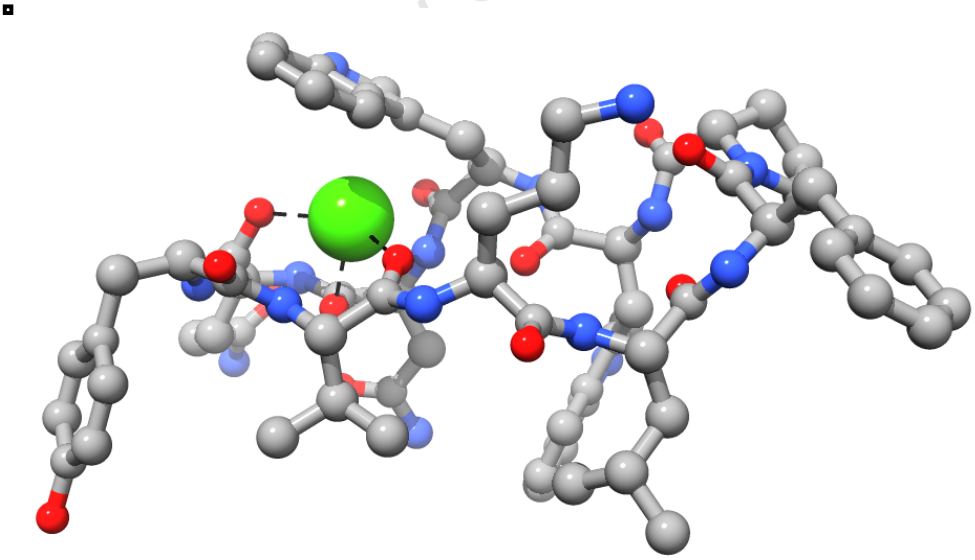

Figure 7.8: DFT optimized structure of TyrC-Ca^{2+} complex 1 (B3LYP/6 – 31G(d)) Ca^{2+} is shown as a green sphere. Bonds between carbonyl oxygens and Ca^{2+} are shown in black.

Upon comparison of the calculated chemical shifts of the complexes to their corresponding counterparts in the free peptide, it was observed that the trends of the chemical shifts were very different (Figure 7.9). The amide proton chemical shift of Gln^6 for complex 2 was 13.3 which is very high for an amide proton. This suggests that the chemical shift value was probably overestimated. All the 10 amide proton chemical shifts of complex 1 were deshielded except Asn^5 which was shielded. Overall, the changes in the chemical shifts were very large in the calculated complexes compared to the experimentally observed chemical shifts.

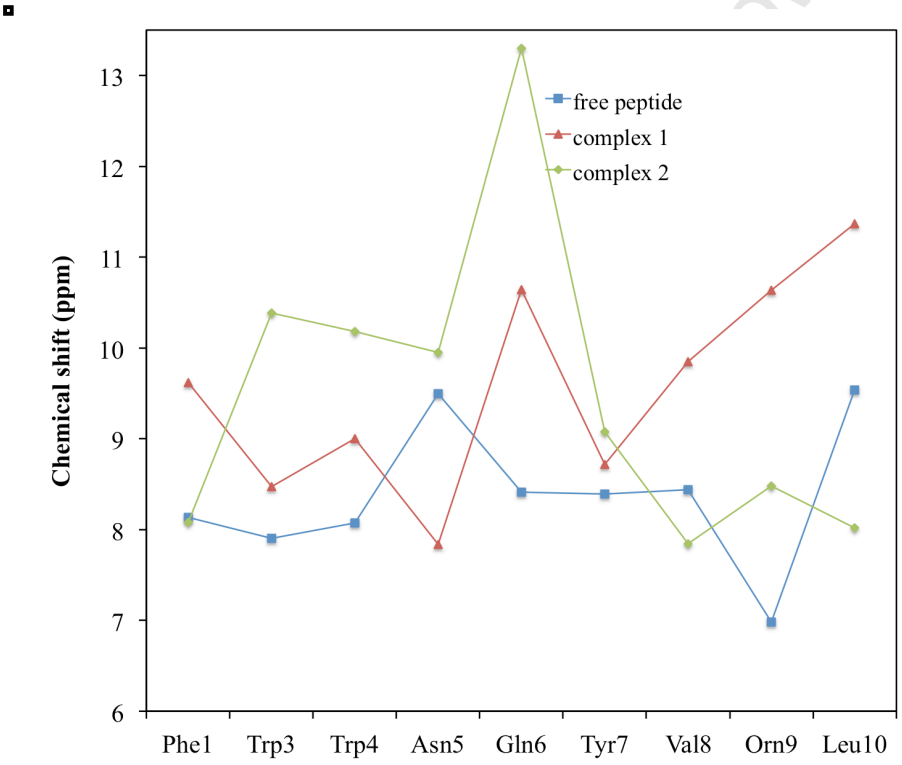

Figure 7.9: Comparison of calculated and experimental chemical shifts of TyrC free peptide and TyrC-Ca^{2+} complexes

Figure 7.10 shows the comparison of theoretical chemical shifts of the complexes to the experimental chemical shifts of the complex. There were significant differences between the calculated and experimental chemical shifts. Complex 1 had only three residues,

Phe[1], Trp[3] and Tyr[7] with theoretical values close to their corresponding experimental chemical shifts. The rest of the chemical shifts were significantly different. Only Asn[5] and Tyr[7] in complex 2 had theoretical chemical shift that were very similar to their experimental counterparts, and the rest of the residues had very different chemical shifts. The general trends of the chemical shift values differed significantly between the two complexes and the experimental values.

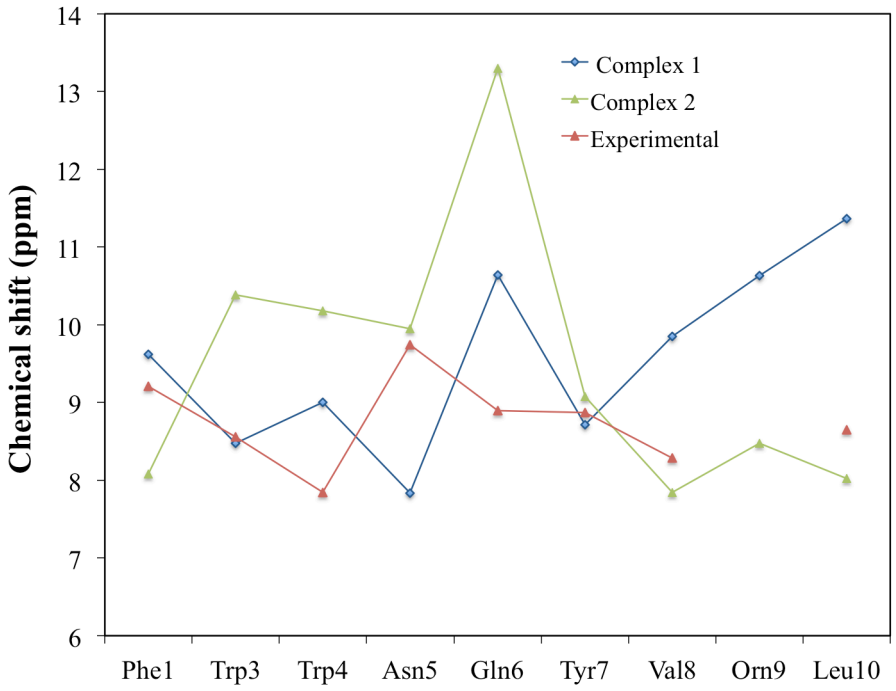

Figure 7.10: Comparison of calculated and experimental chemical shifts of TyrC-Ca^{2+} complexes

Previous studies have shown that at low Ca^{2+} concentration, the mechanism of action of TyrC is the same as that found in the Ca^{2+} free environment [1]. This suggests that at low concentration the binding between Ca^{2+} and TyrC is very weak and has no influence on the aggregation and membrane interaction of TyrC. The significant changes in the structure of TyrC shown by big changes in the chemical shifts and high binding energies

of complexes 1 and 2 indicate that complex 1 and complex 2 may not be the ones being formed at low Ca^{2+} concentration. The mechanism of action of TyrC changes to a non-lytic one at very high Ca^{2+} concentration [1]. This is likely to be due to the type of peptide aggregates formed which may be different in size or in orientation to those found in Ca^{2+} free enviroments.

7.4 Conclusion

Experimental results showed that Ca^{2+} weakly binds tyrocidine C. There were very small chemical shift changes in the presence of Ca^{2+} indicating that there was no significant change in the structure of the peptide. The tyrocidine-Ca^{2+} complexes that were obtained using quantum mechanical calculations were quite stable, however the correlation between quantum mechanical calculations and NMR chemical shifts was poor.

7.5 References

1. Spathelf BM. Qualitative structure-activity relationships of the major tyrocidines, cyclic decapeptides from bacillus aneurinolyticus. PhD Thesis, Stellenbosch University; 2010.

2. Lakey JH, Ptak M. Flourescence indicates a calcium dependent interaction between the lipopeptide antibiotic LY 146032 and phospholipids. Biochemistry. 1988;27:4639-45.

3. Lakey JH, Lea EJA. The role of acyl chain character and other determinants on the bilayer activity of A21978C an acidic lipopeptide antibiotic. Biochemica Et Biophysical Acta-Biomembranes 1986;859:219-26.

4. Allen NE, Alban Jr WE, Hobbs Jr JN. Inhibition of membrane potential dependent amino acid transport by daptomycin. Antimicrobial Agents and Chemotherapy 1991;35:2639-42.

5. Jung D, Rozek A, Okon M, Hancock REW. Structural transitions as determinants of the action of the calcium-dependent antibiotic daptomycin. Chemistry & Biology 2004 7;11:949-57.

6. Bunkoczi G, Vertesy L, Sheldrick GM. Structure of the lipopeptide antibiotic tsushimycin. Acta Crystallographica Section D 2005;61:1160-4.

7. Bunkoczi G. Structure determination of peptides with antimicrobial action. Goettingen, Germany: Goettingen, Germany; 2004.

8. Canepari P, Boaretti M, Lleo MM, Satta G. Lipoteichoic acid as a new target for activity of antibiotics: Mode of action of daptomycin (LY146032). Antimicrobial Agents and Chemotherapy 1990;34:1220-6.

9. Spathelf BM, Rautenbach M. Anti-listerial activity and structure–activity relationships of the six major tyrocidines, cyclic decapeptides from bacillus aneurinolyticus. Bioorganic & Medicinal Chemistry 2009;17:5541-8.

10. Bals R, Goldman MJ, Wilson JM. Mouse beta-defensin 1 is a salt-sensitive antimicrobial peptide present in epithelia of the lung and urogenital tract. Infection and Immunity 1998;66:1225-32.

11. Cociancich S, Ghazi A, Hetru C, Hoffmann JA, Letellier L. Insect defensin, an inducible antibacterial peptide, forms voltage-dependent channels in micrococcus luteus. The Journal of Biological Chemistry 1993;268:19239-45.

12. Lehrer RI, Ganz T, Szklarek D, Selsted ME. Modulation of the in vitro candidacidal activity of human neutrophil defensins by target cell metabolism and divalent cations. The Journal of Clinical Investigation 1988;81:1829-35.

13. Broekaert WF, Terras FRG, Cammue BPA, Osborn RW. Plant defensins: Novel antimicrobial peptides as components of the host defense system. Plant Physiology 1995;108:1353-8.

14. Bowdish DME, Davidson DJ, Lau YE, Lee K, Scott MG, Hancock REW. Impact of LL-37 on anti-infective immunity. Journal of Leukocyte Biology 2005;77:451-9.

15. Gandhi M, Chikindas ML. Listeria: A foodborne pathogen that knows how to survive. International Journal of Food Microbiology 2007;113:1-15.

16. Parente E, Giglio MA, Ricciardi A, Clementi F. The combined effect of nisin, leucocin F10, pH, NaCl and EDTA on the survival of listeria monocytogenes in broth. International Journal of Food Microbiology 1998;40:65-75.

17. Pearson LJ, Marth EH. *Listeria monocytogenes* - threat to a safe food supply: A review. Journal of Dairy Science 1990;73:912-28.

18. Braunschweiler L, Ernst RR. Coherence transfer by isotropic mixing: Application to proton correlation spectroscopy. Journal of Magnetic Resonance 1983;53:521-8.

19. Jeener J, Meier BH, Bachmann R, Ernst RR. Investigation of exchange processes by two-dimensional NMR spectroscopy. Journal of Chemical Physics 1979;71:4546-53.

20. Bax A, Davis DG. Practical aspects of two-dimensional transverse NOE spectroscopy. Journal of Magnetic Resonance 1985;63:207-13.

21. Weber PL, Morrison R, Hare D. Determining stereo-specific 1H nuclear magnetic resonance assignments from distance geometry calculations Journal of Molecular Biology 1988;204:483-7.

22. Sklenar V, Piotto M, Leppik R, Saudek V. Gradient-tailored water suppression for $^{1}H—^{15}N$ HSQC experiments optimized to retain full sensitivity. Journal of Magnetic Resonance 1993;102:241-5.

23. Wuthrich K. NMR of proteins and nucleic acids. New York: John Wiley & Sons; 1986.

24. Breukels V, Vuister GW. Binding of calcium is sensed structurally and dynamically throughout the second calcium-binding domain of the sodium/calcium exchanger. Proteins: Structure,Function, and Bioinformatics 2011;78:1813-1824.

Chapter 8

Conclusions and recommendations

8.1 Conclusions

The aim of this study was to understand the mechanism of action of antimicrobial cyclic tyrocidine deca-peptides. In order to study this, a number of objectives were drawn up based on the hypotheses that tyrocidine peptides either use a lytic or non-lytic mechanism to kill bacteria. The objectives included the determination of the structure of tyrocidine peptides in aqueous and membrane-mimetic environments. This was studied because it is understood that non-linear antibiotic peptides (the most studied antibiotic peptides) are known to be unstructured in the aqueous phase[1, 2] and to adopt specific "active" conformations upon interaction with a membrane. The results indicated that TyrA and TyrC form β-structures in both aqueous and membrane mimetic environments. This was in agreement with previous studies.[3, 4] However TyrB was unstructured in water and formed β-structure in a membrane mimetic environment. The structure of TyrB in a membrane environment was also in agreement with previous studies, however the unstructured conformation obtained in water was different from those reported before [4]. Spathelf [4] determined that TyrA forms the most stable β-sheets compared to TyrB and TyrC, and that the stability of the β-structures was attributed to self-assembly/aggregation of the peptides. There is therefore a possibility that TyrB could form a β-structure upon aggregation. The structures that were obtained in membrane mimetic environment and

those of TyrA and TyrC in water were similar. There was no total separation of hydrophobic and hydrophilic residues between the non-polar and polar faces of the peptides indicating that tyrocidines have low amphipathicity. In all the β-structures, residues Trp^4/Phe^4 and Orn^9 were always on the same face.

The mechanism of self-assembly of TyrC in aqueous environment was also studied. This was done in order to determine if tyrocidines adopt higher-order structures prior to membrane binding. The first step in the aggregation process, dimerization, was studied first. Dimerization was initially studied at 300 K, which is physiological temperature, however, it was discovered that most of the dimer conformations that TyrC formed at that temperature were in meta-stable states. Simulations were repeated at 400K assuming that dimers in trapped conformations would be able to overcome energy barriers. The results indicated that TyrC forms dimers in aqueous environment whereby individual monomers come together in a sideways orientation. The binding free energies of the predominant dimer conformations were very similar indicating that all the dimers have almost the same probability of being formed. From the results, it was observed that there is a possibility for TyrC to form higher order structures by adding monomers on either side of the dimer.

Simulations containing high peptide concentrations were also performed. The change in the solvent accessible surface area of hydrophilic residues was much less than that of hydrophobic residues indicating some degree of orientation during the aggregation, where the hydrophobic residues were being hidden from the solvent. This is

consistent with what is known about protein folding. This was also consistent with what was observed in previous studies, which showed that tyrocidine peptides aggregate in solution.[4-7] TyrB is known to form globular aggregates that resemble micelles, which do not allow metal ions to pass through. It has also been shown that tyrocidine peptides aggregate in solution such that hydrophobic residues are buried from the aqueous environment.[4] DOSY experiments did indeed show that TyrC aggregated in solution but in this experiment the size of the aggregate was 7 units. Simulation results showed that TyrC forms one large and globular structure made up of about 12 monomers in some instances, whereas DOSY experiments indicated that TyrC forms aggregates made up of about 7 monomers. This difference could have been due to the difference in the concentration of peptides that were used. In order to get comparable results there is therefore a need to repeat the simulations using concentrations that are similar to the ones used in DOSY experiments or to repeat the DOSY experiments at higher concentration or to study aggregation as a function of time. Each of these proposals has problems, dilute simulations take much longer and TyrC is expensive and has limited water solubility.

The interactions of tyrocidine peptides with the membrane models produced some interesting but rather expected results. The effect of peptides on both mammalian and bacterial membranes was studied. The results indicated that tyrocidine peptides could perturb both membranes in the same manner. This explained previous studies that showed that tyrocidine peptides are non-selective.[8-10] It was also concluded that extensive aggregation/self-assembly in the aqueous phase of the membrane reduces the interaction between the peptides and membrane. This was also pointed out in previous studies[4].

Overall, it was hypothesised that tyrocidine peptides could destroy the membrane by disrupting its structure. Peptides would insert into the membrane and aggregate into higher order structures that allow particles to move from the cell. This would disrupt the membrane potential, and eventually result in cell death.

The ability of tyrocidine peptides to disrupt membrane structure by forming higher order structures/channels was probed further. This was based on previous studies, which have indicated that tyrocidine peptides form helical structures in mixed solvents.[11] Based on this and also armed with a crystallographically solved structure of Gramicidin S (a similar decapeptide), channels of tyrocidine were produced using homology modelling.[12] The channel models as well as the Gramicidin S channel were subjected to molecular dynamics in a membrane. All the channels allowed water molecules to pass through and were more stable in the lipid section of the membrane compared to the water section of the membrane. The gramicidin S channel completely dissociated in the water section of the membrane pointing out that it is unlikely to exist as a channel in aqueous solution. The rate at which the channels allowed water molecules to move from one side of the membrane to the other was constant. However TyrC allowed more water molecules to pass through it followed by Gramicidin S, while TyrA allowed the least number of water molecules to pass through per unit time. In order to retain the channel structures intact, it may be necessary to tilt them away from the normal to the bilayer surface, keeping all of the monomers within the lipophilic part of the membrane. That would still allow water (and ions) to diffuse through the polar head groups to the opening.

The alternative non-lytic mechanism of action of tyrocidines, which involves the binding of Ca^{2+} to tyrocidine, was also studied using NMR spectroscopy and DFT methods. NMR titrations showed very small chemical shift changes of the amide protons upon addition of Ca^{2+} to the proton. This highlighted a possibility of a very weak binding between the peptide and Ca^{2+}. Attempt to probe this using isothermal titration calorimetry (results not shown) were unsuccessful as the heats of solvent mixing were greater than the heat of complexation. This observation was contrary to what was obtained from DFT studies, where the possible complexes that were modelled indicated a very high binding energy between the peptide and Ca^{2+}. There was therefore no correlation between the quantum mechanics results and the NMR results.

The overall conclusion of this study is that, there could be several mechanisms through which tyrocidines can disrupt a membrane. Events such as self-assembly, membrane binding and channel formation may all play roles in the mechanism of action of tyrocidine peptides.

8.2 Recommendations

Simulations of the interactions between the peptides and the membrane were relatively short because of the limited computer time available. Longer simulations are likely to avail more information about the mechanism of action of tyrocidine peptides.

There is very limited experimental evidence on the ability of tyrocidine peptides to form channels similar to that of gramicidin S. The proposed mechanism of these channels is very promising, however there is need for it to be investigated further experimentally to understand the structure and stability of tyrocidine aggregates in the membrane.

The alternative non-lytic mechanism could not be confirmed from the simulations that were performed. This was probably because of the concentrations of Ca^{2+} that were used in the experiments. Previous studies have shown that in low Ca^{2+} concentration solutions, the mechanism of action of tyrocidine is not different from the one it exhibits in Ca^{2+} free environments. The mechanism of action has been shown to change at very high Ca^{2+} concentration.[4] It has been proposed that Ca^{2+} influences the mechanism of aggregation or the orientation of peptides in the aggregates thereby causing tyrocidine to utilize a different non-lytic mechanism.[4] There is therefore a need for this study to be carried out at significantly higher concentrations than the ones used in the present study.

8.3 References

1. Bello J, Bello HR, Granados E. Conformation and aggregation of melittin: Dependence on pH and concentration. Biochemistry 1982;21:461-5.
2. Falla TJ, Karunaratne DN, Hancock REW. Mode of action of the antimicrobial peptide indolicidin. Journal of Biological Chemistry 1996;271:19298-303.
3. Marques MA, Citron DM, Wang CC. Development of tyrocidine A analogues with improved antibacterial activity. Bioorganic & Medicinal Chemistry 2007;15(21):6667-77.
4. Spathelf BM. Qualitative structure-activity relationships of the major tyrocidines, cyclic decapeptides from bacillus aneurinolyticus. Stellenbosch University; 2010.
5. Paradies HH. Aggregation of tyrocidine in aqueous solutions. Biochemical and Biophysical Research Communications 1979;88:810-7.
6. Laiken SL, Printz MP, Craig LC. Studies on the mode of self-assembly of tyrocidine B. Biochemical and Biophysical Research Communications 1971;43:595-600.
7. Ruttenberg MA, King TP, Craig LC. The use of the tyrocidines for the study of conformation and aggregation behavior. Journal of the American Chemical Society 1965;87:4196-8.
8. Hotchkiss RD. Gramicidin, tyrocidine and tyrothricin. In: Advances in enzymology and related areas of molecular biology. Editors; F. F. Nord, C. H. Werkman, 1944.
9. Rammelkamp CH, Weistein L. Toxic effects of tyrothricin, gramicidin and tyrocidine. The Journal of Infectious Diseases 1942;71(2):166-73.
10. Dubos RJ, Hotchkiss RD. The isolation of bactericidal substances from cultures of bacillus brevis. The Journal of Experimental Medicine 1941 May 01:155-62.

11. Ruttenberg MA, King TP, Craig LC. The chemistry of tyrocidine. VII. Studies on association behavior and implications regarding conformation. Biochemistry 1966;5:2857-63.
12. Llamas-Saiz AL, Grotenbreg GM, Overhand M, van Raaij MJ. Double-stranded helical twisted -sheet channels in crystals of gramicidin S grown in the presence of trifluoroacetic and hydrochloric acids. Acta Crystallographica Section D 2007;63:401-7.

Appendix

NOE derived distance restraints are shown in Table S4 to Table S6. The lower bound restraints were calculated by subtracting 10 % from the inter-proton distance and the upper bound restrains were calculated by adding 20 % to the inter-proton distances.

Table A1: TyrA NOE derived distance restraints with lower and upper bound restraints

Atoms	Distance (nm)	Lower bound (nm)	Upper bound (nm)
Phe^{1}_{NH} - Leu^{10}_{HD23}	0.230	0.207	0.276
Phe^{1}_{HA} - Pro^{2}_{HD1}	0.230	0.207	0.276
Phe^{1}_{HA} - Pro^{2}_{HD2}	0.205	0.185	0.246
Pro^{2}_{HA} - $Phe^{1}_{H}{}^{N}$	0.245	0.221	0.294
Pro^{2}_{HB1} - $Phe^{1}_{H}{}^{N}$	0.295	0.266	0.354
$Phe^{3}_{H}{}^{N}$ - $Leu^{10}_{H}{}^{N}$	0.295	0.266	0.354
Phe^{3}_{HA} - $Phe^{4}_{H}{}^{N}$	0.210	0.189	0.252
Phe^{3}_{HB1} - $Phe^{1}_{H}{}^{N}$	0.260	0.234	0.312
Phe^{3}_{HB2} - $Phe^{1}_{H}{}^{N}$	0.260	0.234	0.312
Phe^{3}_{HB1} - $Leu^{10}_{H}{}^{N}$	0.325	0.293	0.390
Phe^{3}_{HB2} - Phe^{4}_{CD1}	0.325	0.293	0.390
Phe^{4}_{HA} - $Asn^{5}_{H}{}^{N}$	0.200	0.180	0.240
Phe^{4}_{HA} - Orn^{9}_{HA}	0.220	0.198	0.264
Phe^{4}_{HB1} - $Asn^{5}_{H}{}^{N}$	0.250	0.225	0.300
Phe^{4}_{HB2} - $Asn^{5}_{H}{}^{N}$	0.255	0.230	0.306
$Asn^{5}_{H}{}^{N}$ - $Val^{8}_{H}{}^{N}$	0.275	0.248	0.330
Asn^{5}_{HA} - $Gln^{6}_{H}{}^{N}$	0.255	0.230	0.306
Asn^{5}_{HB1} - $Gln^{6}_{H}{}^{N}$	0.205	0.185	0.246
Asn^{5}_{HB2} - $Gln^{6}_{H}{}^{N}$	0.240	0.216	0.288
Asn^{5}_{HD21} - Val^{8}_{HB}	0.290	0.261	0.348
$Gln^{6}_{H}{}^{N}$ - $Tyr^{7}_{H}{}^{N}$	0.245	0.221	0.294
Gln^{6}_{HA} - $Tyr^{7}_{H}{}^{N}$	0.345	0.311	0.414
Gln^{6}_{HB1} - $Tyr^{7}_{H}{}^{N}$	0.310	0.279	0.372
Gln^{6}_{HB2} - $Tyr^{7}_{H}{}^{N}$	0.310	0.279	0.372
$Tyr^{7}_{H}{}^{N}$ - $Val^{8}_{H}{}^{N}$	0.205	0.185	0.246
Tyr^{7}_{HA} - $Phe^{1}_{H}{}^{N}$	0.205	0.185	0.246
Tyr^{7}_{HA} - $Val^{8}_{H}{}^{N}$	0.320	0.288	0.384
Tyr^{7}_{HB1} - $Val^{8}_{H}{}^{N}$	0.255	0.230	0.306
Tyr^{7}_{HB2} - $Val^{8}_{H}{}^{N}$	0.305	0.275	0.366
Val^{8}_{HA} - $Orn^{9}_{H}{}^{N}$	0.200	0.180	0.240
Val^{8}_{HB} - $Asn^{5}_{H}{}^{N}$	0.325	0.293	0.390
Val^{8}_{HB} - $Orn^{9}_{H}{}^{N}$	0.270	0.243	0.324
Orn^{9}_{HA} - $Asn^{5}_{H}{}^{N}$	0.265	0.239	0.318
Orn^{9}_{HB1} - $Leu^{10}_{H}{}^{N}$	0.275	0.248	0.330
Orn^{9}_{HB2} - $Leu^{10}_{H}{}^{N}$	0.275	0.248	0.330
Orn^{9}_{HG1} - $Leu^{10}_{H}{}^{N}$	0.162	0.146	0.194
Orn^{9}_{HG2} - $Leu^{10}_{H}{}^{N}$	0.162	0.146	0.194
Leu^{10}_{HD11} - $Phe^{1}_{H}{}^{N}$	0.335	0.302	0.402

Table A2: TyrB NOE derived distance restraints with lower and upper bound restraints

Atoms	Distance (nm)	Lower bound (nm)	Upper bound (nm)
$Phe^{1}_{HD1/HD2}$ - Pro^{2}_{HD2}	0.430	0.344	0.516
Pro^{2}_{HB1} - $Trp^{3}_{H}{}^{N}$	0.460	0.368	0.550
Pro^{2}_{HB1} - Trp^{3}_{HD2}	0.500	0.400	0.550
Pro^{2}_{HD1} - $Trp^{3}_{H}{}^{N}$	0.390	0.314	0.468
Trp^{3}_{HA} - $Phe^{4}_{H}{}^{N}$	0.300	0.240	0.360
Trp^{3}_{HB1} - $Phe^{4}_{H}{}^{N}$	0.400	0.320	0.480
Phe^{4}_{HA} - $Asn^{5}_{H}{}^{N}$	0.330	0.264	0.396
Phe^{4}_{HB1} - $Asn^{5}_{H}{}^{N}$	0.390	0.312	0.468
Phe^{4}_{HB2} - $Asn^{5}_{H}{}^{N}$	0.360	0.288	0.432
$Phe^{4}_{HD1/HD2}$- Pro^{2}_{HG1}	0.450	0.360	0.540
$Phe^{4}_{HD1/HD2}$- Trp^{3}_{HB1}	0.430	0.344	0.516
$Phe^{4}_{HD1/HD2}$ - Trp^{3}_{HB2}	0.520	0.418	0.550
$Phe^{4}_{HD1/HD2}$- $Leu^{10}_{HD11/HD21}$	0.360	0.288	0.432
$Asn^{5}_{H}{}^{N}$ - $Val^{8}_{H}{}^{N}$	0.450	0.360	0.540
Asn^{5}_{HA} - $Gln^{6}_{H}{}^{N}$	0.430	0.344	0.516
Asn^{5}_{HB1} - $Gln^{6}_{H}{}^{N}$	0.390	0.312	0.468
Asn^{5}_{HD21} - Asn^{5}_{HB1}	0.360	0.288	0.432
Asn^{5}_{HD21} - Asn^{5}_{HB2}	0.450	0.360	0.540
$Gln^{6}_{H}{}^{N}$ - $Tyr^{7}_{H}{}^{N}$	0.460	0.368	0.550
Gln^{6}_{HB1} - $Tyr^{7}_{H}{}^{N}$	0.470	0.376	0.550
Gln^{6}_{HG1} - $Tyr^{7}_{H}{}^{N}$	0.470	0.376	0.550
Gln^{6}_{HE21} - Gln^{6}_{HB1}	0.430	0.344	0.516
Gln^{6}_{HE21} - Gln^{6}_{HB2}	0.430	0.344	0.516
$Tyr^{7}_{H}{}^{N}$ - $Val^{8}_{H}{}^{N}$	0.340	0.272	0.408
Tyr^{7}_{HB1} - $Val^{8}_{H}{}^{N}$	0.390	0.312	0.468
Tyr^{7}_{HB2} - $Val^{8}_{H}{}^{N}$	0.470	0.376	0.550
Val^{8}_{HA} - $Orn^{9}_{H}{}^{N}$	0.340	0.272	0.408
Orn^{9}_{HA} - $Phe^{4}_{HD1/HD2}$	0.440	0.352	0.528
Orn^{9}_{HA} - $Asn^{5}_{H}{}^{N}$	0.480	0.384	0.576
Orn^{9}_{HA} - $Leu^{10}_{H}{}^{N}$	0.290	0.231	0.349
Leu^{10}_{HA} - $Phe^{1}_{H}{}^{N}$	0.330	0.264	0.400
Leu^{10}_{HD11} - $Orn^{9}_{H}{}^{N}$	0.500	0.400	0.550

Table A3: TyrC NOE derived distance restraints with lower and upper bound restraints

Atoms	Distance (nm)	Lower bound (nm)	Upper bound (nm)
Trp^{3}_{HD1} - Phe^{1}_{HB1}	0.31	0.279	0.372
Trp^{3}_{HD1} - Pro^{2}_{HA}	0.30	0.027	0.360
Trp^{3}_{HD1} - Pro^{2}_{HB1}	0.29	0.261	0.348
Trp^{3}_{HD1} - Pro^{2}_{HD1}	0.26	0.234	0.312
Trp^{3}_{HD1} - Val^{8}_{HG11}	0.34	0.306	0.408
Trp^{3}_{HD1} - Leu^{10}_{HD1}	0.37	0.333	0.444
Trp^{4}_{HA} - Trp^{3}_{HB1}	0.29	0.261	0.348
Trp^{4}_{HD1} - Pro^{2}_{HB1}	0.30	0.267	0.360
Trp^{4}_{HD1} - Trp^{3}_{HB1}	0.27	0.243	0.324
Trp^{4}_{HD1} - Tyr^{7}_{HB1}	0.25	0.225	0.300
Trp^{4}_{HD1} - Val^{8}_{HB}	0.36	0.340	0.432
Trp^{4}_{HD1} - Orn^{9}_{HA}	0.25	0.225	0.300
Trp^{4}_{HD1} - Leu^{10}_{CB}	0.27	0.243	0.324
Trp^{4}_{HD1} - Leu^{10}_{HB2}	0.27	0.243	0.324
Trp^{4}_{HD1} - Leu^{10}_{HD1}	0.31	0.279	0.372
$Asn^{5}_{H^N}$ - Trp^{4}_{HA}	0.24	0.216	0.288
$Asn^{5}_{H^N}$ - Trp^{4}_{HB1}	0.26	0.234	0.312
$Asn^{5}_{H^N}$ - $Val^{8}_{H^N}$	0.31	0.279	0.372
$Asn^{5}_{H^N}$ - Val^{8}_{HG11}	0.33	0.297	0.396
$Asn^{5}_{H^N}$ - Orn^{9}_{HA}	0.33	0.297	0.396
$Asn^{5}_{H^N}$ - Orn^{9}_{HG1}	0.35	0.315	0.420
$Gln^{6}_{H^N}$ - Asn^{5}_{HB1}	0.26	0.234	0.312
$Tyr^{7}_{H^N}$ - Gln^{6}_{HB1}	0.30	0.267	0.360
$Tyr^{7}_{H^N}$ - Gln^{6}_{HG1}	0.29	0.261	0.348
$Tyr^{7}_{H^N}$ - $Val^{8}_{H^N}$	0.22	0.198	0.264
Tyr^{7}_{HD1} - Gln^{6}_{HG1}	0.33	0.297	0.396
$Val^{8}_{H^N}$ - Tyr^{7}_{HA}	0.29	0.260	0.348
$Val^{8}_{H^N}$ - Tyr^{7}_{HB1}	0.26	0.234	0.312
$Orn^{9}_{H^N}$ - Val^{8}_{HA}	0.24	0.216	0.288
$Orn^{9}_{H^N}$ - Val^{8}_{HG11}	0.34	0.306	0.408
Leu^{10}_{NH} - $Trp^{3}_{H^N}$	0.32	0.288	0.384
Leu^{10}_{NH} - Trp^{3}_{HB1}	0.32	0.288	0.384
Leu^{10}_{NH} - Orn^{9}_{HA}	0.20	0.180	0.240
Leu^{10}_{NH} - Orn^{9}_{HG1}	0.33	0.297	0.396
Leu^{10}_{NH} - Orn^{9}_{HD1}	0.33	0.300	0.396
Leu^{10}_{NH} - Orn^{9}_{HD2}	0.33	0.300	0.396